NANOPARTICLE EFFECT ON STRUCTURAL EVOLUTION OF PROTEIN-SURFACTANT SOLUTIONS

By

SUMIT MEHAN

Enrolment No. PHYS01201104020

Bhabha Atomic Research Centre, Mumbai, India

A thesis submitted to the

Board of Studies in Physical Sciences

In partial fulfillment of requirements

for the Degree of

DOCTOR OF PHILOSOPHY

of

HOMI BHABHA NATIONAL INSTITUTE

May, 2016

Homi Bhabha National Institute

Recommendations of the Viva Voce Committee

As members of the Viva Voce Committee, we certify that we have read the dissertation prepared by Shri Sumit Mehan entitled "Nanoparticle Effect on Structural Evolution of Protein-Surfactant Solutions" and recommend that it may be accepted as fulfilling the thesis requirement for the award of Degree of Doctor of Philosophy.

Chairman - Prof. S.L. Chaplot	**Date:**
Guide - Prof. V.K. Aswal	**Date:**
Examiner - Prof. J.K. Basu	**Date:**
Member 1- Prof. P.A. Hassan	**Date:**
Member 2- Prof. B.V.R. Tata	**Date:**

Final approval and acceptance of this thesis is contingent upon the candidate's submission of the final copies of the thesis to HBNI.

I hereby certify that I have read this thesis prepared under my direction and recommend that it may be accepted as fulfilling the thesis requirement.

Date: 23/09/2016

Place: Mumbai **Dr. V.K. Aswal**

(Guide)

STATEMENT BY AUTHOR

This dissertation has been submitted in partial fulfillment of requirements for an advanced degree at Homi Bhabha National Institute (HBNI) and is deposited in the Library to be made available to borrowers under rules of the HBNI.

Brief quotations from this dissertation are allowable without special permission, provided that accurate acknowledgement of source is made. Requests for permission for extended quotation from or reproduction of this manuscript in whole or in part may be granted by the Competent Authority of HBNI when in his or her judgment the proposed use of the material is in the interests of scholarship. In all other instances, however, permission must be obtained from the author.

(Sumit Mehan)

DECLARATION

I, hereby declare that the investigation presented in the thesis has been carried out by me. The work is original and has not been submitted earlier as a whole or in part for a degree / diploma at this or any other Institution /University.

(Sumit Mehan)

DECLARATION

I, hereby declare that the queries raised by the examiners of the thesis have been incorporated as suggested.

Dr. V.K. Aswal
(Guide)

List of Publications

In Refereed Journal:

Related to Thesis

1. Tuning of Protein-Surfactant Interaction to Modify the Resultant Structure
   Sumit Mehan, V. K. Aswal and J. Kohlbrecher
   Phys. Rev. E **92,** 032713 (2015).

2. Cationic versus Anionic Surfactant in Tuning the Structure and Interaction of Nanoparticle, Protein, and Surfactant Complexes
   Sumit Mehan, V. K. Aswal and J. Kohlbrecher
   Langmuir **30**, 9941 (2014).

3. Small-Angle Neutron Scattering Study of Structure and Interaction of Nanoparticle, Protein and Surfactant Complexes
   Sumit Mehan, A. J. Chinchalikar, S. Kumar, V. K. Aswal and R. Schweins
   Langmuir **29,** 11290 (2013).

4. Structure and Interaction of Silica Nanoparticle, BSA Protein and Mixed Nonionic-Ionic Surfactant Complexes
   Sumit Mehan, V. K. Aswal and J. Kohlbrecher
   Phys. Rev. E (Submitted).

5. Study of Protein Unfolding and Refolding using Mixed Surfactants
   Sumit Mehan, V. K. Aswal and J. Kohlbrecher
   (Under Preparation).

In Other Areas

6. Modified Interactions among Globular Proteins below Isoelectric Point in the Presence of Mono-, Di-and Tri-valent Ions: A Small Angle Neutron Scattering Study
   K. Das, S. Kundu, **Sumit Mehan** and V. K. Aswal
   Chem. Phys. Lett. **645**, 127 (2016).

7. Studies on Interactions among Lysozyme Proteins in Solution: Effects of Concentration, pD, Temperature and Monovalent Ions
   S. Kundu, **Sumit Mehan**, V. K. Aswal and P. Callow
   Chem. Phys. Lett. **622**, 23 (2015).

8. Structure and Interaction among Protein and Nanoparticle Mixture in Solution: Effect of Temperature.
   S. Kundu, K. Das, **Sumit Mehan** and V. K. Aswal
   Chem. Phys. Lett. **641**, 68 (2015).

9. Modification of Interactions among Proteins with the Lowering of Solution pD Toward the Isoelectric Point in Presence of Different Valent Ions
K. Das, S. Kundu, **Sumit Mehan** and V. K. Aswal
Chem. Phys. Lett. **610**, 405 (2014).

In Conferences and Symposia:

Related to Thesis

1. Modifications in Structure and Interaction of Nanoparticle-Protein-Surfactant Complexes in electrolyte solution
Sumit Mehan, S. Kumar, V. K. Aswal, R. Schweins
AIP Conf. Proc. **1731**, 050123 (2016).

2. Observation of dynamic equilibrium cluster phase in nanoparticle-polymer system
S. Kumar, **Sumit Mehan**, V. K. Aswal and R. Schweins
AIP Conf. Proc. **1731**, 040013 (2016).

3. Structural Study of Surfactant-dependent Interaction with Protein
Sumit Mehan, V. K. Aswal and J. Kohlbrecher
AIP Conf. Proc. **1665,** 040009 (2015).

4. Probing Nanoparticle Effect in Protein-Surfactant Complexes
Sumit Mehan, V. K. Aswal and J. Kohlbrecher
AIP Conf. Proc. **1665,** 050026 (2015).

5. Structure and Interaction of BSA Protein with Mixed Micelles
Sumit Mehan and V. K. Aswal
Conference on Neutron Scattering, HBCSE, Mumbai (2015).

6. Structure And Interaction in Nanoparticle-Protein-Surfactant Complexes
Sumit Mehan and V. K. Aswal
International Conference on Nano-Bio-Med (ICTP), IIT Bombay (2015).

7. Observation of Two Different Fractal Structures in Nanoparticle, Protein and Surfactant Complexes
Sumit Mehan, S. Kumar and V. K. Aswal
AIP Conf. Proc. **1591,** 167 (2014).

8. Tuning of Structure and Interaction in Nanoparticle-Protein-Surfactant Complexes
Sumit Mehan, V. K. Aswal and J. Kohlbrecher
Conference on Neutron Scattering, IISER, Pune (2014).

9. Tuning of Protein-Surfactant Interaction and their Resultant Structure
Sumit Mehan and V. K. Aswal
Interdisciplinary Symposium on Material Chemistry, BARC, Mumbai (2014).

10. Structure and Interaction of Nanoparticle-Protein-Surfactant Complexes
Sumit Mehan, V. K. Aswal and J. Kohlbrecher
Interdisciplinary Symposium on Material Chemistry, BARC, Mumbai (2014).

11. Role of Electrostatic Interaction on Surfactant Induced Protein Unfolding
Sumit Mehan, S. Kumar and V.K. Aswal
AIP Conf. Proc. **1512,** 160 (2013).

12. Probing Structures of Multi-components Systems comprising Protein, Surfactant and Nanoparticle in Aqueous Solution
Sumit Mehan, S. Kumar, V. K. Aswal and R. Schweins
International Symposium on Neutron Scattering, BARC, Mumbai (2013).

13. Observation of Adsorption vs. Depletion Interaction in Nanoparticle-Protein System
Sumit Mehan, S. Kumar and V.K. Aswal
Interdisciplinary Symposium on Material Chemistry, BARC, Mumbai (2012).

(Sumit Mehan)

Dedicated

To

My Parents

ACKNOWLEDGEMENTS

I would first like to express my sincere gratitude to my guide Dr. V.K. Aswal, Solid State Physics Division, Bhabha Atomic Research Centre, for his guidance, constant support, motivation, constructive criticism and valuable advices. I thank Dr. S. Basu, Head, Solid State Physics Division, Bhabha Atomic Research Centre, for his support and encouragement. I am also grateful to Dr. S.L. Chaplot, Dr. P.A. Hassan and Dr. B.V.R. Tata whose useful suggestions as doctoral committee members have been very helpful.

I also wish to thank Dr. S. Mazumder, Dr. D. Sen, Dr. Sugam Kumar, Dr. D. Ray and Dr. A. J. Chinchalikar, Dr. S. Abbas and Dr. J. Bahadur for many fruitful discussions during the course of thesis. My thanks are also attributable to Dr. J. Kohlbrecher, Paul Scherrer Institut, Switzerland and Dr. R. Schweins, Institut Laue Langevin, France for their help in carrying out SANS experiments. Thanks are due to Mr. Indresh yadav for help in experiments and useful scientific discussions.

Special thanks to Mr. Ripandeep Singh, Mr. Mayank K. Gupta, Mr. Avik Das, Ms. Neetika Sharma, Ms. Priyanka Biswas, Mr. Baltej Singh, Mr. Purushotam Dubey and Dr. Vindhya Kumari who directly or indirectly have helped me in achieving my goals. I would like to thank Dr. R. Mital, Dr. P. U. Sastry, Shri A. K. Patra and other colleagues in SSPD, BARC for being supportive during the tenure of the thesis. I am also thankful to my hostel mates, Dr. Lokesh Gambhir, Mr. Ravi Dhawan and Mr. Ganesh Kumar Maurya, for their support.

Last but not the least, I would like to thank my parents and all the family members for being supportive in my endeavour and extending encouragement throughout the work.

CONTENTS

Homi Bhabha National Institute

SYNOPSIS OF Ph. D. THESIS

1. **Name of the Student:** SUMIT MEHAN
2. **Name of the Constituent Institution:** Bhabha Atomic Research Centre, Mumbai
3. **Enrolment No.:** PHYS01201104020
4. **Title of the Thesis:** Nanoparticle Effect on Structural Evolution of Protein-Surfactant Solutions
5. **Board of Studies:** Physical Sciences

SYNOPSIS

Soft matter comprises an important class of materials which are commonly used in a wide range of technological applications [1]. These materials are easily deformed by thermal fluctuations and external forces. The structures of interest in these materials are much larger than the microscopic scale (atoms and molecules), and yet much smaller than the macroscopic scale (bulk) of material. The properties and interactions of these so called mesoscopic structures determine the macroscopic behavior of the material [2]. Everyday examples include detergents and cosmetics, paints, food additives, lubricants and fuel additives, rubbers etc. In addition a number of biological materials (blood, muscle, milk, yogurt, jelly) are classifiable as soft matter. Biological materials as soft matter provide a different perspective for understanding their structure [3]. Proteins are essential biomolecules of organisms and participate in virtually every process within cells. Proteins do structural or mechanical functions as well as many proteins are

enzymes that catalyze biochemical reactions and are vital to metabolism. Most proteins fold into unique three-dimensional structures. The shape into which a protein folds is known as its native conformation. Protein-surfactant complexes are widely studied to understand the stability and structural changes in protein. The self-assembly property of surfactants that leads to the micelle formation makes the protein-surfactant interaction more complex and effective towards applications [4]. They are regularly used in biochemical laboratories for protein molecular weight determination, membrane protein solubilisation, etc. It is believed that electrostatic and hydrophobic interactions play an important role in the formation of protein-surfactant complexes. In this thesis, interplay of these interactions (electrostatic and hydrophobic) has been investigated using model protein with different ionic and nonionic surfactants. These protein-surfactant complexes are further examined in the presence of charged nanoparticles. Nanoparticles due to their small size and large surface-to-volume ratio possess unique and distinct properties which are useful for their numerous applications [5]. Many of these applications require the interaction of nanoparticles with macromolecules such as proteins and micelles [6]. The interaction and resultant structure of nanoparticles with protein-surfactant complexes are reported in this thesis. These systems are mainly characterized by small-angle neutron scattering (SANS), which is an ideal technique to study such multi-component systems [7].

The thesis consists of seven chapters. The chapter 1 gives an introduction to the structure and function of proteins, self-assembly of surfactants and characteristics of nanoparticles. The interest in protein-surfactant complexes, their usefulness in presence of nanoparticles and objective of thesis are also discussed. The different experimental techniques for probing structure and interaction of such systems are described in chapter 2. The details of SANS are also discussed. The results of thesis are given in chapters 3 to 6. The structure and interaction of protein-surfactant complexes under different solution conditions are presented in chapter 3.

The nanoparticles effect on protein-surfactant complexes with different surfactants are discussed in chapters 4-6. The results of anionic nanoparticles on anionic protein-anionic surfactant complexes (all the components are similarly charged) are discussed in chapter 4. The study on nanoparticle effect on protein-surfactant complexes using cationic surfactant and their comparison with anionic surfactant (chapter 4) are reported in chapter 5. The nanoparticle effect on protein-surfactant complexes using nonionic surfactant and tuning by nonionic-ionic mixed surfactants is studied in chapter 6. Chapter 7 gives the summary of the thesis.

Proteins are the polymers of amino acids with a specific three-dimensional shape and charge on them [8]. Surfactants are amphiphilic molecules and can self-assemble to different structures [9]. Nanoparticles are particles between 1 and 100 nm in size [10]. A general introduction to theses systems (proteins, surfactants, nanoparticles) is given in **chapter 1**. The structures of proteins, interactions in protein solutions and types of proteins are discussed in details. Proteins have four different levels of structure - primary, secondary, tertiary and quaternary. The protein molecules in the solution are stabilized due to the repulsive (electrostatic and/or steric) interaction overcomes the attractive (van der Waals and/or hydrophobic effects) interactions between them [11]. These different interactions between the protein molecules can be suitably tuned to obtain their different phases leading to crystallization, denaturation, gelation etc. There are two more general types of protein molecules: globular proteins and fibrous proteins. Globular proteins are generally compact, soluble and spherical in shape. Fibrous proteins are typically elongated and insoluble. In this thesis, globular protein bovine serum albumin (BSA) has been used as a model system. BSA has a molecular weight of 66.4 kDa and its isoelectric point is at pH=4.7. About the surfactant molecules, their classification, micelle formation and different structures of micelles are discussed. Surfactants are amphiphilic molecules which above a threshold concentration known as critical micelle concentration (cmc) self assemble to form micelles. These are classified as ionic and nonionic on the basis of charge

on their head groups. The surfactant aggregates formed are of various types, shapes, sizes such as spherical or ellipsoidal, cylindrical or thread-like, disk-like micelles, membrane and vesicle. The three different surfactants [anionic sodium dodecyl sulphate (SDS), cationic dodecyl trimethylammoniumbromide (DTAB) and nonionic polyoxyethylene 10 lauryl ether (C12E10)] have been used in this thesis. Protein and surfactant together show rich phase behavior because of their common amphiphilic nature. The surfactant molecules are known to interact via electrostatic binding at low concentrations and cooperative binding at high concentrations. Tuning of the interaction between protein and surfactant by different means lead to a wide range of applications of their complexes from cosmetics to pharmaceuticals to protein separation. Some of these issues of interest are discussed in chapter 1. The characteristics of nanoparticles, synthesis methods and some important applications requiring their conjugation with protein-surfactant are also discussed. Charge-stabilized silica nanoparticles have been used in the present thesis because of their easy preparation, high stability, low toxicity and ability to be functionalized with a range of macromolecules. A layout of thesis is discussed in the end of this chapter.

The experimental techniques for the characterization of soft matter are described in **chapter 2**. In particular, SANS as mostly used in this thesis work is discussed in details. SANS is a diffraction experiment, which involves scattering of a monochromatic beam of neutrons from the sample and measuring the scattered neutron intensity as a function of wave vector transfer Q ($=4\pi\sin\theta/\lambda$, where λ is the incident neutron wavelength and 2θ is the scattering angle). In SANS experiment, one measures the scattered intensity as given by $I(Q) \sim (\rho_p - \rho_s)^2 \times P(Q) \times S(Q)$, where $P(Q)$ is the intraparticle structure factor and $S(Q)$ is the interparticle structure factor [7]. $P(Q)$ is the square of particle form factor and decided by the shape and size of the particle. $S(Q)$ depends on the spatial arrangement of particles and is thereby sensitive to interparticle interactions. The magnitude of the scattered neutron intensity in the

SANS experiments depends on contrast factor [$(\rho_p - \rho_s)^2$], the square of the difference between the average scattering length densities of the particle and the medium. Due to the fact that the scattering length is negative (= -0.372×10^{-12} cm) for hydrogen and positive (= 0.667×10^{-12} cm) for deuterium, SANS is ideally suited for studying the structural aspects in hydrogenous materials. Deuterating either the particle or the medium can easily enhance the contrast between the particle and the medium. Further the multi-components systems can be simplified to study them by selectively contrast matching the components with the partial deuteration of the components. In addition to SANS, dynamic light scattering (DLS) is used wherever required to compliment the SANS results [12]. This technique is also described in chapter 2.

The structure and interaction of anionic BSA protein with anionic SDS, cationic DTAB and nonionic C12E10 surfactants have been studied in **chapter 3** [13-15]. The interaction of protein with these different surfactants is examined with varying concentration of surfactant, ionic strength and mixture of surfactants. The protein-surfactant interaction is maximum when the two components are oppositely charged, followed by components having similarly charged through the site-specific binding, and no interaction in the case of nonionic surfactant. This interaction of protein with ionic surfactants is characterized by the fractal structure representing bead-necklace structure of micelle-like clusters adsorbed along the unfolded protein chain [16, 17]. The interaction is enhanced with ionic strength only in the case of site-specific binding of anionic surfactant with anionic protein, whereas it is almost unchanged for other complexes of cationic and nonionic surfactants with anionic protein. Interestingly, the interaction of BSA protein with ionic surfactants is significantly suppressed in presence of nonionic surfactant. These results with mixed surfactants are thus used to fold back the unfolded protein as well as to prevent the surfactant-induced protein unfolding. For different solution

conditions, the results are interpreted in terms of change in the fractal dimension, overall size of the protein-surfactant complex and number of micelles attached to the protein. The interplay of electrostatic and hydrophobic interaction is found to govern the resultant structure of the complexes.

The effect of anionic silica nanoparticles with anionic BSA protein and anionic SDS surfactant has been examined in **chapter 4** [18-20]. Although all the components are similarly charged, strong structural evolutions amongst them have been observed. The complexes of different components in pairs (nanoparticle-protein, nanoparticle-surfactant and protein-surfactant) have been examined to correlate the role of each component in the three-component nanoparticle-protein-surfactant system. The nanoparticle-protein system shows depletion interaction induced aggregation of nanoparticles in the presence of protein [21]. Both the nanoparticle and the surfactant coexist individually in nanoparticle-surfactant system. The bead-necklace structure is formed in protein-surfactant system (chapter 3). The nanoparticle effect in protein-surfactant system is found to be governed by the synergetic effect of nanoparticle-protein and protein-surfactant interactions. The nanoparticle aggregates coexist with the structures of protein-surfactant complex in the three-component nanoparticle-protein-surfactant system. Both of these structures are characterized by mass fractals at different length scales. By applying selective contrast-matching of the components, it has also been observed that the nanoparticle aggregation as well as unfolding of protein is enhanced in this system as compared to the corresponding two-component systems.

Chapter 5 provides modifications in the structure and interaction of cationic DTAB vs. anionic SDS surfactant for nanoparticle effect in protein-surfactant systems [22, 23]. In both the cases (DTAB and SDS), the structure of nanoparticles in protein-surfactant systems is predominantly determined by the interactions of individual two components. The nanoparticle-surfactant and protein-surfactant interactions for DTAB, whereas

nanoparticle-protein and protein-surfactant for SDS, are found to be responsible for the resultant structure of nanoparticle-protein-surfactant complexes. Irrespective of the charge on the surfactant, both of them form the similar kind of bead-necklace structure with the protein (chapter 3). The adsorption of these protein-surfactant complexes for DTAB on oppositely charged nanoparticles gives rise to the protein-surfactant complex mediated aggregation of nanoparticles (similar to that as observed with DTAB surfactant) [24]. It is unlike to that of depletion induced aggregation of nanoparticles with non-adsorption of protein-surfactant complexes for SDS in similarly charged nanoparticle systems (similar to that of protein alone). The micelles are found to be rearranging on adsorption of protein-surfactant complex on the nanoparticles in leading to their (nanoparticle) aggregation. On the other hand, the unfolding of protein in free protein-surfactant complex is found to be significantly enhanced with respect to without the presence of nanoparticles.

The effect of nanoparticles on protein-surfactant systems with nonionic C12E10 and mixed nonionic-ionic (C12E10-SDS and C12E10-DTAB) surfactants are reported in **chapter 6** [25]. The interactions in three-component system with nonionic surfactant are interpreted in terms of competition of two-component nanoparticle-protein and nanoparticle-surfactant interactions. The non-adsorption of both anionic BSA protein and nonionic C12E10 surfactants show depletion force induced aggregation in two-component nanoparticle-protein and nanoparticle-surfactant systems [26]. The morphology of nanoparticle aggregates is surface fractal with more close packing for nonionic C12E10 and mass fractal for anionic BSA protein mediated nanoparticle aggregates. BSA protein and nonionic C12E10 surfactants remains independently in solution. In the ternary nanoparticle-protein-surfactant system, the strong depletion force of nonionic C12E10 micelles dominates over that of anionic BSA protein to aggregate nanoparticles with morphology similar to nanoparticle-surfactant system coexisting with free BSA protein and nonionic C12E10 surfactants in solution. In the case of C12E10-SDS mixed surfactants,

the mixed micelles behave very similar to nonionic C12E10 surfactant to produce depletion force induced nanoparticle aggregates and for the case of C12E10-DTAB mixed surfactants behave similar to cationic DTAB surfactant to produce adsorption-mediated nanoparticle aggregates in solution. For the case of C12E10-DTAB mixed surfactants the aggregates are mediated by adsorption of cationic DTAB micelles instead of DTAB/C12E10 mixed micelles in solution. In all these systems, BSA protein remains unaffected and resultant structures are driven by the interaction of surfactant micelles with nanoparticles.

Chapter 7 summarizes the findings of the thesis. The thesis presents the structure and interaction in protein-surfactant complexes with varying surfactant and effect of nanoparticles in these systems. SANS has been used as a main technique to characterize these systems. The main results of the thesis are:

i) The protein (anionic BSA) interacts very differently with ionic and nonionic surfactants. Ionic surfactants, irrespective of their charge (anionic or cationic) strongly bind to protein to form a bead-necklace structure whereas no binding is found for nonionic surfactant with protein. This difference in interaction behavior of ionic and nonionic surfactants is used to refold the unfolded protein as well as to prevent the unfolding of protein through the mixed ionic-nonionic surfactants in these systems. The results are explained in terms of interplay of electrostatic and hydrophobic interactions.

ii) Nanoparticle effect in BSA protein-SDS surfactant systems is decided by the two-component interactions of protein-surfactant and nanoparticle-protein systems. Protein-induced nanoparticle aggregates coexists with the protein-surfactant complexes in the resultant system. Both the nanoparticle aggregation and protein unfolding are found to be enhanced in the resultant (nanoparticle-protein-surfactant) system as compared to the two-component (nanoparticle-protein and protein-surfactant) systems.

iii) The effect of nanoparticles in protein-surfactant system with cationic DTAB surfactant is found to be quite different than that with anionic SDS surfactant. For DTAB, two-component protein-surfactant and nanoparticle-surfactant interactions decide the resultant structure of the system. The surfactant micelles-mediated fractal aggregates of nanoparticles coexist with free protein-surfactant system. The micelles are adsorbed through the protein-surfactant complex. Both the adsorbed and non-adsorbed protein-surfactant complexes on nanoparticles are modified.
iv) The differences observed in the interaction of protein with ionic and nonionic surfactants are also observed in the presence of nanoparticles. The interaction of protein with nonionic surfactant remains unaltered whereas nanoparticle aggregation is solely governed by the depletion interaction of surfactant micelles. Further, the mixed micelles of nonionic-ionic surfactants are used for tuning the interaction and structure of nanoparticle-protein-surfactant systems.

To conclude, protein-surfactant systems under varying solution conditions have been investigated. In particular, the structure and interaction of BSA protein with ionic (anionic SDS and cationic DTAB) and nonionic C12E10 surfactants are found to very different. The ionic surfactants strongly bind to the protein and form bead-necklace structure, whereas protein does not show any change with the nonionic surfactant. In each of these surfactants, silica nanoparticle effect on protein-surfactant systems has been examined. The surfactant-dependent different microstructures of nanoparticle aggregates (mass and surface fractals) are formed along with enhanced protein-surfactant interactions in the resultant nanoparticle-protein-surfactant systems. The interactions in these systems are governed by the competition of electrostatic (repulsive and/or attractive) and attractive depletion interaction. This work can be utilized in nanoparticle applications of drug delivery, phase separation processes and synthesis of functional materials.

REFERENCES

1. R. A. L. Jones, *Soft Condensed Matter* (Oxford University Press, New York, 2002).
2. C. N. Likos, Phys. Rep. **348**, 267 (2001).
3. I. W. Hamley, *Introduction to Soft Matter: Synthetic and Biological Self-Assembling Materials* (John Wiley & Sons, England, 2007).
4. D. Otzen, Biochim. Biophys. Acta. **1814**, 562 (2011).
5. A. E. Nel, *et al.* Nat. Mater. **8**, 543 (2009).
6. I. Lynch and K. A. Dawson, Nano Today **3**, 40 (2008).
7. D. I. Svergun and M. H. J. Koch, Rep. Prog. Phys. **66**, 1735 (2002).
8. D. Whitford, *Proteins: Structure and Function* (John Wiley & Sons, England, 2005).
9. M. J. Rosen and J. T. Kunjappu, *Surfactants and Interfacial Phenomena* (Wiley, New Jersey, 2012).
10. G. Cao and Y. Wang, *Nanostructures and Nanomaterials: Synthesis, Properties and Applications* (World Scientific, Singapore, 2011).
11. J. Israelachvili, *Intermolecular and Surface Forces* (Academic Press, London, 2011).
12. P. A. Hassan, S. Rana, and G. Verma, Langmuir **31**, 3 (2015).
13. *S.* Mehan, V. K. Aswal and J. Kohlbrecher, Phys. Rev. E **92**, 032713 (2015).
14. S. Mehan, S. Kumar, and V. K. Aswal, AIP Conf. Proc. **1512**, 160 (2013).
15. K. Das, S. Kundu, S. Mehan, and V. K. Aswal, Chem. Phys. Lett. **610**, 405 (2014).
16. S. Chodankar, V. K. Aswal, J. Kohlbrecher, R. Vavrin, and A. G. Wagh, Phys. Rev. E **77**, 031901 (2008).
17. S. H. Chen, J. Teixeira, Phys. Rev. Lett. **57**, 2583 (1986).
18. S. Mehan, A. J. Chinchalikar, S. Kumar, V. K. Aswal, and R. Schweins, Langmuir **29**, 11290 (2013).
19. S. Mehan, S. Kumar and V. K. Aswal, AIP Conf. Proc. **1591**, 167 (2014).
20. K. Das, S. Kundu, S. Mehan, and V. K. Aswal, Chem. Phys. Lett. **645**, 127 (2016).
21. H. N. W. Lekkerkerker and R. Tuinier, *Colloids and Depletion Interaction* (Springer, New York, 2011).
22. S. Mehan, V. K. Aswal and J. Kohlbrecher, Langmuir **30**, 9941 (2014).
23. S. Mehan, V. K. Aswal and J. Kohlbrecher, AIP Conf. Proc. **1665**, 050026 (2015).
24. S. Kumar, V. K. Aswal and J. Kohlbrecher, Langmuir **28**, 9288 (2012).
25. S. Mehan, V. K. Aswal and J. Kohlbrecher (Under Preparation).
26. D. Ray and V. K. Aswal, J. Phys.: Condens. Matter. **26**, 035102 (2014).

LIST OF FIGURES

Figure 3.10. (a) DLS data of 1 wt% BSA protein with 40 mM of mixed surfactants (DTAB and C12E10) with varying mole fraction (X) of nonionic surfactant at pH=7 and 0.2 M NaCl in D_2O. (b) The variation in hydrodynamic radii of 1 wt% BSA protein with 40 mM of mixed surfactants (DTAB and C12E10) with varying mole fraction (X) of nonionic surfactant at pH=7 and 0.2 M NaCl.

Figure 3.11. (a) SANS and (b) DLS data of 1 wt% BSA protein with 40 mM of mixed surfactants (SDS and C12E10) with varying mole fraction (X) of nonionic surfactant at pH=7 and 0.2 M NaCl in D_2O. The inset in Figure (b) shows the variation of effective hydrodynamic radius with the change in the mole fraction of nonionic surfactant.

Figure 3.12. SANS data of 1 wt% BSA protein with 40 mM of mixed surfactants (a) DTAB and C12E10 and (b) SDS and C12E10 at 1:1 mole fraction of ionic and nonionic surfactants at pH=7 and 0.2 M NaCl in D_2O. The data are compared with the change in the order of mixing of ionic and nonionic surfactants.

Figure 3.13. Schematic of the protein unfolding and refolding using ionic, nonionic and mixed surfactants.

Figure 4.1. Experimental verification of contrast-matched conditions (a) silica nanoparticles and (b) SDS micelles. A flat pattern is obtained of incoherent scattering as compared to that scattering from D_2O as solvent.

Figure 4.2. SANS data from 1 wt% HS40 silica nanoparticles, 1 wt% BSA protein and 50 mM SDS surfactant in presence of 0.2 M NaCl in D_2O. Data have been fitted by different structural models for differences in the scattering profiles of silica nanoparticles (polydisperse spheres), BSA protein (oblate ellipsoid) and SDS micelles (prolate ellipsoid).

Figure 4.3. SANS data from the three-component system of 1 wt% HS40 silica nanoparticles, 1 wt% BSA protein and 50 mM SDS surfactant mixed together in presence of 0.2 M NaCl in D_2O. Insets show the differences between the measured data of the three-component system with that of the addition of data of individual components (nanoparticle, protein and surfactant) as shown in different *Q* (low, intermediate and high) regions.

Figure 4.4. SANS data from 1 wt% HS40 silica nanoparticles with 1 wt% BSA protein is compared with individual components (1 wt% HS40 and 1 wt% BSA) in presence of 0.2 M NaCl (a) in D_2O and (b) in H_2O. Inset of (a) shows the comparison of experimentally measured data of 1 wt% HS40 + 1 wt% BSA to the calculated sum of individual component data. Scattering data of 1 wt% HS40 + 1wt% BSA are fitted by the model of coexistence of nanoparticle aggregates with BSA protein in the system.

Figure 4.5. SANS data from 1 wt% HS40 silica nanoparticles with varying concentration of BSA protein in presence of 0.2 M NaCl in D_2O. Data are fitted by the model of coexistence of nanoparticle aggregates with BSA protein in the system. The buildup of scattering in the higher *Q* region arises from the free (non-adsorbing) protein in the system.

Figure 4.6. SANS data from 1 wt% HS40 silica nanoparticles with 50 mM SDS micelles compared with individual components (1 wt% HS40 and 50 mM SDS) in presence of 0.2 M NaCl in D_2O. Inset shows the comparison of as measured data (1 wt% HS40 + 50 mM SDS) with that of the addition of individual components. Data of 1 wt% HS40 + 50 mM SDS are fitted by sum of model scattering from individual components of nanoparticles and micelles.

Figure 4.7. SANS data of 1 wt% HS40 with 50 mM SDS (a) nanoparticles are contrast-matched along with data from pure surfactant (SDS) system and (b) micelles are contrast-matched along with data from pure nanoparticle (HS40) system.

Figure 4.8. SANS data from (a) 1 wt% HS40 silica nanoparticles with varying concentration of SDS surfactant (b) different concentrations of individual SDS surfactants in presence of 0.2 M NaCl in D_2O. Data of mixed system are fitted by sum of model scattering from individual components of nanoparticles and micelles.

Figure 4.9. SANS data from 1 wt% BSA protein with varying concentration of SDS surfactant in presence of 0.2 M NaCl in D_2O. Data in lower surfactant concentration (0 – 10 mM) are fitted by the expanded protein structure whereas by fractal structure of micelle-like clusters randomly distributed along the unfolded protein chain for higher concentrations of surfactant (25 – 100 mM). The free micelles are also found to be coexisting with protein-surfactant fractal structure in the case of 100 mM SDS.

Figure 4.10. SANS data from three-component system of 1 wt% HS40 silica nanoparticles mixed with 1 wt% BSA protein and 50 mM SDS surfactant and compared along with two-component systems of 1 wt% HS40 + 1 wt% BSA and 1 wt% BSA + 50 mM SDS in presence of 0.2 M NaCl in D_2O. Data of three-component system are fitted by the sum of the scattering contributions of protein-surfactant complexes and nanoparticle aggregates as induced by proteins.

Figure 4.11. SANS data from 1 wt% HS40 silica nanoparticles mixed with 1 wt% BSA protein and varying concentration of SDS surfactant (5 – 100 mM) in presence of 0.2 M NaCl in D_2O.

Figure 4.12. Schematic of the structures formed in the three-component nanoparticle-protein-surfactant system.

Figure 4.13. SANS data (a) 1 wt% HS40 + 1 wt% BSA + 50 mM SDS having silica nanoparticles contrast matched are compared with 1 wt% BSA + 50 mM SDS and (b) 1 wt% HS40 + 1 wt% BSA + 50 mM SDS having surfactant contrast matched are compared with 1 wt% HS40 + 1 wt% BSA in presence of 0.2 M NaCl. Data of 1 wt% BSA + 50 mM SDS without and with nanoparticles (contrast matched) are fitted by bead-necklace structure of BSA-SDS complex whereas data of 1 wt% HS40 + 1 wt% BSA without and with surfactant (contrast matched) are fitted by coexistence of nanoparticle aggregates with BSA protein in the system.

Figure 5.1. SANS data of 50 mM DTAB surfactant compared with 50 mM SDS surfactants at pH=7 and in the presence of 0.2 M NaCl in D_2O.

Figure 5.2. SANS data of 1 wt% HS40 silica nanoparticles + 1 wt% BSA protein + 50 mM DTAB surfactant are compared with (a) sum of scattering from individual components (1 wt% HS40 silica nanoparticles, 1 wt% BSA protein and 50 mM DTAB surfactant) and (b) 1 wt% HS40 silica nanoparticles + 1 wt% BSA protein + 50 mM SDS surfactant at pH=7 and in the presence of 0.2 M NaCl in D_2O.

Figure 5.3. SANS data of 1 wt% HS40 silica nanoparticles + 50mM DTAB surfactant compared with the sum of scattering of individual components at pH=7 and in presence of 0.2 M NaCl in D_2O.

Figure 5.4. SANS data of 1 wt% HS40 silica nanoparticles + 50mM DTAB surfactant compared with (a) 1 wt% HS40 silica nanoparticles + 1 wt% BSA protein and (b) 1 wt% HS40 silica nanoparticles + 50 mM SDS surfactant at pH=7 and 0.2 M NaCl in D_2O.

Figure 5.5. SANS data of 1 wt% HS40 silica nanoparticles + 50 mM DTAB surfactant with (a) micelles are contrast matched and compared with 1 wt% HS40 silica nanoparticles and (b) nanoparticles are contrast matched and compared with 50 mM DTAB surfactant at pH=7 and 0.2 M NaCl.

Figure 5.6. SANS data of 1 wt% BSA protein + 50 mM DTAB surfactant compared with 1 wt% BSA protein + 50 mM SDS surfactant at pH=7 and in the presence of 0.2 M NaCl in D_2O.

Figure 5.7. SANS data of 1 wt% HS40 silica nanoparticles + 1 wt% BSA protein + 50 mM DTAB surfactant along with scattering data of 1 wt% HS40 silica nanoparticles + 50 mM DTAB surfactant and 1 wt% BSA protein + 50 mM DTAB surfactant at pH=7 and in the presence of 0.2 M NaCl in D_2O. Inset shows the scattering profile of 1 wt% HS40 silica nanoparticles + 1 wt% BSA protein + 50 mM SDS surfactant along with 1 wt% HS40 silica nanoparticles + 1 wt% BSA protein and 1 wt% BSA protein + 50 mM SDS surfactant at pH=7 and 0.2 M NaCl in D_2O.

Figure 5.8. Schematic of structures formed in three-component system of anionic silica nanoparticles, anionic BSA protein and cationic DTAB surfactant.

Figure 5.9. SANS data of 1 wt% HS40 silica nanoparticles + 1 wt% BSA protein + 50 mM DTAB surfactant compared with 1 wt% HS40 silica nanoparticles + 1 wt% BSA protein and 1 wt% HS40 silica nanoparticles + 50 mM DTAB surfactant at pH=7 and 0.2 M NaCl with micelles contrast matched.

Figure 5.10. SANS data of 1 wt% HS40 silica nanoparticles + 1 wt% BSA protein + 50 mM DTAB surfactant compared with (a) 1 wt% BSA protein + 50 mM DTAB surfactant (b) 1 wt% HS40 silica nanoparticles + 50 mM DTAB surfactant at pH=7 and in the presence of 0.2 M NaCl with nanoparticles contrast matched.

Figure 6.1. SANS data of 50 mM C12E10 surfactants compared with (a) 50 mM SDS and 50 mM C12E10/SDS mixed surfactants (b) 50 mM DTAB and 50 mM C12E10/DTAB mixed surfactants at pH=7 and 0.2 M NaCl in D_2O.

Figure 6.2. SANS data of 1wt% HS40 with 1 wt% BSA protein and 50 mM nonionic C12E10 surfactants compared to similar system with anionic SDS and cationic DTAB surfactants at pH=7 and 0.2 M NaCl in D_2O.

Figure 6.3. SANS data of 1wt% HS40 with 1 wt% BSA protein and (a) 50 mM of mixed C12E10/SDS surfactants compared to similar system with nonionic C12E10 and anionic SDS surfactants, (b) 50 mM of mixed C12E10/DTAB surfactants compared to similar system with nonionic C12E10 and cationic DTAB surfactants at pH=7 and 0.2 M NaCl in D_2O.

Figure 6.4. SANS data of 1 wt% HS40 nanoparticles with 50 mM of nonionic C12E10 surfactants compared to the sum of scattering of individual components (1 wt% HS40 nanoparticles and 50 mM nonionic C12E10 surfactants) at pH=7 and 0.2 M NaCl in D_2O.

Figure 6.5. SANS data of (a) 1 wt% HS40 nanoparticles with 50 mM of nonionic C12E10 surfactants compared with individual nanoparticles and 1 wt% HS40 nanoparticles with 1 wt% BSA protein under micelles contrast matched, (b) 1 wt% HS40 nanoparticles with 50 mM of nonionic C12E10 surfactants compared with individual nonionic C12E10 surfactants with nanoparticles contrast matched at pH=7 and 0.2 M NaCl.

Figure 6.6. SANS data of 1 wt% HS40 nanoparticles with 50 mM of mixed C12E10/SDS, C12E10/DTAB and nonionic C12E10 surfactants at pH=7 and 0.2 M NaCl in D_2O.

Figure 6.7. SANS data of 1 wt% HS40 nanoparticles with 50 mM of mixed C12E10/SDS, C12E10/DTAB and nonionic C12E10 surfactants under different contrast conditions, (a) surfactant

contrast matched and (b) nanoparticles contrast matched at pH=7 and 0.2 M NaCl. Inset in both the figures shows the comparison of nanoparticles-C12E10/DTAB surfactant system with nanoparticles-DTAB surfactant system under micelles and nanoparticles contrast matched condition.

Figure 6.8. SANS data of 1 wt% BSA protein with (a) 50 mM C12E10 surfactant compared with sum of scattering of individual components and (b) C12E10/SDS, C12E10/DTAB mixed surfactants and nonionic C12E10 surfactants at pH=7 and 0.2 M NaCl in D_2O.

Figure 6.9. SANS data of 1 wt% HS40 nanoparticles with 1 wt% BSA protein and 50 mM of C12E10 surfactant compared with two-component 1 wt% HS40 nanoparticle with 1 wt% BSA protein and 1 wt% HS40 with 50 mM of C12E10 surfactant systems at pH=7 and 0.2 M NaCl in D_2O.

Figure 6.10. SANS data of 1 wt% HS40 nanoparticles with 1 wt% BSA protein and 50 mM C12E10 surfactant system compared with scattering from nanoparticle-surfactant system under different contrast conditions (a) Micelles contrast matched and (b) nanoparticles contrast matched at pH=7 and 0.2 M NaCl.

Figure 6.11. SANS data of 1 wt% HS40 nanoparticles with 1 wt% BSA protein and 50 mM of mixed C12E10/SDS surfactants compared with scattering from nanoparticle-protein-C12E10 surfactant system under different contrast conditions (a) surfactant contrast matched (b) nanoparticles contrast matched. SANS data of 1 wt% HS40 nanoparticles with 1 wt% BSA protein and 50 mM of mixed C12E10/DTAB surfactants compared with scattering from nanoparticle-C12E10 surfactant system under different contrast conditions (c) surfactant contrast matched (d) nanoparticles contrast matched at pH=7 and 0.2 M NaCl.

Figure 6.12. Schematic of structures formed in three-component system of anionic silica nanoparticles, anionic BSA protein and nonionic C12E10 surfactant.

LIST OF TABLES

Table 4.3. The fitted fractal dimension of aggregation of silica nanoparticles (1 wt% HS40) with varying concentration of BSA protein in presence of 0.2 M NaCl in D_2O. The mixed system (nanoparticle-protein) consists of aggregates of nanoparticles coexisting with individual proteins. The building block size of the fractal aggregates is same in all the cases that of the size of nanoparticle (87.1 Å), whereas the extent of aggregates has been taken a value larger than $2\pi/Q_{min}$ (~ 1000 Å) because of absence of lower *Q* cut-off.

Table 4.4. The fitted structural parameters of (5 – 100 mM) SDS micelles coexisting with (1 wt%) HS40 nanoparticles in presence of 0.2 M NaCl in D_2O. Data are fitted for prolate core-shell ellipsoidal shape of SDS micelles residing independently in solution. The similar parameters are also obtained for pure SDS micellar solution without HS40 nanoparticles.

Table 4.5. The fitted parameters of SANS analysis of protein-surfactant complex for 1 wt% BSA with varying concentration of SDS surfactant in presence of 0.2 M NaCl in D_2O. (i) Oblate ellipsoidal shape of the protein macromolecule for lower concentrations of surfactant (0 – 10 mM). (ii) Fractal structure of micelle-like clusters randomly distributed along the unfolded protein chain for higher concentrations of surfactant (25 – 100 mM).

Table 4.6. Fitted parameters of fractal structure of protein-surfactant complex (1 wt% BSA + 50 mM SDS) without and with nanoparticles. The analysis for protein-surfactant system with nanoparticles (1 wt% HS40) is from when the nanoparticles are contrast matched. Both the systems have been studied in presence of 0.2 M NaCl.

Table 5.1. The structural parameters of 50 mM DTAB and 50 mM SDS surfactant solutions at pH=7 and in the presence of 0.2 M NaCl in D_2O.

Table 5.2. The fitting parameters of two-component systems at pH=7 and in the presence of 0.2 M NaCl in D_2O. (a) Nanoparticle-protein system characterized by depletion interaction induced fractal aggregates of nanoparticles (from chapter 4). (b) Nanoparticle-surfactant system characterized by surfactant micelle mediated fractal aggregates of nanoparticles. (c) Protein-surfactant system characterized by fractal structure of micelle-like clusters formed along the unfolded protein chain.

Table 5.3. The fitting parameters of three-component nanoparticle-protein-surfactant system at pH=7 and in the presence of 0.2 M NaCl. [(a) Surfactant is contrast matched and (b) Nanoparticle is contrast matched]

Chapter 1

Introduction to Nanoparticles, Proteins and Surfactants

1.1. Introduction

The term soft matter comprises a broad class of physical states that are easily deformed by thermal fluctuations and external stresses [1]. The properties of these systems are intermediate to those of solids and liquids [2-5]. For example, the shear deformation in soft matter systems is resisted by both elastic and viscous behavior, which collectively is called viscoelastic property of soft mater systems. In such systems under the influence of shear force, the elastic properties dominate up to a particular time scale and the system maintains its shape, whereas flow like a liquid under the influence of viscosity above the particular time scale. The characteristic time scale of transformation from solid to liquid depends on many factors including size, shape and different interactions governing them. Many of the soft matter systems include liquid crystals show ordering intermediate to crystalline solids and liquids.

There are plenty of examples of soft materials in our everyday life such as the food that we eat which includes milk, butter, yogurt, mayonnaise, chocolate, ice cream etc [6-7]. The personal-care products used in our daily life such as toothpastes, shampoos, skin creams, lotions and conditioners are soft matter. The mechanical properties of these soft matter systems are tailored for specific applications. For example, the flow behavior and appearance are controlled by the use of high-molecular weight polymers and the presence of surfactants. The complex mixture of proteins and surfactants are used for the stability of gels, foams and emulsions used in cosmetics and food products [8-9]. The liquid crystal displays as used in display screens in

televisions, gaming devices, clocks, watches, calculators, and telephones are based on liquid crystal, which is a soft matter. The different optical properties of different orientationally ordered phases of liquid crystals are utilized in LCD displays [10].

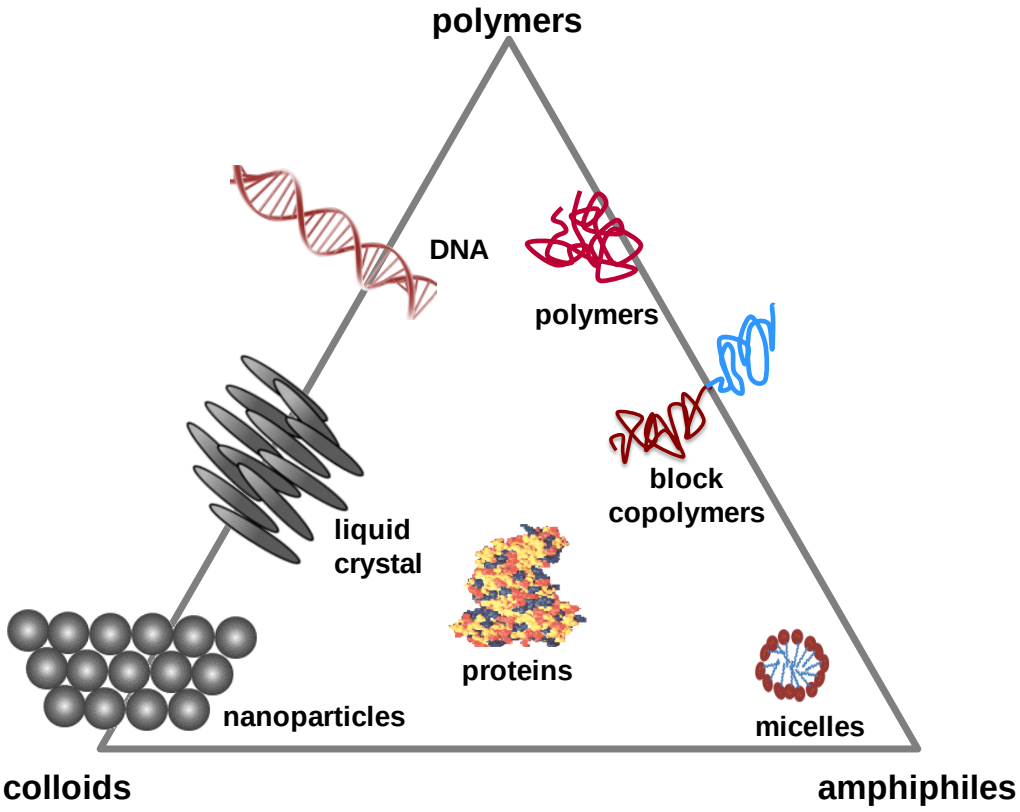

Figure 1.1. Different constituents of soft matter systems.

The common feature in all the soft matter systems discussed above is the constituents of these systems such as colloids, self-assemblies of amphiphiles and polymers have particle size in mesoscopic length scale (1-1000 nm), which is intermediate to atomic and macroscopic length scales (Figure 1.1) [11]. The soft matter systems have typically 10-12 orders of magnitude lower shear modulus as compared to hard matter systems. This large difference of shear modulus has a significant contribution from the length scales involved in soft matter systems [shear modulus$\propto (1/L)^3$]. Thus, this mesoscopic length scale of the constituent units contributes to the softness of soft matter materials. The particle size in mesoscopic length governs most of

the properties of soft matter systems. The chemical details and composition of soft matter systems have very limited influence on the properties of these systems. For example, the Brownian motion of colloidal particles, the self-assembly of surfactants and the flow behavior of polymers are all in large governed by their sizes and extension in three dimensional space. The Brownian motion of particles depends on their size, the self-assembly of surfactants is described by the area covered by truncated cone of suitable shape and the flow properties of polymers are described by its topology and extension in three dimensional space.

The properties of soft matter systems are governed by complex interactions among its constituent colloids in solution [12-14]. The stability of these systems is governed by interplay of attractive and repulsive interactions among the constituents (Figure 1.2). The Derjaguin-Landau-Verwey-Overbeek (DLVO) theory with van der Waals attractive term and screened Coulomb repulsive term is the simplest theory used to describe the stability of such systems [1,15-16]. The range and strength of these interactions depend on characteristics of constituents and solution conditions [1]. Other than these DLVO interactions, there are many non-DLVO interactions which play important role in deciding the phase behavior of soft matter [17-18]. The hydrophobic interactions, hydrogen bonding, steric repulsion, depletion interactions are some important non-DLVO interactions for soft matter systems. Hydrophobic interaction is entropy driven attraction among the hydrophobic patches in solution [17,19]. The presence of hydrophobic patches orders the water molecules around it and consequently decreases entropy of the solution. The aggregation of hydrophobic patches reduces the number of ordered water molecules and consequently increases the entropy of solution. The hydrogen bond is a weak dipole-dipole interaction between the hydrogen atom bounded to electronegative atom with lone pair of electrons [20-22]. The steric repulsion is the effective repulsions among the hydrocarbon

chains approaching each other [18,23]. This repulsion arises from the unfavourable entropy associated with the confinement of the polymer chains in solution. The depletion force is again entropy driven force, where the larger particles feel attraction in solution in the presence of non adsorbing smaller particles [24-26]. The applicability of these interactions is very diverse [27]. The hydrophobic effect is major contributor to the self-assembly of surfactants to form micelles and to stabilize the folded three dimensional structure of protein. The hydrogen bonding stabilizes the α-helix and β-sheet structure of proteins. The non-ionic micelles are formed by competition of hydrophobic interaction of micelle core and steric repulsion of hydrophilic head groups. In many cases, nanoparticles are stabilized by polymer adsorption through steric repulsions. The depletion force can destabilize the larger size particles in the presence of non-adsorbing smaller size particles.

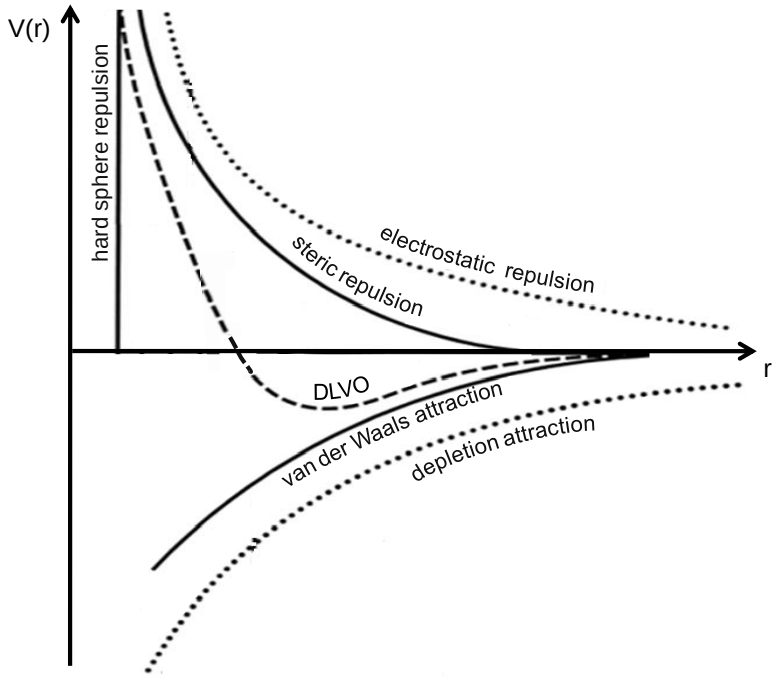

Figure 1.2. Typical interactions in soft matter systems.

Soft matter problems present significant challenges due to their many-body interactions at multiple length and time scales, the existence of metastable states and their often complex geometry and topology [28-30]. The applications of soft matter systems are diverse from our daily life products to biology to industrial applications. Biology has mastered the soft matter interactions. The function of a cell, to the working of blood and antibodies and enzymes are in large governed by soft complex interactions [2,31]. Even though the situation is different under living conditions where the biological molecules are out of equilibrium and simple laws of statistics cannot be applied. But the understanding of these interactions and possibility to tune them on demand is required to enhance our understanding of these systems for various potential applications [30,32].

Nanoparticles, proteins and surfactants are three major components of soft matter with numerous applications of each individual component. For example, proteins are essential biomolecules of organisms and participate in virtually every process within the cells. The unique three-dimensional structure of proteins is crucial for controlling their functionality in these systems. The self-assembly property of surfactants has applications in detergency and cosmetic industry [33]. Nanoparticles due to their small size and large surface-to-volume ratio possess unique and distinct properties which are useful for their applications in nanobiotechnology and drug delivery [34-35]. The conjugation of these components together enhances the system properties or generates new properties for different applications. For example, the self-assembly property of surfactants makes the protein-surfactant interaction more complex and effective towards applications [33,36]. These complexes are regularly used in biochemical laboratories for protein molecular weight determination, membrane protein solubilization, etc [37]. The nanoparticles interaction with macromolecules such as proteins, surfactants and their complexes

generates synergistic properties, which cannot be achieved through individual components [38-39]. These systems have the potential to improve the biocompatibility of nanoparticles for drug delivery applications, to enhance colloid stability, etc [40-42]. The interaction and resultant structure of nanoparticles with protein-surfactant complexes are investigated in the thesis. The important characteristics of individual components (proteins, surfactants and nanoparticles) are discussed in this chapter. The layout of the thesis is discussed at end of this chapter.

1.2. Structure of proteins

Proteins are the most abundant biological macromolecules of living organisms. They are unique amongst the biological macromolecules in underpinning almost every reaction in biological systems [4,43]. For example, antibodies and enzymes are proteins; skin and muscles are composed of proteins; some hormones are proteins; and some proteins are involved with digestion, respiration, reproduction are just to mention a few. The diverse functional proteins are simply the polymers of amino acids folded in a specific three dimensional shape with charged patches on their surface. It is the shape and charge of protein which is essential for controlling and regulating the stability and biological functionality of proteins. The shape and charge of protein depends on the different type of amino acids, the sequence and three dimensional arrangements of these amino acids in the protein. These molecules in aqueous solution are known to undergo different interactions (electrostatic, hydrophobic, hydrogen bonding, van der Waals, etc.) in aqueous solution [44-47]. The interplay of these interactions controls the structure of proteins as well as their stability.

1.2.1. Different structures of proteins

Proteins are the polymers of twenty different amino acids arranged in a linear chain and joined together by peptide bonds. Each amino acid consists of a central carbon atom C_α attached

to an amine ($–NH_2$), a carboxyl group (–COOH), an alkyl group (–R) and a hydrogen atom (–H). These twenty amino acids differ in the type of alkyl group (R) attached to the amino acids [43]. These different R groups result in different size, shape, charge, polarity, hydrophobicity and aromaticity of the amino acids. The polar amino acids have an oxygen atom or nitrogen atom in their side chain (R group) that can participate in hydrogen bonding within a protein or with the solvent molecules. These amino acids tend to form hydrogen bond with the solvent molecules and thus preferentially arrange themselves on the surface of protein. The hydrophobic amino acids are mostly comprised of carbon atoms and hydrogen atoms in their side chains. These amino acids avoid the surface exposure and tend to sequester themselves in the interior of protein. There are aromatic amino acids with aromatic hydrocarbon ring in their R group. These amino acids are joined together by peptide bonds to form polypeptide chain of protein. The folding of polypeptide chain of amino acids results in three dimensional structure of protein. The three dimensional structure of protein is described by the four level of organization as primary, secondary, tertiary and quaternary structure (Figure 1.3).

Primary structure: The primary structure is the linear chain arises from covalent linkage of individual amino acids via peptide bonds. The peptide bond is the covalent bond associating the carboxylic acid of the previous amino acid to the amino group of the next amino acid. Thus the primary structure gives us the information about the sequence of amino acids attached in the polypeptide chain of protein. This sequence is unique to the protein and is always given starting with N-terminal and ending with the C terminal amino acids. This N to C is the order in which amino acids are added during the synthesis of protein in the cell.

Secondary structure: The secondary structure refers to the formation of twists or kinks of primary structure of amino acids. The secondary structure is stabilized by the hydrogen bond

formation between the atoms of the amino acid backbones of the polypeptide chain. The two most common secondary structures are α-helix and β-plated sheet. The α-helix is the structural motif in proteins and over 30% of residues are found in helices for globular proteins. Atoms in α-helix arrange themselves in a helical pattern which has about 3.6 residues per turn and each residue offset from the proceeding residue by 0.15 nm. The hydrogen bond occurs in the peptide carboxyl oxygen of one residue and peptide amide nitrogen of a residue four places ahead in polypeptide chain. The hydrogen bonds from oxygen to nitrogen atoms are linear and parallel to the axis of α-helix. In α-helix structure the first four NH groups and last four CO groups normally lack backbone hydrogen bonds. This lack of hydrogen bonds results in distortion of α-helix structure for shorter polypeptide chain of amino acids.

The β-sheet is the second unit of secondary structure. It is an extremely elongated form of helical arrangement with two residues per turn and a translation distance of 0.34 nm between similar atoms in neighboring residues. These β-sheets are stabilized by backbone hydrogen bonds between adjacent residues from adjacent sheets that may be widely separated in the primary sequence.

Tertiary structure: The tertiary structure represents the folding of secondary structure elements in a compact unit arising from linking of different secondary structures. The tertiary structure can also be defined as the spatial three dimensional arrangements of amino acid residues in a protein. The different elements of secondary structure interact via hydrogen bonds, disulfide bridges, electrostatic interactions, van der Waals interactions, hydrophobic interactions etc. Many proteins consist of several domains, which are often connected only by a single segment of polypeptide chain. The proteins folded state is known to be marginal stable over the unfolded

state and the differences in stability are governed by non-covalent interactions governing the protein folding [45,48].

Quaternary structure: The proteins with more than one polypeptide chain exhibit the quaternary structure. The condition arises for proteins with number of amino acids larger than 150 residues. The different tertiary structures of polypeptide chains are called domains. The different domains of a protein interact among themselves with fewer interactions than the secondary structural elements within each domain. The nature of interactions (hydrogen bonds, disulfide bridges, electrostatic interactions, van der Waals interactions, hydrophobic interactions) among different domains of protein is same as those within a single domain.

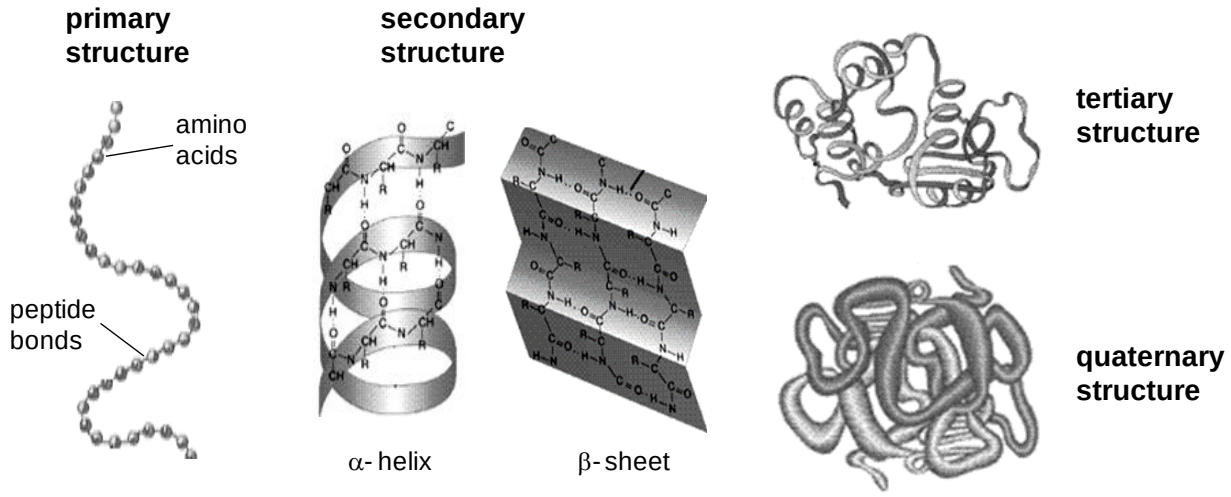

Figure 1.3. Different levels of protein structures.

1.2.2. Classification of proteins

Based on the three-dimensional structure and their physical properties, proteins have been divided into three classes as globular, fibrous and membrane proteins.

Globular protein: Globular proteins have a compact folded tertiary or quaternary structure of protein. The compact structure of protein is water soluble as the polar groups of atoms reside on

the protein's surface. The water solubility of globular proteins allows them to exist in biological fluids as individual molecules or in small clusters and to accomplish a wide range of functions [45,49]. Some of the examples of globular proteins are lysozyme, myoglobin, hemoglobin, bovine serum albumin (BSA), lactoglobulin and ovalbumin etc.

Fibrous protein: Fibrous proteins were named so because they are the constituents of most of the 'fibers' found in the body. These proteins generally form elongated structures and interactions are confined to local residues only. They are generally water insoluble and are found as an aggregate due to hydrophobic groups of amino acids that stick out of the molecule. These proteins have a common role in conferring strength and rigidity to these structures as well as physically holding them together. Three major groups of fibrous proteins are the collagens, keratins and silk fibroins.

Membrane protein: The membrane protein is a protein that is attached or associated with the membrane of a cell or an organelle. These proteins are difficult to isolate from the embedded lipid bilayers and are classified in two groups based on their strength of association with the lipid bilayers. Integral membrane proteins are the proteins remain firmly embedded within the hydrophobic bilayer and removal from this environment frequently results in a loss of structure and function. On the other hand, peripheral membrane proteins are temporarily attached either to the lipid bilayer or to integral proteins by a combination of hydrophobic, electrostatic and other non-covalent interactions. Peripheral proteins dissociate on treatment with a polar reagent.

A globular bovine serum albumin (BSA) protein has been used in this thesis. This protein functions biologically as a carrier for fatty acids, anions and other simple amphiphiles in the bloodstream [50]. It has a molecular weight of 66.4 kDa and consists of 583 amino acids in a single polypeptide chain. The protein contains 17 disulfide bridges. The isoelectric point is at

pH 4.7. The helical content is high 68%, and the content of β-sheet is 18%. The tertiary structure of BSA comprises three very similar domains. Figure 1.4 displays the structure of a BSA protein molecule.

Figure 1.4. Structure of a BSA protein molecule.

1.2.3. Stability of proteins

The three dimensional structure of protein has different levels as primary, secondary, tertiary and quaternary structures. Except the primary structure which is stabilized by covalent and peptide bonds, the higher levels of structures (secondary, tertiary and quaternary) are stabilized by relatively weak non-covalent interactions and disulphide bridges [45,48]. The disruption of structure at any level results in loss of biological functionality of protein from its native structure. The different processes that can destabilize the proteins are denaturing additives surfactants, urea, guanidium chlorides or the change in solution conditions pH, temperature and pressures etc [36,51-56]. In general, quaternary, tertiary and secondary structures are disruptsed in destabilizing the protein. The denaturation of protein in each of these processes has its own technological advantages and used in different scientific and industrial applications. The protein unfolding and refolding is an important issue that can be addressed using different mechanisms [54]. Some of the protein unfolding processes can be revert back to refold the unfolded protein [57-59]. But there are chances of proteins to be misfolded [45,60-61].

The important parameters which influence the protein stability and follow various routes in the protein denaturation are:

Effect of solution conditions: The increase in temperature results in weakening and breaking of non-covalent bonds such as hydrogen bonding, van der Waals interactions in the protein macromolecule [55-56,62]. The disruption of these bonds leads to exposure of hydrophobic groups hidden in the protein core to the solvent and aggregation of protein.

The increased pressure on the protein solution forces the transfer of solvent to the hydrophobic core of the protein molecule, there by breaking of weak bonds and unfolding of the protein [55-56].

The change in pH of protein solution protonate or deprotonate the amino acid side groups of the protein [63]. The hydrogen bonding and salt bridge interactions are altered and may result in denaturation of the protein.

Effect of denaturating additives: The presence of urea strengthens the hydrogen bonding between the water molecules and correspondingly increases the ordering of water molecules. The enhanced ordering of water molecules help to dissolve the protein hydrophobic groups in the solution. The improved solvation of the protein hydrophobic groups in the solution unfolds the protein [51-52,64].

The surfactants bind to proteins through the multistep binding under the influence of both electrostatic and hydrophobic interactions [36,65-66]. Surfactants interact with protein through site-specific electrostatic binding at low concentrations and cooperative binding via hydrophobic interactions at higher concentrations. The proteins are unfolded in cooperative binding region.

1.3. Self-assembly of surfactants

Surfactants are the surface active agents which tend to adsorb on surfaces and interfaces. They are amphiphilic molecules usually consist of a non-polar hydrophobic portion attached to a polar hydrophilic portion. The adsorption of surfactants on the surfaces and interfaces reduce the surface tension of solution [13,67-68]. The reduction in surface tension of solution by surfactant adsorption is the effect of low surface tension of hydrocarbons than water. The increase in surfactant concentration increases the surfactant adsorption at interface and reduces the surface tension of solution. As the surfactant concentration increases above a particular value called the critical micellar concentration (CMC), all the surface is fully occupied by the surfactant molecules. The surface tension of solution saturates to its minimum value at its critical micelle concentration. Beyond the CMC, the surfactant molecules self assemble to create supramolecular structures. The simplest possible surfactant self-assembly is the micelle, which is a cluster of surfactants in water (Figure 1.5). The micelle formation depends on the characteristics of surfactant and solution conditions.

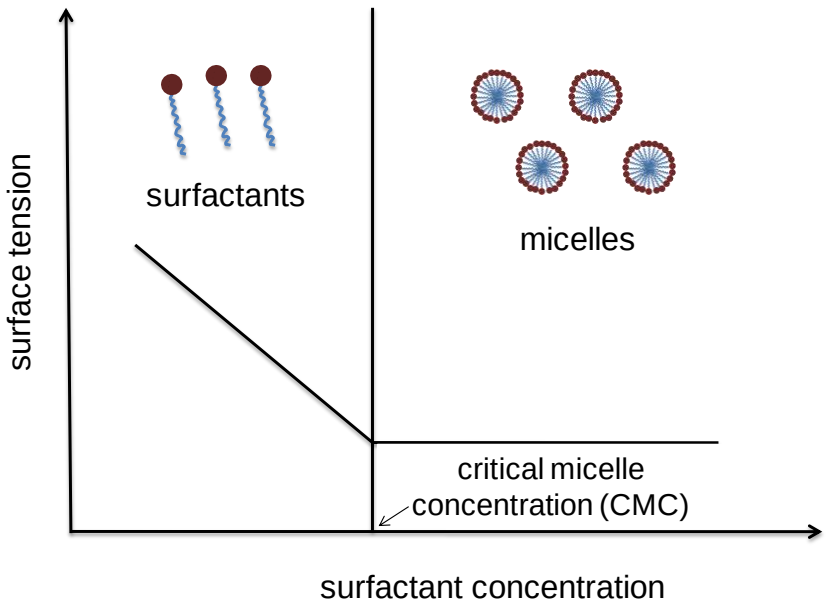

Figure 1.5. Schematic of micelle formation in the surfactant solution.

1.3.1. Classification of surfactants

The surfactants are commonly classified based on the nature of their hydrophilic head groups. They are classified as anionic, cationic, nonionic and zwitterionic surfactants. These different surfactants are distinguished by the charge on their head group. If the charge is negative, the surfactant is called anionic and if the charge is positive, it is called cationic. A nonionic surfactant does not have any charge on its head group. If a surfactant contains a head with two oppositely charged groups, it is termed zwitterionic. The surfactants can also be classified based on different tail lengths as well as in terms of number of tails. For example, the surfactants with twin tails are called gemini surfactants. The anionic sodium doecyl sulphate, cationic dodecyl trimethyl ammonium bromide and nonionic polyoxyethylene 10 lauryl ether surfactants are used in this thesis. The chemical structures of the surfactant are given in Figure 1.6. These surfactants have the same C12 carbon chain. The same chain length helps to study the role of head group interactions [electrostatic or steric] in deciding the properties of different systems.

(i) *Anionic surfactant*: sodium dodecyl sulphate ($C_{12}H_{25}SO_4^-Na^+$)

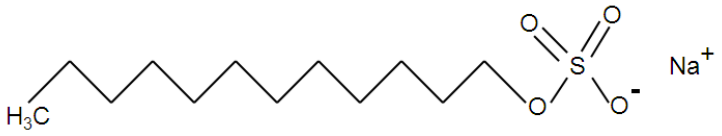

(ii) *Cationic surfactant*: dodecyltrimethyl ammonium bromide [$C_{12}H_{25}N(CH_3)_3^+ Br^-$]

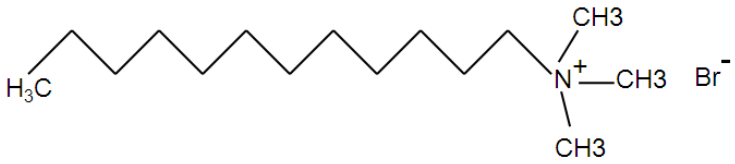

(iii) *Non-ionic surfactant*: decaoxyethylene *n*-dodecylether [$CH_3(CH_2)_{11}$ $(CH_2CH_2O)_{10}$ OH]

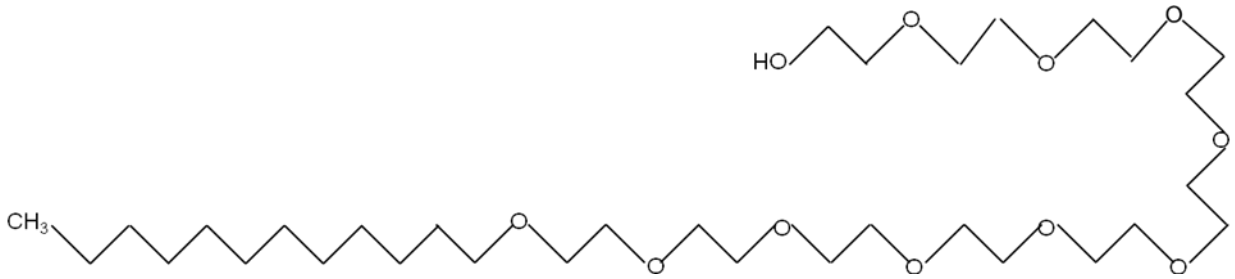

Figure 1.6. Chemical structures of anionic, cationic and nonionic surfactants.

1.3.2. Micelle formation

The surfactant molecules self assemble to form micellar aggregates in solution [13,67-69]. In this process of micelle formation, the hydrophobic tails sequester themselves inside aggregates and hydrophilic polar head groups orient themselves towards the aqueous phase in solution. The self-assembly of surfactant molecules to form micelles is a physiochemical process, where the surfactant molecules are associated via weak physical interactions and not strong chemical bonds. This self-assembly is governed by interplay of three major terms such as hydrophobic term, surface term and packing term. The hydrophobic term will sequester the hydrophobic chains inside interior of micelles. The surface term is usually governed by electrostatic or steric repulsions among charged or polar head groups of surfactants. The packing term restricts the geometrically accessible forms of surfactant aggregates so that head groups and water are excluded from core of surfactant aggregates. For the known shape and size of surfactant molecules the structure of self assembled surfactant aggregates can be predicted in terms of packing parameter $p=v/al$, where v is the volume of surfactant molecule, a is the area of the surfactant head group and l is the length of surfactant molecule. The various structures formed in solution depend on the packing parameter. The spherical micelles are

formed for the $p< \frac{1}{3}$, cylindrical or rod like for $\frac{1}{3} < p < \frac{1}{2}$ and vesicles or bilayer for $p \sim 1$ and inverted micelles for $p > 1$ (Figure 1.7).

The micelles formed by self-assembly of surfactants are in dynamic equilibrium with those in solution. The average residence time for a monomer in micelle may vary by orders of magnitude depending on the structure of surfactant molecules and typically ranges from 10^{-6} s for short chain surfactants and 10^{-3} s for long chain surfactants.

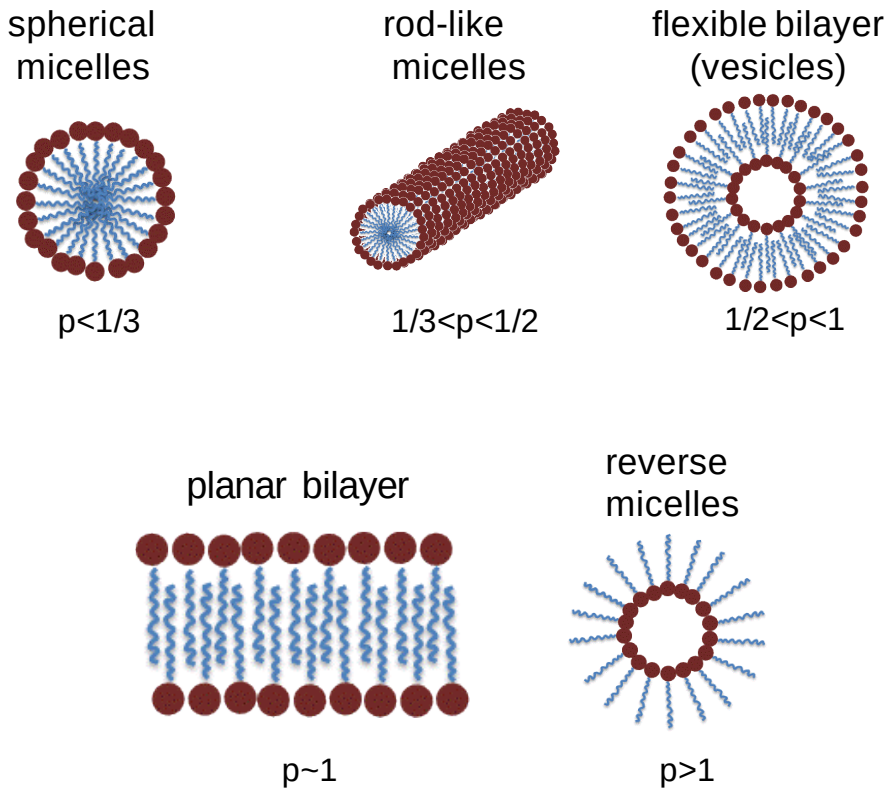

Figure 1.7. Different self-assembled structures in surfactant solutions.

1.3.3. Tuning of micellar structure

The self-assembly of surfactants is governed by hydrophobic term, surface term and packing term. The tuning of each of these terms can alter the morphology of self-assembled structures or micelles formed in solution [68,70-72]. For example, the hydrophobic interaction

can be simply varied by hydrocarbon tails with different chain lengths. The increase in chain length increases the hydrophobic interaction and consequently resulting in formation of larger structures with higher aggregation numbers. The surface term can be modified using different cationic, anionic or nonionic head group of surfactants, which tune the electrostatic or steric repulsion between the surfactant head groups in micelles. The packing term can be modified using bulky groups in hydrocarbon tail or bulky hydrophilic head groups [70]. Other than these parameters, the structure of self-assembled aggregates in solution can be modified by tuning the solution parameters such as concentration, ionic strength, pH, temperature etc [73-75]. At higher surfactant concentrations, the micellar aggregates in particular those of ionic surfactants transform to large non-spherical (e.g. ellipsoidal, rodlike and dislike) micelles. The change in pH and ionic strength influences the electrostatic repulsions among the surfactant head group for ionic surfactants. As a result the effective head group area and consequently packing parameter is affected. The ionic and nonionic surfactants are affected by temperature in different manners. The use of mixed micelles where more than two different kinds of surfactant molecules are used is one of the interesting systems to tune the micellar structure [76]. In many cases, even a small addition of second component (cationic-anionic mixed surfactants) can change the micellization process dramatically [77]. In some other cases, the structure of micellar aggregates can be tuned between the structures of individual components (e.g. mixed ionic-nonionic surfactants and surfactants with different tail lengths) [78-79].

The addition of components such as polymers, proteins and nanoparticles can also influence the micellization process of surfactants. For example, the addition of proteins in surfactant solution results in unfolding of protein along with formation of clusters of surfactants along the unfolded protein chain [80]. These clusters of protein-surfactant complexes have

different properties than the pure micelles in solution [66]. The surfactant addition in nanoparticles results in their adsorption on nanoparticle surface. These surfactants can form different structures as spherical or elongated micelles or bilayer on nanoparticle surface [81-82].

1.4. Interest in protein-surfactant complexes

Proteins and surfactants share the common property of being amphiphilic in nature resulting in strong interactions and hence diverse phase behavior of their complexes [36]. These complexes are used in many applications from cosmetics to pharmaceutical to protein separation process etc [37,58,83-84]. The interaction of surfactants with protein depends on many factors including the type of surfactant used (cationic, anionic or nonionic), type of protein, solution conditions (pH, ionic strength, temperature) etc. These different interactions result in different regimes of protein-surfactant interaction and different models have been proposed for the structure of protein-surfactant complexes.

1.4.1. Different regimes of protein-surfactant interaction

The surfactant binding to globular proteins is known to be accompanied by four characteristic regions as (i) specific binding, (ii) non-cooperative binding, (iii) cooperative binding and (iv) saturation region [80,85]. The binding isotherm of a typical protein-surfactant system is shown in Figure 1.8. At very low concentration of surfactants, the surfactants bind to proteins predominantly through specific binding, which is electrostatic in nature. In the specific binding surfactant head groups bind to the oppositely charged patches on protein. The specific binding region as governed by electrostatic interaction show significant dependence on type of surfactant and solution condition. For example the cationic and anionic surfactants show specific binding up to significantly high concentration range, whereas non ionic

surfactants lack any specific binding with protein [86]. The solution pH decides the effective charge as well as different charged patches of protein and influence the specific binding of surfactants with protein [87-89]. As the surfactant concentration is further increased, the non-cooperative binding or plateau region is followed (Figure 1.8). In the plateau region most of the ionic binding sites on protein are already occupied and additional surfactants remain independently in solution. The further addition of surfactants results in the cooperative binding region. In the cooperative binding regime, the binding affinity increases as more surfactant bound to protein. The cooperative binding region is governed by hydrophobic interactions, where the surfactants form micelle-like clusters along the unfolded protein chain (similar to micellization in water) [66,80,90]. The protein is believed to be unfolded in the cooperative binding region. The cooperative binding region follows steeper rise than specific binding region and a large concentration of surfactant bind to protein in this region. The cooperative binding region is followed by saturation region. In this region, surfactant binding to protein is saturated and additional surfactants form micelles which coexist with protein-surfactant complexes. The saturation binding concentration is believed to be controlled by the hydrophobic interactions or cooperative binding of surfactant with protein. Thus is believed to be independent of the charge head group of surfactants [90-91]. In terms of protein, different variety of proteins as globular, membrane and fibrous proteins show identical amount of anionic Sodium dodecyl sulphate surfactant (SDS) binding to the proteins (1.4 g of SDS per gram of protein) [92-94]. This fact is also responsible for the use of SDS in SDS-PAGE to find the molecular weight of unknown proteins and their separation [94].

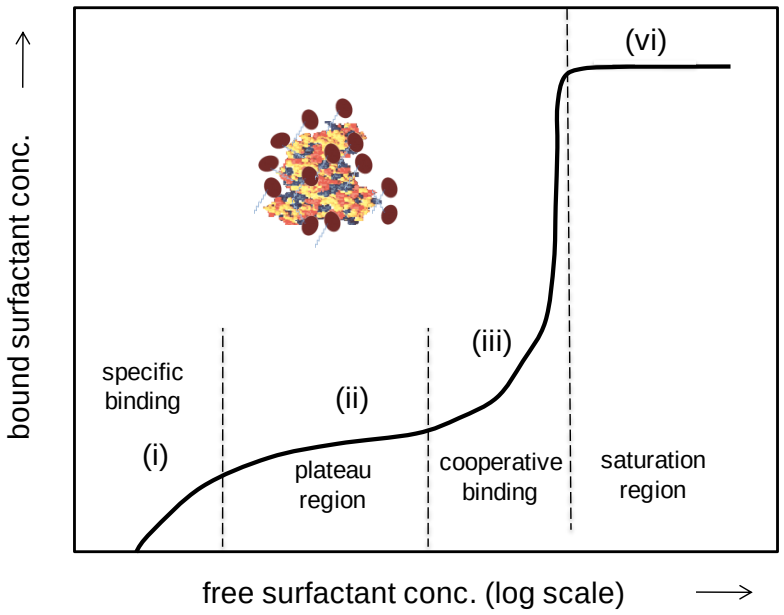

Figure 1.8. Typical binding isotherm of protein-surfactant systems.

1.4.2. Models of protein-surfactant complexes

The structure of protein-surfactant complexes have been characterized by different techniques including viscometric measurements, theoretical models, free-boundary electrophoresis, SANS, fluorescence, electron spin resonance (ESR) and nuclear magnetic resonance (NMR) etc. In general, the structure of protein-surfactant could be quite complex as well as diverse depending on the protein and surfactant used [36]. The BSA protein-SDS surfactant complex has been widely studied as model system. The structures of BSA-SDS complex is described by the following three models [80,95].

(i) Rod-like particle model: The rod-like particle model describe the complex as a rod like shape with cross sectional radius of about 18 Å (corresponding to surfactant tail length) and length proportional to the molecular weight of protein. The model was proposed on the basis of viscosimetric measurements.

(ii) Flexible helix model: The flexible helix model assumes a flexible cylindrical micelle formed by the SDS molecules with the hydrophilic segments of protein bound on its surface. The model was proposed based on the theoretical studies.

(iii) Bead-necklace model: In the bead-necklace model, the micelle-like clusters of surfactants adsorb along the unfolded polypeptide chain of protein as shown in Figure 1.9. The model was proposed based on the results of free-boundary electrophoresis technique [96]. SANS (small angle neutron scattering) studies have further concluded that the structure of protein-surfactant complexes can be described as bead-necklace model as compared to rod like or flexible helix model [97-98]. The viscometry, nuclear magnetic resonance and electron spin resonance studies have also supported this model [80].

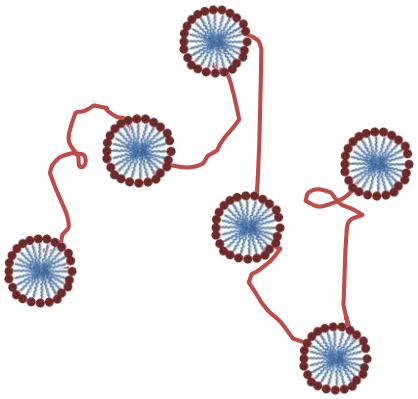

Figure 1.9. Representation of bead-necklace structure of protein-surfactant complexes.

1.4.3. Applications of protein-surfactant complexes

Tuning of the interaction between protein and surfactant by different means leads to a wide range of applications of their complexes from cosmetics to pharmaceuticals to protein separation process [37,40,58,83-84,99-100]. For example, in the protein separation process of SDS-PAGE (sodium dodecyl sulfate-polyacrylamide gel electrophoresis), the interaction of

surfactant with protein is used to unfold the protein through the formation of protein-surfactant complexes. Unfolded proteins are separated based on their mobility in polyacrylamide gel electrophoresis, which is directly dependent on the molecular weight of the protein [37,101]. The protein-surfactant complexes are also utilized in membrane protein solubilisation in the protein purification process [84,93]. In the cosmetics and pharmaceutical industry, the surfactants are also known to modify the properties of their products in terms of rheology, appearance and taste [83,102-103]. The tuning of concentration ratio of protein to surfactant as well as charge of surfactants can effectively tune these properties as per the requirement. In the detergent industry, proteins like enzymes are regularly used with mixture of surfactants in detergents [104]. Other than these, the coating of surfactant-induced unfolded protein can enhance the biocompatibility of nanoparticles for drug delivery applications [105]. The protein unfolded by ionic surfactants can be refolded back using different additives such as cyclodextrin [57-58]. This unfolding and refolding process can also be utilized to understand the mechanism of protein folding [100].

1.5. Characteristics of nanoparticles

Nanoparticles are the most widespread current form of nanomaterials with all the three dimensions in nanometer length scales (1-100 nm). These particles, due to their small size and large surface to volume ratio possess distinct fascinating properties (surface plasmon resonance, high electron mobility, superparamagnetism, giant magnetoresistance etc.) compared to their bulk counterparts [106-108]. These specific features of nanoparticles are utilized in variety of applications from medicine to electronics to catalysis to functional materials and many more [109-111]. Many of these applications require the conjugation of different macromolecules with nanoparticles to enhance the system properties or generate new properties for specific

applications [34,82,112]. Different macromolecules such as polymers, proteins, surfactants and block copolymers are utilized for different requirements of specific applications. The research interests on nanoparticles include from synthesis to understanding their unique properties to various applications.

1.5.1. Synthesis of nanoparticles

Nanoparticles have been synthesized and used for centuries. But recently reliable methods have been developed to manufacture nanoparticles with different sizes, shapes and polydispersity. Since the properties of nanoparticles show significant dependence on their size and shape, thus controlled synthesis is an important issue of consideration. The bottom up and top down are two broadly used approaches in synthesis of nanoparticles [108,113].

Top-down approach: Top-down approach relies on removal of bulk material to make nanomaterials. This approach uses division of bulk material or miniaturization of bulk fabrication process to produce the desired shape and properties. The milling, lithography and machining are commonly used top down methods. In general top-down approaches are less expensive, but have less control over the size distribution. These approaches could be destructive and can cause significant crystallographic damage to the resultant structures. Surface imperfections are more pronounced in top-down approaches.

Bottom up approaches: Bottom-up approach is a controlled additive process, where atoms, molecules and even nanoparticles are used as the building blocks for construction of complex materials. The controlled size, type and organization of the building blocks are utilized to generate the functional nanostructured materials. This is a highly controlled process. The nanomaterials obtained by this method have less defects and more homogenous chemical compositions. The vapour phase deposition, sol gel method and chemical reduction method are

commonly used bottom up approach. This approach is suitable for controlling monodispersity of the nanoparticles. Thus with lots of advantages the bottom-up approach is the most common route for nanomaterial production including nanoparticles.

Silica nanoparticles are used as model nanoparticles in this thesis. These nanoparticles are one of the most studied nanoparticles, because of their easy preparation, high stability, low toxicity and ability to be functionalized with a range of macromolecules [114-115]. These are usually electrostatically stabilized suspensions of amorphous, nonporous particles in a liquid phase. The usual particle size range is in between 10 to 100 nm in diameter as the smaller and larger particles are more unstable. Silica nanoparticles are synthesized usually in two ways: vapour phase deposition and sol-gel process. In vapour phase deposition, chemical vapour deposition (CVD) method is used for silica nanoparticle synthesis. Silica nanoparticles are produced through high temperature flame decomposition of precursors such as silicon tetra chloride ($SiCl_4$) with hydrogen and oxygen in CVD method. This method has difficulty in controlling the particle size, morphology, and phase composition, but is efficiently used for commercial synthesis of silica nanoparticles in powder form. The sol-gel method is a multi-step process where hydrolysis and condensation of metal alkoxides [$Si(OR)_4$] such as tetraethylorthosilicate [TEOS, $Si(OC2H5)_4$] or inorganic salts such as sodium silicate [Na_2SiO_3] is carried out in the presence of mineral acid (e.g. HCl) or base (e.g. NH_3) as catalyst [116]. The hydrolysis of silicon compound (TEOS) molecules forms silanol (Si–O–H) groups. The condensation/polymerization between the silanol groups creates siloxane bridges (Si–O–Si) that form entire silica structure in colloidal form. A general flow chart summarizing the silica nanoparticle synthesis by sol-gel process is shown in Figure 1.10 (a). In aqueous solution, the hydrogen ions from the surface of colloidal silica tend to dissociate, yielding an overall high

negative charge [Figure 1.10 (b)]. The colloidal suspension is first stabilized by adjusting the pH of the solution and then concentrated, usually by evaporation. The maximum concentration obtainable depends on the particle size, such as 50 nm particles can be concentrated to greater than 50 wt% solids, while 10 nm particles can only be concentrated to approximately 30 wt% solids, before the suspension becomes unstable. The Ludox HS40 silica nanoparticles used in this thesis are electrostatically stabilized 40 wt% concentrated amorphous, non porous solid suspensions of silica nanoparticles synthesized by sol-gel process.

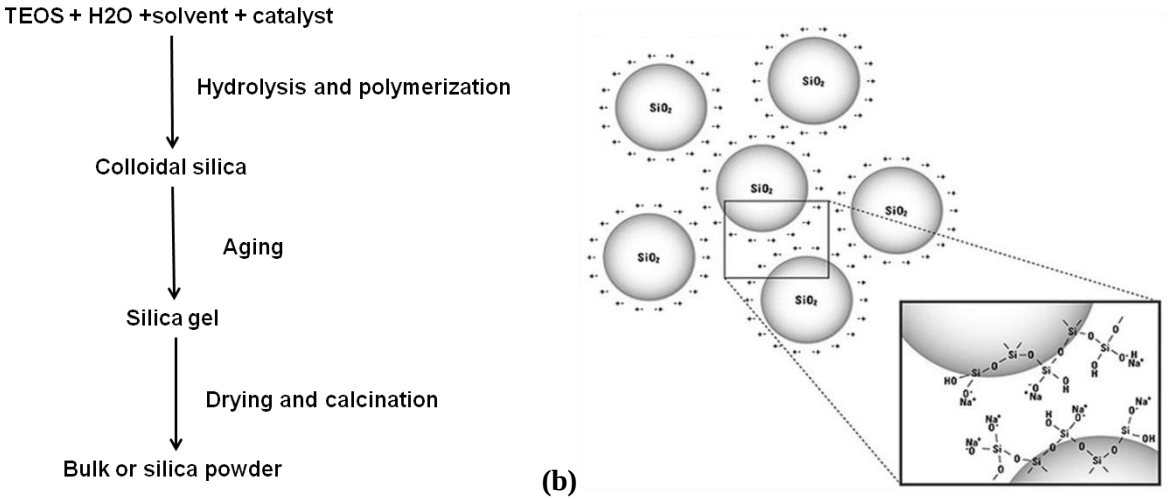

Figure 1.10. (a) Layout of sol-gel process for synthesis of colloidal silica nanoparticles and (b) schematic of charge stabilized silica nanoparticles.

1.5.2. Properties of nanoparticles

Nanoparticles have unique physical, chemical, optical, electrical, and magnetic properties as compared to their bulk counterparts [38,106,109,117-118]. Most of these properties can be controlled by tuning of the size and shape of nanoparticles. These distinct properties of particles at nanometer length scales can be described in terms of two kinds of effects called quantum size effect and surface atom effect.

The quantum size effect arises from the two processes, (i) confinement of electronic wave function to the smaller size particles (quantum confinement) and (ii) surface plasmon resonance (SPR) of conduction electrons [108-109,119]. The confinement of electronic wave function discretizes the electronic energy levels similar to the case of particle in a box. SPR is based on the collective oscillation of conduction electrons of the metal nanoparticle surface under the influence of electromagnetic field with characteristic frequency of incident light. The frequency of these oscillations depends on the size and shape of nanoparticles, free electron density as well as surrounding dielectric medium. The optical, electronic and magnetic properties of nanoparticles are affected by the quantum size effect.

The origin of surface atom effect is the lower coordination or unsaturated bonds of the surface atoms as compared to bulk atoms [108-109,119]. The unsaturated bonds of surface atom result in dangling bonds therefore surface atoms are more active than bulk. The number of surface atoms or specific surface area in a sample increases with decreasing size of its particles. For example, as the diameter of a spherical particle reduces from 1 mm to 1 nm, the available specific surface area (m^2/g) increases from 0.003 to 300, respectively. The surface-to-volume ratio scales with the inverse of particle size, and therefore the properties affected by surface atom effect follow the same scaling law. The catalytic properties, mechanical properties and thermodynamic properties of materials are modified by surface atom effects at nanometer length scales.

The quantum size effects are significant at very small size of nanoparticle usually less than 10 nm. The overall properties of nanoparticles are governed by both surface atom and quantum size effects, where the quantum effect is superimposed over the continuous function of

scalable surface atom effect [119]. The different nanoparticle properties affected by these effects are discussed in this section.

Optical properties: The optical properties of nanoparticles are governed by discretization of energy spectrum for semiconductor nanoparticles and surface plasmon resonance for noble metal nanoparticles. The smaller-sized nanoparticles have the bigger band gap and consequently optical adsorption of light can be tuned simply by change in nanoparticle size [119]. The semiconductor particles show blue shift in the light absorption with reduction in size as the band gap is increased. The noble metal nanoparticles have SPR in the visible and near-infrared region of the electromagnetic spectrum. The brilliant colors of gold nanoparticles, the possibility of tuning these colors with varying size, shape or via adsorption of macromolecules on nanoparticle surface are examples of surface plasmon effect [109].

Electronic properties: The electronic properties of nanoparticles are affected by quantum size effects as the band gap increases with reduction in nanoparticle size [108,119]. In the case of noble metal nanoparticles (gold, platinum, silver etc.), the conductive properties of nanoparticles transits from metallic to semiconductor to insulator properties with the decreasing nanoparticle size. Thus the nanoparticle electronic properties can be tuned conveniently via controlling the size of nanoparticles.

Magnetic properties: Superparamagnetism behavior is shown by ferromagnetic nanoparticles with decreasing particle size [107,111,120]. The ferromagnetic particles behave as paramagnetic as the nanoparticle size is of the order of a single domain. The coercively and saturation magnetization of nanoparticles is increased with superparamagnetic effects. The magnetic properties are also affected by uncompensated surface spins at nanoscale. The uncompensated

surface spins leads to high magnetic moment even for small nanoparticles of non-magnetic (Pd, Au and Pt) materials [106].

Catalytic properties: The active surface atoms of nanoparticles participate in a variety of catalytic reactions (such as hydrogenation, halogenations, oxidation, reduction, decomposition etc.) to improve their efficiency [108,119]. The use of smaller size nanoparticles as compared to larger sized catalyst increase the available surface area for the reaction to takes place. The active surface atoms of nanoparticles also make the surface functionalization process easier and provide the routes for on demand modulation of nanoparticle properties [115].

Mechanical properties: The mechanical properties of the nanoparticles are orders of magnitude higher than that found in bulk materials. The mechanical properties are improved by two factors at nanometer length scales (i) strong surface forces of surface active atoms and (ii) reduced probability of defects like dislocations, impurities etc [108,119]. The mechanical properties (adhesion, hardness, elastic modulus, scratch resistance etc.) at nanometer length scales are significantly improved as compared to bulk materials [121].

Thermodynamic properties: The melting and boiling temperature of bulk materials lowers with reducing particle size to nanometer length scales. This effect is explained by the fact that surface energy increases with increase in surface area and decrease in particle size [119,122]. Nanoparticles also show intrinsic thermodynamic self-purification, which means that the impurities diffuses from the bulk of nanoparticles to its surface under the heat treatment. The purification also improves the chemical and physical properties of the nanoparticles.

1.5.3. Applications of nanoparticles

Under the influence of quantum size and surface atom effects, the nanoparticles have numerous applications diverging in different fields from medicine to photonics to electronics to

food materials etc. Each unique property of nanoparticles is utilized in these applications. For example, the optical properties of nanoparticles are used in photonics, solar cell and sensor applications [109,117,123]. The unique electronic properties of nanoparticles result in applications under the field of nanoelectronics etc [107,117,124]. The superparamagnetism property of magnetic nanoparticles has applications in memory devices, batteries, magnetic resonance imaging (MRI) etc [107,111,125]. The catalytic properties of nanoparticles are utilized in improving the reaction rates for various chemical reactions [126-128]. The enhanced mechanical properties of nanoparticles result in application in formation of high tensile materials such as scratch resistance materials, cutting tools, aircraft components that require high fatigue strength and textile fibers [121,129]. The unique thermodynamic properties of nanoparticles are utilized in applications like generating nanometric heat sources, probing local temperature variations and treating cancer through photo-thermal therapy [109,122].

In addition to applications of individual nanoparticles, there are many applications where conjugation of nanoparticles with different macromolecules results in synergistically improved system properties as compared to individual components [34,39,130]. For example, nanoparticle-polymer composites have attracted attention for engineering flexible materials with improved sustainability and multi-functionality [112,121,131]. Nanoparticle interaction with protein enhances the biocompatibility of nanoparticles, which enables them to be used in the areas of nanobiotechnology and drug delivery [38,131]. Nanoparticle interaction with surfactant gives enhanced colloidal stability having applications in detergent industry, cosmetic industry and design of functional materials [132-133]. Thus, the presence of nanoparticles with protein-surfactant complexes can be utilized to generate new functional materials for different potential applications.

1.6 Layout of thesis

Protein-surfactant complexes are widely studied to understand the stability and structural changes in protein. The self-assembly property of surfactants that leads to the micelle formation makes the protein-surfactant interaction more complex and effective towards applications. It is believed that electrostatic and hydrophobic interactions play an important role in the formation of protein-surfactant complexes. In this thesis, interplay of these interactions (electrostatic and hydrophobic) has been investigated using model protein with different ionic and nonionic surfactants. These protein-surfactant complexes are further examined in the presence of charged nanoparticles. The interaction and resultant structure of nanoparticles with protein-surfactant complexes are reported in this thesis. The thesis consists of seven chapters. A general introduction to the structure and function of proteins, self-assembly of surfactants and characteristics of nanoparticles has already been discussed in this chapter. The different experimental techniques and in particular small-angle neutron scattering and dynamic light scattering for probing structure and interaction of such systems are described in chapter 2. The results of thesis are given in chapters 3 to 6. The structure and interaction of protein-surfactant complexes under different solution conditions are presented in chapter 3. The nanoparticles effect on protein-surfactant complexes with different surfactants are discussed in chapters 4-6. The results of anionic nanoparticles on anionic protein-anionic surfactant complexes (all the components are similarly charged) are discussed in chapter 4. The study on nanoparticle effect on protein-surfactant complexes using cationic surfactant and their comparison with anionic surfactant (chapter 4) are reported in chapter 5. The nanoparticle effect on protein-surfactant complexes using nonionic surfactant and tuning by nonionic-ionic mixed surfactants is studied in chapter 6. Chapter 7 gives the summary of the thesis.

Chapter 2

Characterization Techniques

2.1. Introduction

In soft matter, the research interest lies in investigating the structure-property relationship of individual as well as multi-component systems. The multi-component systems can have the properties of its constituents or the synergistically improved system properties [40,110,134-135]. The specific behaviors of soft materials are highly dependent on size, shape and intermolecular interactions among its constituents [3,12,106,118]. Modifications of these parameters of the constituents can generate new properties for specific applications. The precise understanding of these microscopic properties of the constituents can provide better control and improved properties for different applications. The experimental techniques used for the characterization of materials are decided by the many parameters including the length scale of interest, requirement of the application, nature of the materials, accessibility and availability of the technique. The results of a specific technique depend on its sensitivity to measure a particular parameter. Thus the results from multiple techniques are required to be complemented in order to get reasonable understanding of the system.

The various techniques used for the characterization of soft matter can be broadly classified as macroscopic, microscopic, spectroscopic, and scattering techniques [113,136]. Macroscopic techniques commonly used are rheology, viscosity, turbidity and conductivity etc. These techniques provide information about the bulk properties of the system and are useful to study the role of one component in tuning the bulk behavior of the system.

For example, rheology and viscosity can provide the information about the flow behavior of protein under gelation [137]. The spectroscopic techniques mostly deal with structural transitions occurring at atomic and molecular level in macromolecules due to the presence of other components or varying solution conditions. The different properties of the system are extracted based on different interaction of radiation with matter. The most commonly used spectroscopy techniques are UV-visible spectroscopy, circular dichroism (CD), Raman spectroscopy, fluorescence spectroscopy, nuclear magnetic resonance (NMR) and electron paramagnetic resonance (EPR) spectroscopy. These diverse techniques are utilized to investigate the different aspects of the sample under different conditions. For example, the UV-visible spectroscopy is utilized to find the protein concentration in solution [138]. The circular dichroism (CD) and Raman spectroscopy are utilized to evaluate the extent of the protein unfolding under different solution conditions such as in the presence of surfactants and nanoparticles [53,57,100]. Fluorescence spectroscopy is used to investigate the self-assembly of the surfactants in individual as well as while adsorbed on the proteins [57,139]. Electron paramagnetic resonance (EPR) spectroscopy can be utilized to obtain insight into protein orientation on the nanoparticle surface [140].

The microscopic techniques allow the direct visualization of the materials at mesoscopic length scales. The three broad class of microscopy techniques are optical microscopy, scanning probe microscopy and electron microscopy. The transmission electron microscopy, scanning electron microscopy, atomic force microscopy are commonly used microscopy techniques to study structures at these length scales. The transmission electron microscopy has been widely used to image a wide range of soft matter systems [141-142]. Scattering techniques can provide information about the structure as well as interaction among the particles under native conditions. The most commonly used scattering techniques are

small-angle neutron scattering (SANS), small-angle X-ray scattering (SAXS), static light scattering (SLS) and dynamic light scattering (DLS). SANS, SAXS and SLS can be used to find the structure and interactions of the particles [143]. DLS is used to find the diffusion of particles in solution, which is related to its hydrodynamic size [144].

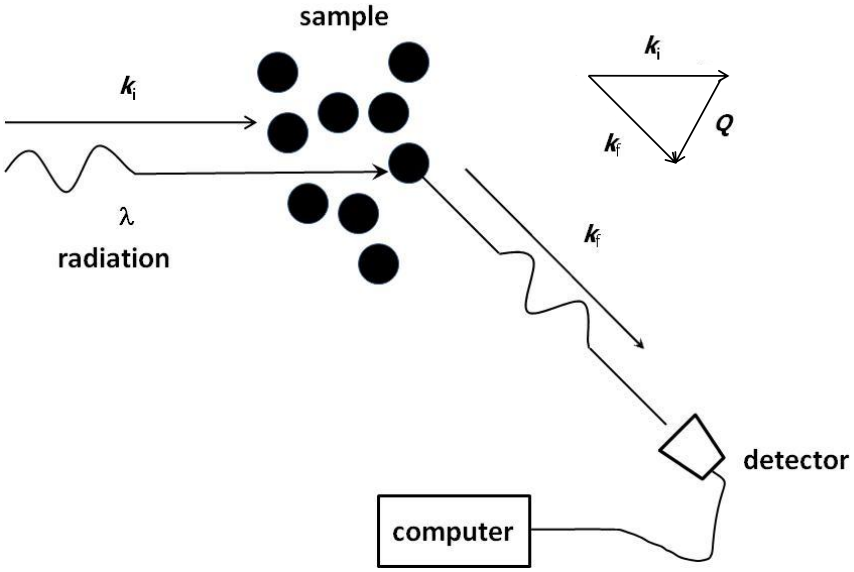

Figure 2.1. Schematic representation of a scattering experiment.

The basic principle governing different scattering techniques (SANS, SAXS and SLS) is same and can be described with minor adjustments for different type of radiations. The schematic of a generalized scattering experiment is shown in Figure 2.1. Here the incident monochromatic beam with wave vector $\boldsymbol{k_i}$ falls on the sample and the scattered beam $\boldsymbol{k_f}$ is detected at detector at a particular scattering angle. The $\boldsymbol{Q}=\boldsymbol{k_f} - \boldsymbol{k_i}$ is called the momentum transfer. The choice of a scattering technique depends on the length scale to be probed. The smallest length scale probed by a scattering technique is of the order of wavelength of the radiation used. In SAXS and SANS, the nanometer length scales can easily be probed using the X-rays and neutrons with wavelength of a few Angstroms. In the case of SLS the larger wavelength (~ 0.5 μm) of laser light restricts the minimum length scale to be probed to hundreds of nanometers. In SANS, SAXS and SLS, the radiation is elastically scattered by a sample and

the resulting scattering pattern is analyzed to provide information about the size, shape of the constituents as well as interactions governing the system behavior [143]. However, DLS works on different principle which measures the time dependent fluctuations in scattering light intensity [145]. It probes the particle size from the diffusion coefficient of particles by measuring the intensity autocorrelation function. The DLS can probe the length scales down to a few nanometers to as high as in micron range. The size range probed by SANS, SAXS, SLS, DLS are compared in Figure 2.2. The type of samples that can be studied by scattering techniques, the sample environment that can be applied, the actual length scale probed and the information that can be obtained, all depend on the nature of the radiation employed. For example, SANS with high penetration depth of neutrons can easily be applied to opaque samples which cannot be studied by DLS. SANS measures the actual size of the particle, whereas DLS measures the hydrodynamic size of the particle. DLS results are biased towards larger length scale present in the system, whereas SANS provides more statistical results. Thus to a large extent these techniques are complementary to each other, whilst sharing many similarities also. The scattering techniques SANS and DLS are used in this thesis and are described in detail in this chapter.

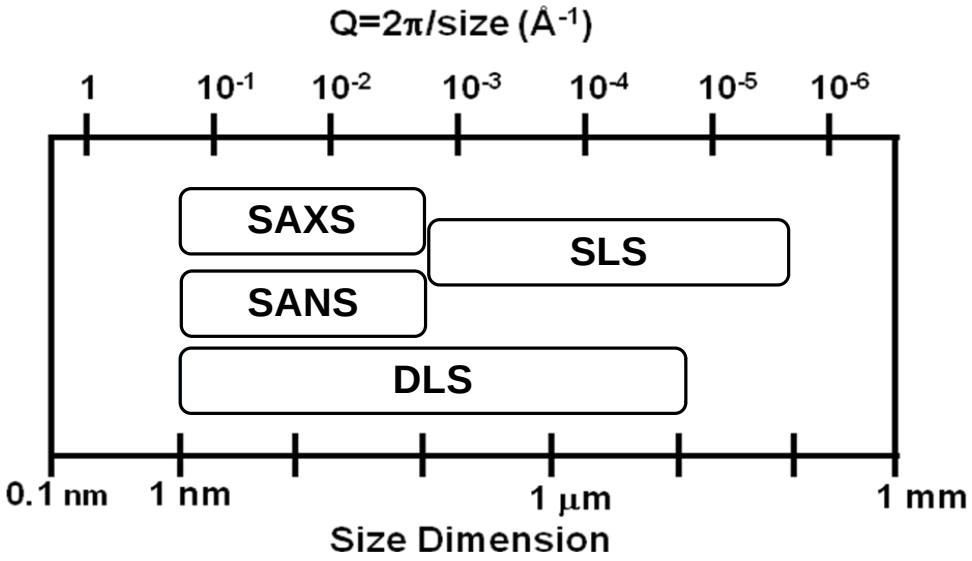

Figure 2.2. Overview of the measureable size range in different scattering techniques.

2.2. Small-angle neutron scattering (SANS)

SANS is one of the useful probes for investigating large-scale structures in mesoscopic length scale [136,143,146-148]. It is a diffraction technique, which involves the scattering of a monochromatic beam of neutrons from the sample and the scattered neutron intensity is measuring as a function of the scattering angle. The scattering angle and wave vector transfer Q are related by relation $Q = 4\pi \sin\theta/\lambda$, where 2θ is the scattering angle and λ is the mean wavelength of incident neutron beam. The wavelength of neutrons used for these experiments is usually in the range 4 to 10 Å. To characterize a typical length scale L in real space, one needs to do a scattering experiment around the $Q = 2\pi/L$. Thus the characterization of larger structures requires the access to lower Q values and corresponding small scattering angles. The Q values covered in a typical SANS experiment are in the range of 0.001 $Å^{-1}$ to 1 $Å^{-1}$. The length scales covered are 1 to 100 nm. Thus SANS is a low resolution technique used to study the structures of materials at larger length scales, unlike conventional diffraction experiments, where the structures of materials are examined at atomic resolution.

2.2.1. Scattering cross section

The incident beam of neutron from the source can be considered as a plane wave with incident wave vector $\boldsymbol{k_i}$. The interaction range of incident neutrons with nucleus is much smaller than the wavelength λ of neutron, thus the scattered wave with wave vector $\boldsymbol{k_f}$ is a spherical wave. The wave vectors of scattered wave from a nucleus at point r in the sample will thus be phase shifted with respect to that scattered at the origin by a phase factor $e^{-i\boldsymbol{Q}.\boldsymbol{r}}$, where $\boldsymbol{Q} = \boldsymbol{k_f} - \boldsymbol{k_i}$ is the wave vector transferred in the scattering process. The scattering cross section describing the flux scattered into the solid angle $d\Omega$ and normalized to the irradiated sample volume (V_T) is called macroscopic differential scattering cross section. The macroscopic differential scattering

cross section for an assembly of scatterers in a macroscopic sample is expressed as [136,143,147-151]

$$\frac{d\Sigma}{d\Omega}(Q) = \frac{1}{V_T}\left\langle \left| \sum_j b_j \exp(-i\boldsymbol{Q}.\mathbf{r_j}) \right|^2 \right\rangle \tag{2.1}$$

where b_j is the scattering length and $\mathbf{r_j}$ is the position vector of jth scatterer in a sample, and the bracket represents an average over all possible orientations.

Since SANS deals with the study of large scale heterogeneities rather than studying location of individual scattering centers, the summation over b_j can be replaced by a volume integral over scattering length density $\rho(\mathbf{r})$ and equation 2.1 transforms to

$$\frac{d\Sigma}{d\Omega}(Q) = \frac{1}{V_T}\left\langle \left| \int \rho(\mathbf{r}) \exp(-i\boldsymbol{Q}.\mathbf{r}) d\mathbf{r} \right|^2 \right\rangle \tag{2.2}$$

where the integration extends over the volume V_T of the sample and $\rho(r)$ is defined as

$$\int_{V_T} \rho(\mathbf{r}) d\mathbf{r} = \sum_j b_j \tag{2.3}$$

The summation in the above equation extends over all the nuclei in the volume V_T.

In general, the particle could be heterogeneous in its composition and it may not have uniform scattering length density. However, to simplify the discussion, we have assumed that scattering length densities in the particle and the matrix are uniform and we can treat the sample as a two-component system. Let ρ_p and ρ_m are the scattering length densities of the particle and the solvent, respectively. The equation 2.2 can be written as

$$\frac{d\Sigma}{d\Omega}(Q) = \frac{1}{V_T}\left\langle \left| \rho_p \int_{V_p} \exp(-i\boldsymbol{Q}.\mathbf{r}) d\mathbf{r} + \rho_m \int_{V_m} \exp(-i\boldsymbol{Q}.\mathbf{r}) d\mathbf{r} \right|^2 \right\rangle \tag{2.4}$$

Here the first term in the integration is over the volume V_p occupied by all particles and the second term is over the volume V_m occupied by the matrix. We rewrite Equation 2.4 as

$$\frac{d\Sigma}{d\Omega}(Q) = \frac{1}{V_T}\left\langle \left| (\rho_p - \rho_m)\int_{V_p} \exp(-i\boldsymbol{Q}.\mathbf{r})d\mathbf{r} + \rho_m \left\{ \int_{V_m} \exp(-i\boldsymbol{Q}.\mathbf{r})d\mathbf{r} + \int_{V_p} \exp(-i\boldsymbol{Q}.\mathbf{r})d\mathbf{r} \right\} \right|^2 \right\rangle \quad (2.5)$$

The uniform integration in the second term of the above equation behaves like a delta function as the size of medium is quite large and corresponding scattering contribution would be at Q value close to zero. This contribution may be neglected for all practical purposes with $Q \neq 0$. After neglecting the second term, the above equation becomes

$$\frac{d\Sigma}{d\Omega}(Q) = \frac{(\rho_p - \rho_m)^2}{V_T}\left\langle \left| \int_{V_P} \exp(-i\boldsymbol{Q}.\mathbf{r})d\mathbf{r} \right|^2 \right\rangle \quad (2.6)$$

where $(\rho_p - \rho_m)^2$ is referred to as the contrast factor.

The integration in equation 2.6 is over all the particles in sample. It may be mentioned that $V_p = nV_TV$, where n is the number density of particles in the sample and V is the average volume of the single particle.

In general, the above integration will contain spatial correlation between the particles and also the effects due to the size distributions. To simplify the above equation, one rewrites Equation 2.6 as

$$\frac{d\Sigma}{d\Omega}(Q) = (\rho_p - \rho_m)^2 V^2 \left\langle \left| \sum_k F_k(\boldsymbol{Q}) \exp(-i\boldsymbol{Q}.\mathbf{R}_k) \right|^2 \right\rangle \quad (2.7)$$

where $\boldsymbol{R_k}$ is the position vector of the k^{th} particle and $F_k(\boldsymbol{Q})$ is the form factor associated with the particle. $F(\boldsymbol{Q})$ is defined as

$$F(\boldsymbol{Q}) = \frac{1}{V}\int_V \exp(-i\boldsymbol{Q}.\mathbf{r})d\mathbf{r} \quad (2.8)$$

and is normalized so that $|F(0)|^2 = 1$.

For the monodisperse system, equation 2.7 can be written as

$$\frac{d\Sigma}{d\Omega}(Q) = (\rho_p - \rho_m)^2 V_p{}^2 \left[n\left\langle \left|F(\boldsymbol{Q})\right|^2 \right\rangle + \left\langle \sum_k \sum_{k'} F_k(\boldsymbol{Q}) F_{k'}^*(\boldsymbol{Q}) \exp[-i\boldsymbol{Q}.(\mathbf{R}_k - \mathbf{R}_{k'})] \right\rangle \right] \quad (2.9)$$

The summation in the second term extends over all the N_p particles in the sample. It is seen that the scattering cross section for a collection of particles consists of two terms, the first term depends on the intraparticle scattering and the second on interparticle scattering.

The intraparticle scattering is the orientational average of the square of the particle form factor and is denoted by $P(Q)$. This term depends on the shape and size of the particle and in principle can be calculated for any geometry.

The interparticle interference term can be evaluated in a closed form only if certain assumptions are made about the correlation between the spacing of the particles and their sizes and orientations. The simplest assumption is that sample contains a monodispersed, spherical particles for which equation 2.9 can be simplified to the form

$$\frac{d\Sigma}{d\Omega}(Q) = n(\rho_p - \rho_m)^2 V^2 P(Q) S(Q) \quad (2.10)$$

where $P(Q) = \langle\, |F(\boldsymbol{Q})|^2 \,\rangle$ is intraparticle structure factor and $S(Q)$ is the interparticle structure factor. In equation 2.10, we confine to situations where particles are randomly oriented in the sample and the scattering is isotropic about the beam axis. $S(Q)$ is given by

$$S(Q) = 1 + \frac{1}{n}\left\langle \sum_k \sum_{k'} \exp[-i\boldsymbol{Q}.(\mathbf{R}_k - \mathbf{R}_{k'})] \right\rangle \quad (2.11)$$

The typical functionality of $P(Q)$, $S(Q)$ and $d\Sigma/d\Omega(Q)$ as a function of Q are plotted in Figure 2.3.

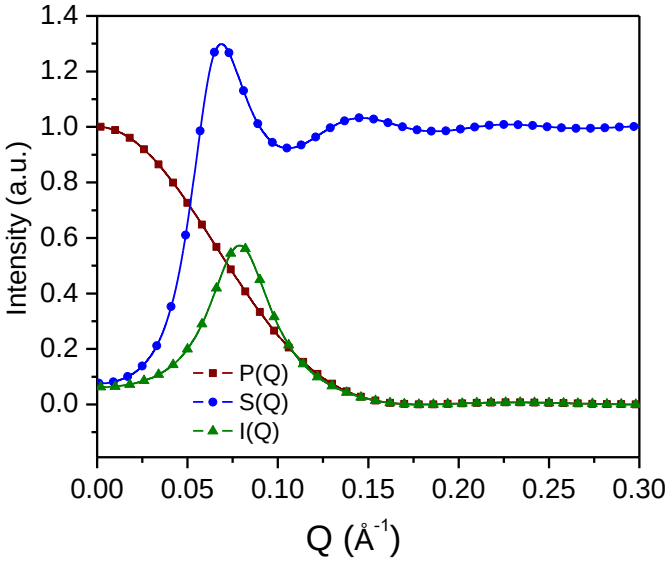

Figure 2.3. Typical curves of $P(Q)$, $S(Q)$ and $I(Q)$.

2.2.2. Determination of intraparticle structure factor

For some of the regular shapes, having an axis of symmetry, the analytical expressions for $P(Q)$ are available in literature [151]. It is assumed that the particles are randomly oriented in the sample so that the theoretical form factors for anisotropic particles have to be averaged over orientation. $P(Q)$ expressions for some standard shapes are given below:

i) Spherical particle

For spherical particle of radius R with uniform scattering length density the intraparticle structure factor is given as [136,143,147,150-151]

$$P_s(Q) = 9\left[\frac{j_1(QR)}{QR}\right]^2 \tag{2.12}$$

where $j_1(x) = \dfrac{(\sin x - x\cos x)}{x^2}$ is first order spherical Bessel function.

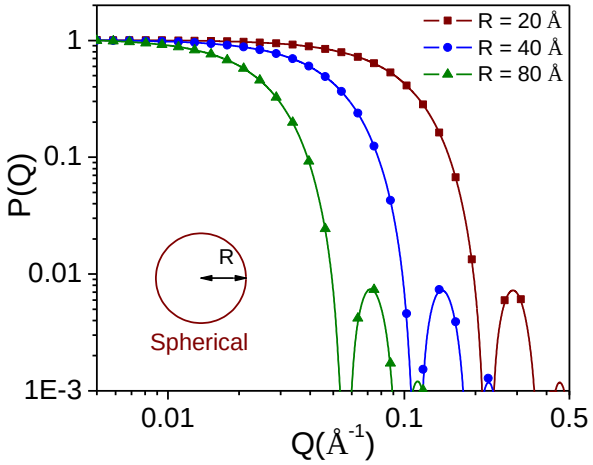

Figure 2.4. *P*(*Q*) plots for a sphere with varying radius.

Figure 2.4 shows the functional form of *P*(*Q*) for spherical particles of radii 20, 40 and 80 Å. It is observed that the width of distribution gets narrowed as the size of the particle increases.

ii) Ellipsoidal particle

The expression for intraparticle structure factor of ellipsoidal particles with its semi axes *R* and *εR*, $P_e(Q)$ can be written as [136,148,151]

$$P_e(Q) = \int_0^{\pi/2} P_s(Q,r)\sin\beta d\beta \qquad (2.13)$$

where $r = R\sqrt{\sin^2\beta + \varepsilon^2\cos^2\beta}$ and β is the angle between semi-major axis and wave vector transfer. Here ε < 1 for oblate ellipsoidal and ε > 1 for prolate ellipsoidal shape of particles.

Figure 2.5 shows the functional form of *P*(*Q*) for spherical, prolate ellipsoidal and oblate ellipsoidal shape of particles with same volume but different axial ratios. The differences in the plots suggest that the different shapes in samples can be determined.

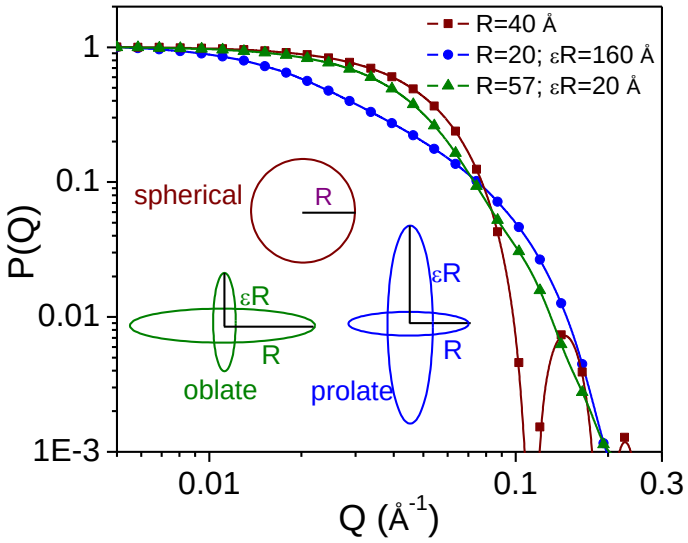

Figure 2.5. *P*(*Q*) plots for spherical, prolate ellipsoidal and oblate ellipsoidal shapes of particles having same volume.

iii) Spherical shell (core-shell particle)

The intraparticle structure factor for spherical shell with inner radius *R* and outer radius *R*+*t*, where *t* is thickness, can be obtained by subtracting the empty core of radius *R* from sphere of radius *R*+*t* with proper weighting by the volumes. Therefore, $P'_{SCS}(Q)$ for spherical shell is written as [136,148,151]

$$P'_{SCS}(Q) = [(\rho_c - \rho_{shell})V_1 \frac{3j_1(QR)}{QR} + (\rho_{shell} - \rho_m)V_2 \frac{3j_1[Q(R+t)]}{Q(R+t)}]^2 \qquad (2.14)$$

where ρ_c, ρ_{shell} and ρ_m are the scattering length densities of core, shell and solvent, respectively. V_1 and V_2 are the volume of the sphere with radius *R* and *R*+*t*, respectively.

Figure 2.6 shows the functional form of *P*(*Q*) for spherical shell with inner radius 40 Å and thickness 10 Å with contrast of shell greater than the contrast of core. The distribution for shell is compared with those with spherical particles of radii 40 and 50 Å. The particle with shell

is found to have the lowest width and also show the oscillations of higher magnitude than those for spherical particles.

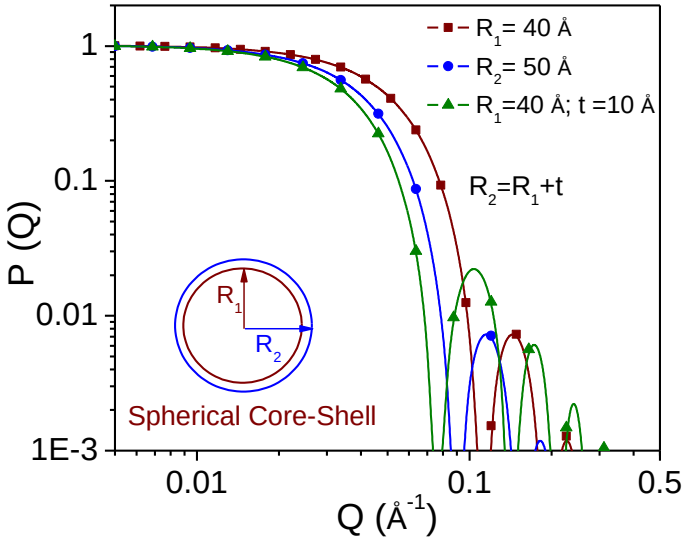

Figure 2.6. *P*(*Q*) plot for a spherical shell as compared with the spherical particles.

iv) Ellipsoidal core-shell particle

The expression for intraparticle structure factor of ellipsoidal core-shell particles $P'_{ecs}(Q)$ can be written as [136,148,151]

$$P'_{ecs}(Q) = \int_0^{\pi/2} P'_{scs}(Q, r_1, r_2) \sin\beta d\beta \tag{2.15}$$

$$P'_{scs}(Q, r_1, r_2) = \left[(\rho_c - \rho_{shell}) V_1 \left\{ \frac{3 j_1(Q r_1)}{Q r_1} \right\} + (\rho_{shell} - \rho_s) V_2 \left\{ \frac{3 j_1(Q r_2)}{Q r_2} \right\} \right]^2 \tag{2.16}$$

$$r_1 = R\sqrt{\sin^2\beta + \varepsilon^2 \cos^2\beta} \tag{2.17}$$

$$r_2 = (R+t)\sqrt{\sin^2\beta + \varepsilon^2 \cos^2\beta} \tag{2.18}$$

where the dimensions R, εR are the semi axes of ellipsoidal particle, and t is the thickness of the shell of the particle. V_1 and V_2 are volumes of core and core along with shell, respectively. The variable β is the angle between directions of semi-major axis and wave vector transfer.

v) Rod-like particle

The intraparticle structure factor of randomly oriented rod-like particles with the radius R and length L (=2l) is given by [136,148,151]

$$P(Q) = \int_0^{\pi/2} \frac{4 j_1^2(QR\sin\theta)}{Q^2R^2\sin^2\theta} \frac{\sin^2[(Ql)\cos\theta]}{(Ql)^2\cos^2\theta} \sin\theta d\theta \qquad (2.19)$$

where θ is the angle subtended by the principal axis of the rod with Q.

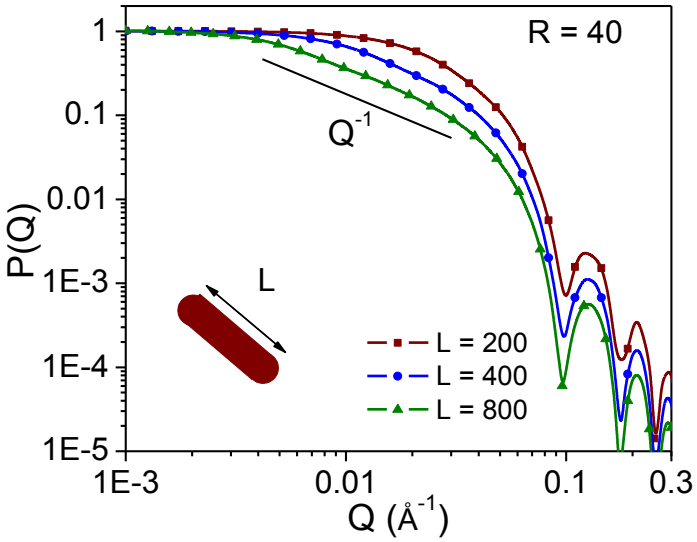

Figure 2.7. $P(Q)$ for rod-like particles having different lengths and fixed radius.

Figure 2.7 shows the functional form of $P(Q)$ for rod-like particles of different lengths and a fixed radius 40 Å. As the length of the particle increases $P(Q)$ on log-log scale shows a linear region in the intermediate Q range ($1/l < Q < 1/R$) with slope -1 of the linear region.

vi) Disc-like particle

The small-angle scattering technique can differentiate between rod-like particles and disc-like particles. The intraparticle structure factor for a disc is given by the same equation as that for a rod (equation 2.19) with the diameter having much larger than the thickness.

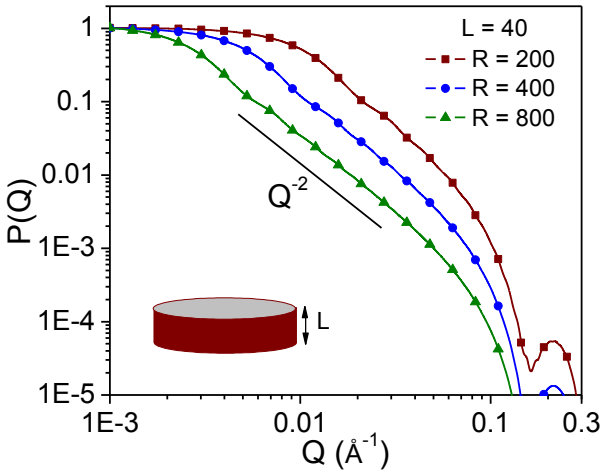

Figure 2.8 *P*(*Q*) plots for disc-like particles having same thickness and varying radius.

Figure 2.8 shows the functional form of *P*(*Q*) for disc like particles with same thickness and different radius. Unlike for a rod-like particle, *P*(*Q*) for a disc-like particle has a slope of -2 in the intermediate *Q* range.

2.2.3. Determination of interparticle structure factor

The interparticle structure factor *S*(*Q*) contributes to the scattering intensity pattern above a particular concentration where the particles start interacting with each other. For these systems *S*(*Q*) ≠ 1 and is governed by correlation between the particles. The correlation depends on interaction between the particles and hence determines the properties of the concentrated system. For an isotropic system, *S*(*Q*) can be written as [136,151]

$$S(Q) = 1 + 4\pi n \int (g(r) - 1) \frac{\sin Qr}{Qr} r^2 dr \qquad (2.20)$$

where $g(r)$ is the radial distribution function and n is the number density of the particles. The radial distribution function is the probability of finding another particle at a distance r from the reference particle centered at the origin. The details of $g(r)$ depend on the interaction potential $U(r)$ between the particles [152-155]. Thus the information about $S(Q)$ can be used to obtain information about the interaction potential $U(r)$.

The colloidal solutions in soft matter are essentially macrofluid on the length scales probed in SANS. The $g(r)$ or $S(Q)$ for these solutions can be calculated using methods as developed for liquids. These colloid solutions are treated as single component model for statistical description of these solutions. The effect of different solution conditions (ionic strength, pH, temperature etc.) and the presence of other components is taken care via an effective interaction potential $U(r)$ [156]. The $U(r)$ could consist of several interaction terms such as screened Coulomb interaction, van der Waals interaction, depletion interactions etc. The $g(r)$ is radial distribution function for a pair of scattering particles. There are two more important functions $h(r)$ and $C(r)$. The $C(r)$ is the direct correlation function which accounts for the direct interactions between the pair of particles and $h(r)$ is the total correlation function which accounts for the interactions through other particles. The functions $g(r)$ and $h(r)$ are related by the expression [157]:

$$g(r) = 1 + h(r) \tag{2.21}$$

Further, The Ornstein-Zernike Equation (OZE) relates the total correlation function $h(r)$ by direct correlation function $C(r)$ as

$$h(r) = C(r) + n\int C\left(r'\right) h\left(\left|\vec{r} - \vec{r}'\right|\right) d^3r' \tag{2.22}$$

The OZE contains two unknowns [$h(r)$ and $C(r)$] and requires an additional relation between $h(r)$ and $C(r)$ to solve the equation. This relation is called closure relation. Depending on the approximations involved, a variety of closure relations have been proposed in the literature. Some frequently used closure relations are as follows:

(i) Mean spherical approximation (MSA) gives [158]

$$C(r) = -\beta U(r), \qquad r > \sigma \tag{2.23}$$

$$h(r) = -1, \qquad r \leq \sigma \tag{2.24}$$

where $\beta = 1/k_B T$ and σ is the particle diameter.

(ii) Percus-Yevick approximation (PYA) gives [152]

$$C(r) = 1 - \exp\left[-\beta U(r)\right] \tag{2.25}$$

(iii) Hypernated chain approximation (HNCA) gives [159]

$$C(r) = -\beta U(r) + h(r) - \ln\left[h(r) + 1\right] \tag{2.26}$$

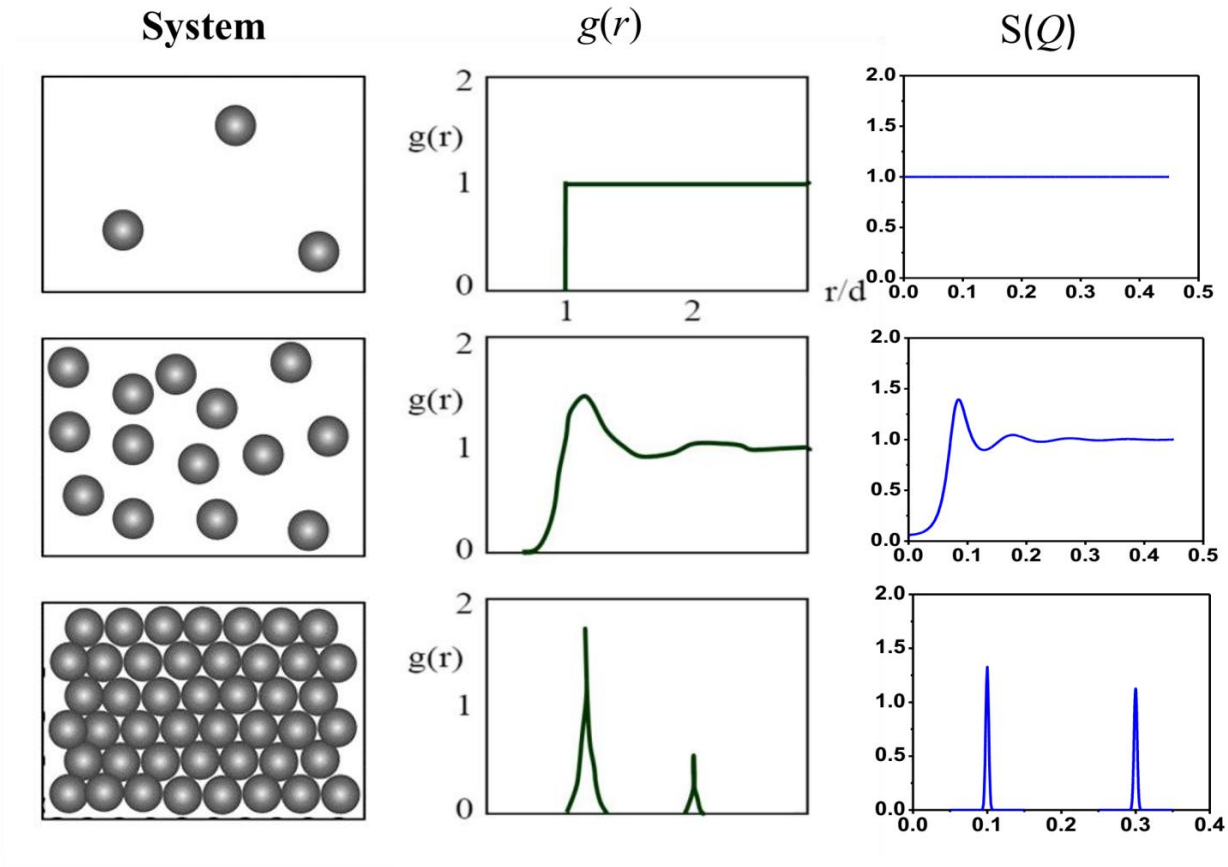

Figure 2.9. Radial distribution function $g(r)$ and corresponding interparticle structure factor S(Q) for dilute, semi-dilute and concentrated systems.

Figure 2.9 shows the radial distribution function $g(r)$ and corresponding interparticle structure factor $S(Q)$ for dilute, semi-dilute and concentrated systems. The $S(Q)$ for colloidal particles in solution as for semi dilute system shows several maxima and minima of decreasing amplitude. The first peak in $S(Q)$ occurs at $Q_{max} \approx 2\pi/d$, where d is the average distance between the particles.

S(Q) for hard sphere potential

In the case of uncharged particles at higher concentrations, hard sphere potential is used which may be defined as

$$\begin{aligned} U(r) &= \infty \quad r \le 2R_{HS} \\ &= 0 \quad r > 2R_{HS} \end{aligned} \tag{2.27}$$

where $2R_{HS}$ is the hard sphere diameter. The analytic solution for the structure factor is obtained using Percus-Yevick approximation as given by [160]:

$$S(Q) = \frac{1}{1 + 24\eta f(R_{HS}Q)/(R_{HS}Q)} \tag{2.28}$$

In this equation, $f(x)$ is defined as follows:

$$\begin{aligned} f(x) = {} & \alpha(\sin x - x\cos x)/x^2 \\ & + \beta[2x\sin x + (2 - x^2)\cos x - 2]/x^3 \\ & + \gamma[-x^4\cos x + 4\{(3x^2 - 6)\cos x + (x^3 - 6x)\sin x + 6)\}]/x^5 \end{aligned} \tag{2.29}$$

and

$$\begin{aligned} \alpha &= (1 + 2\eta)^2/(1 - \eta)^4 \\ \beta &= -6\eta(1 + \eta/2)^2/(1 - \eta)^2 \\ \gamma &= \eta\alpha/2 \end{aligned} \tag{2.30}$$

where η is particle volume fraction.

S(*Q*) *for screened Coulomb potential*

In the case of charged particles, *S*(*Q*) is calculated under rescaled mean spherical approximation [156,158]. This method takes account of a screened Coulomb potential in addition to hard sphere potential between the particles. In the approximation the particle is assumed to be equivalent sphere of diameter σ through a screened Coulomb potential, which is given by

$$U(r) = U_0\sigma\frac{\exp[-\kappa(r-\sigma)]}{r}, \quad r > \sigma \tag{2.31}$$

The contact potential U_0 is given by

$$U_0 = \frac{Z^2e^2}{\pi\varepsilon\,\varepsilon_0\sigma(2+\kappa\sigma)^2} \tag{2.32}$$

where ε is the dielectric constant of the solvent medium, ε_0 is the permittivity of free space and *e* is the electronic charge. The effective charge on the particles (*Z*) is an additional parameter to fit *S*(*Q*) in analyzing the SANS data. The Debye-Hückel inverse screening length (κ) is calculated by

$$\kappa = \left[\frac{8\pi N_A e^2 I}{10^3\varepsilon\, k_B T}\right]^{1/2} \tag{2.33}$$

where *I* is the ionic strength of the solution.

S(*Q*) *for Baxter's sticky hard sphere potential*

The presence of a short-range attractive interaction between the particles is taken care of using Baxter's sticky hard sphere potential [161]. This potential assumes hard sphere repulsion along with the short-range attraction (represented by a thin attractive well). The sticky hard sphere interaction of particles of diameter σ (*2R*) interacting via a thin attractive potential of width Δ is given by

$$\frac{U(r)}{kT} = \infty \quad (0 < r < \sigma) \tag{2.34}$$

$$= \ln\frac{12\ \tau\ \Delta}{\Delta+\sigma} \quad (\sigma \le r \le \Delta+\sigma)$$

$$= 0 \quad (r > \Delta+\sigma)$$

The expression of $S(Q)$ for particles with volume fraction η is expressed as

$$S(Q) = \frac{1}{A^2(Q) + B^2(Q)} \tag{2.35}$$

$$A(Q) = 1 + 12\ \eta\ \left(\alpha\frac{sin(k) - k\,cos(k)}{k^3} + \beta\frac{1 - cos(k)}{k^2} - \frac{\lambda}{12}\frac{sin(k)}{k}\right) \tag{2.36}$$

$$B(Q) = 12\ \eta\ \left(\alpha\left[\frac{1}{2k} - \frac{sin(k)}{k^2} + \frac{1 - cos(k)}{k^3}\right] + \beta\left[\frac{1}{k} - \frac{sin(k)}{k^2}\right] - \frac{\lambda}{12}\frac{1 - cos(k)}{k}\right) \tag{2.37}$$

where

$$\alpha = \frac{1 + 2\eta - \mu'}{(1-\eta)^2}\ ,\ \beta = \frac{-3\eta + \mu'}{2(1-\eta)^2}\ ,\ \mu' = \lambda'\eta(1-\eta) \tag{2.38}$$

$$\lambda' = \frac{6}{\eta}\left[\delta - \left(\delta^2 - \nu\right)^{1/2}\right],\ \delta = \tau + \frac{\eta}{1-\eta}\ ,\ \nu = \eta\frac{1 + \eta/2}{3(1-\eta)^2}$$

and $k = Q(\sigma+\Delta)$. The parameter stickiness (τ^{-1}) provides the information about the strength of adhesion and is given as

$$\tau = \frac{\sigma + \Delta}{12\Delta} exp\left(\frac{V}{kT}\right) \tag{2.39}$$

Figure 2.10 represents the comparison of $S(Q)$ for different interaction potentials of hard sphere, sticky hard sphere and screened coulomb potential for same effective size of particles. The simulated value of $S(Q)$ for Q=0 show maxima for attraction (sticky hard sphere potential) between the particles and minima for repulsion (hard sphere and screened coulomb potential)

between the particles. The hight of maximum of $S(Q=0)$ depends on stickiness (τ^{-1}) between the particles for the case of sticky hard sphere potential. The $S(Q)$ for hard sphere and screened coulomb potential is same above a particular Q value. At lower Q values the screened coulomb potential shows higher depth of minima as Q approaches to zero. The reason of higher depth of minima is strong long range repulsion for the case of charged particles. The position of first correlation peak depends on the average interparticle distance.

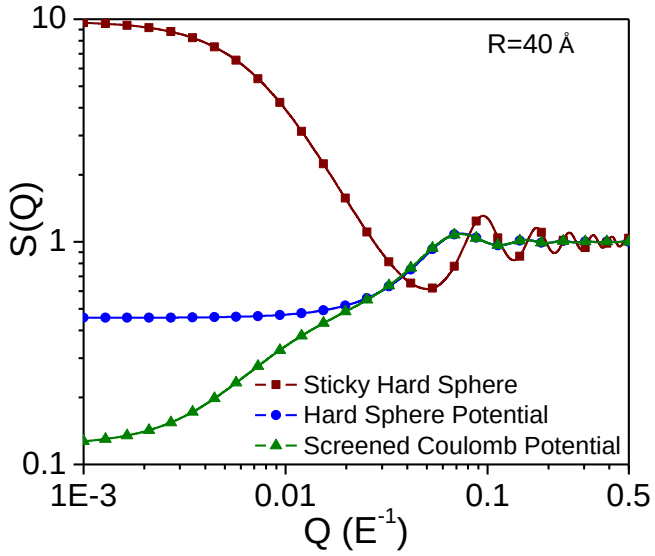

Figure 2.10. Typical S(Q) plots for sticky hard sphere, hard sphere and screened coulomb potentials.

S(*Q*) *for fractal structure*

The origin of the term fractal is due to the fact that some objects or some processes exhibit a self-similarity over a wide length scale and possess a characteristic fractional dimension. Many properties of the fractal systems can often be described by quantities, which are proportional to a power of another quantity. This relation is frequently called a power law. Usually this dependence of $I(Q)$ and correspondingly $S(Q)$ on power of Q is observed when the condition $Q\xi >>1$ is satisfied, where ξ is the upper cut-off length, representing the characteristic distance above which the mass distribution in the system is no longer described by a fractal law.

For mass fractals, where the mass $M(r)$ inside a spherical surface with radius r describing the structure is given by $M(r) \alpha r^d$, $d \leq 3$ [97,162-164]. If the shape of the basic units of the fractals is approximated to be spherical with radius R_p, $P(Q)$ is given by equation 2.12. $S(Q)$ is the interparticle structure factor of the scattering centres and can be expressed as [97,163]

$$S_f(Q) = 1 + \frac{1}{(QR_p)^D} \frac{D\Gamma(D-1)}{[1+(Q\xi)^{-2}]^{[(D-1)/2]}} \times \sin[(D-1)\tan^{-1}(Q\xi)] \qquad (2.40)$$

where $\Gamma(x)$ is the gamma function of argument x. D and ξ are the fractal dimension and the correlation length of the fractal network, respectively.

The expression of $S(Q)$ for surface fractal structure is given by [165-166]

$$S_{sf}(Q) = Q^{-1}\Gamma(5-D_s)\xi^{5-D_s}\left[1+(Q\xi)^2\right]^{\left(D_s-5/2\right)} sin\left[(D_s-1)tan^{-1}(Q\xi)\right] \qquad (2.41)$$

where D_s is the fractal dimension of surface fractal structure. It may be mentioned that the scattering intensity from both kind of fractal structures is governed by power law behavior in a definite Q range.

$$\frac{d\Sigma}{d\Omega}(Q) \sim Q^{-D_m} \qquad \frac{1}{\xi} < Q < \frac{1}{R_p} \quad \text{for mass fractals} \qquad (2.42)$$

$$\frac{d\Sigma}{d\Omega}(Q) \sim Q^{-(6-D_s)} \qquad \frac{1}{\xi} < Q \quad \text{for surface fractals} \qquad (2.43)$$

Figure 2.11 shows the fractal structure factor for various fractal dimension and fixed building block size (R=40 Å) and correlation length (ξ=500 Å). The slope of curve increases with increasing fractal dimension. The higher and lower Q cut off of linearity is decided by the building block size and overall size of fractal in the range given by $2/\xi < Q < 1/R$.

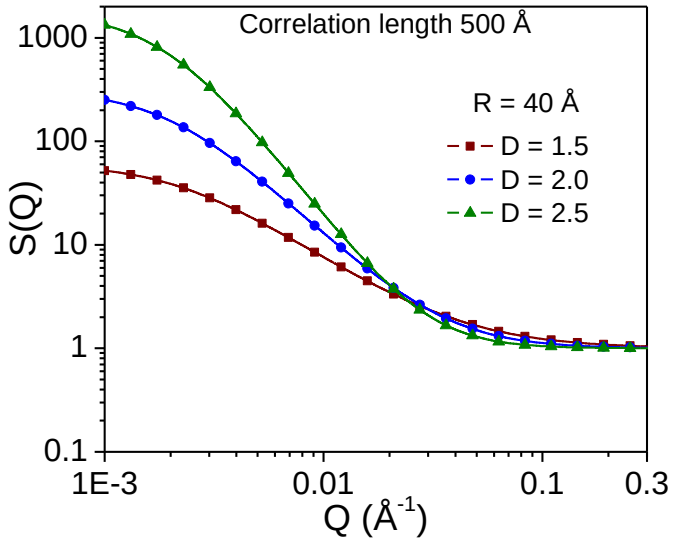

Figure 2.11. S(*Q*) plots for fractal structures with varying fractal dimension.

2.2.4. Concept of contrast in SANS

The major advantage of SANS over SAXS comes from the possibility of contrast variation which comes from the fundamental difference between the interaction mechanism of neutrons and electromagnetic radiation with matter. The X-rays are scattered by electrons surrounding atomic nuclei, whereas neutrons are scattered by the nuclei. The X-ray scattering length increases whereas neutron scattering length varies in a random way with increasing atomic number of the atom (Figure 2.12). The random variation of neutron scattering length allows study of low atomic number elements like hydrogen as well as to distinguish close elements in periodic table having similar scattering length in case of X-rays. Even the two isotopes of same elements can have different neutron scattering lengths. For example the scattering length of hydrogen is negative (= - 0.3741 x 10^{-12}cm) and that deuterium is positive (= 0.6674 x 10^{-12}cm).

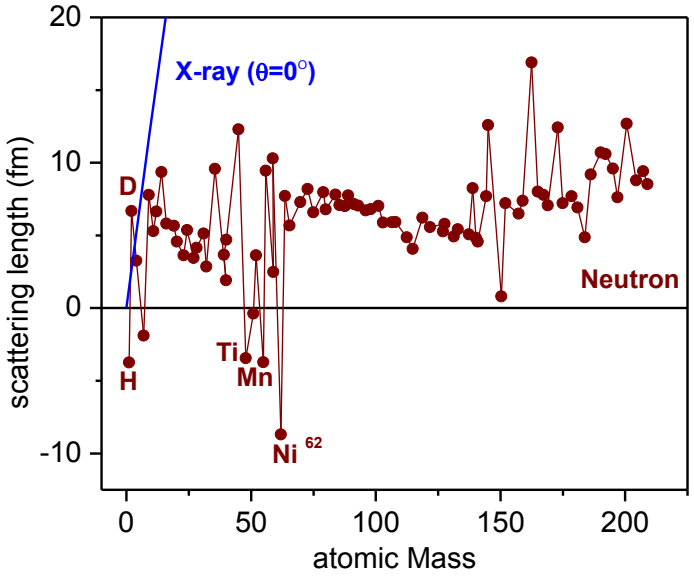

Figure 2.12. Scattering length variation for neutrons and X-rays as a function of atomic mass.

This difference of scattering length between H and D is utilized to have a good contrast between the hydrogenous particle and the solvent by deuterating either the particle or the solvent. Further the scattering length density of solvent can be varied over a long range by using mixed hydrogenated and deuterated solvents. The variation of scattering length density of solvent can be used to contrast match the scattering length density of solvent to the particle. Thus for (ρ_p = ρ_m), the null scattering from that particle is obtained (equation 2.10). This fact is used to study the multi-component system in a solution, where the scattering contribution from the each component can be studied by contrast matching the other component. Various possibilities of contrast variation by mixed D_2O and H_2O as solvent are shown in Figure 2.13.

Figure 2.13(a) shows a hydrogenous spherical particle suspended in H_2O. Let the scattering length densities be ρ_p of the particle and ρ_H of the solvent. In this case ρ_p=ρ_H and thus the particle is not visible for neutrons. However, the solvent can be replaced with D_2O, so the scattering length density of D_2O is ρ_D which is different from ρ_p and thus the SANS scattering pattern is determined from the particle. A spherical core-shell particle is suspended in D_2O as

shown in Figure 2.13(b). The constituents of the inner core are different from those of the outer shell of the particle. Let ρ_{pc} and ρ_{ps} be the scattering length densities of the core and shell. The solvent has a scattering length density $\rho_m=\rho_D$. This scattering length density of solvent can be varied by varying the relative amounts of H_2O and D_2O in the solvent. Thus ρ_m can be either matched with ρ_{ps} so that the SANS scattering pattern is determined by the core alone or ρ_m can be matched with ρ_{pc} so that the SANS scattering pattern is determined by shell alone. The core-shell structure can also be studied by deuterium labeling the particle core and placed in a D_2O solvent. The deuterating of the core of the particle, vary the contrast of core ρ_{pc} equal to ρ_D, thus for neutrons only the shell is visible as shown in Figure 2.13(c).

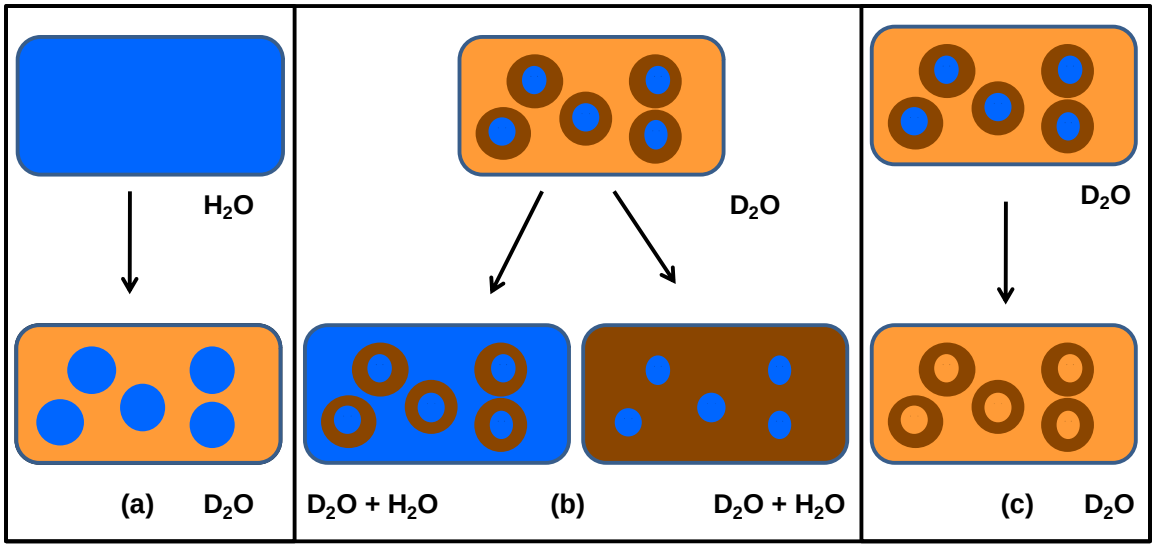

Figure. 2.13. Various possible contrast variations in SANS experiments.

2.2.5. Experimental aspects of small-angle neutron scattering

In a small-angle neutron scattering experiment, the incident neutron beam from the source passes through four different regions (i) monochromator, (ii) collimator, (iii) sample and (iv) detector [146]. The neutron beam from source is first monochromatized using a suitable monochromator (e.g. velocity selector) and is then collimated with a slit arrangement. This monochromatic beam of neutrons is scattered by the sample and the angular distribution of

scattered radiation is recorded using a position sensitive detector (He^3 gas detector). Large distances between the monochromator to the sample and the sample to the detector are kept to ensure fine beam collimation (low $\Delta\theta/\theta$). It is desirable to use circular apertures for defining the incident beam. However, rectangular apertures (slit geometry) are used to gain in intensity. Resolution corrections are more important for slit-geometry as compared to those for pinhole geometry. In a typical SANS instrument, $\Delta\theta/\theta$ ~0.1 and thus it is not necessary to have a high wavelength resolution ($\Delta\lambda/\lambda$ ~ 10%).

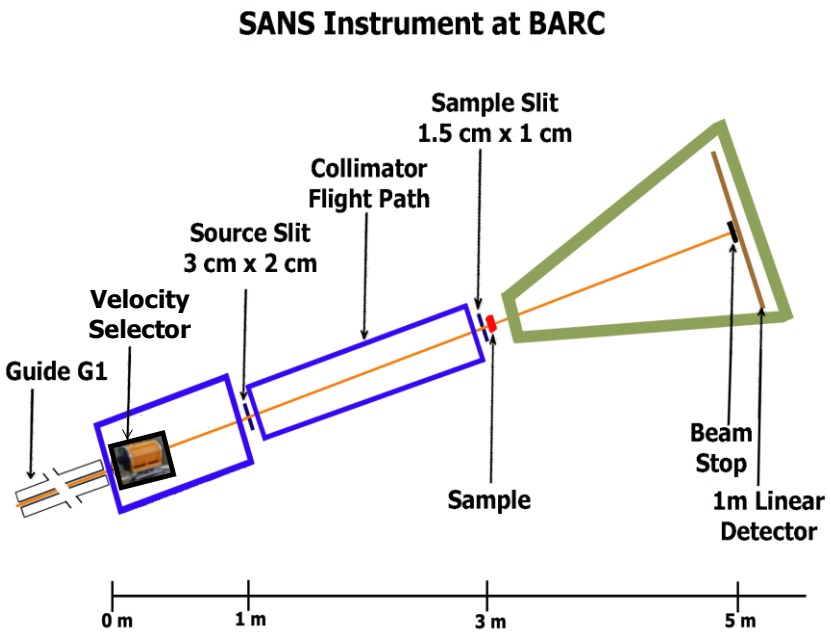

Figure 2.14. Schematic of SANS facility at BARC.

The small-angle neutron scattering experiments presented in this thesis are performed at SANS diffractometer, Dhruva reactor, BARC [146], Swiss Spallation Neutron Source, SINQ, Paul Scherrer Institute, Switzerland [167] and Institut Laue Langevin, Grenoble, France [168]. Figure 2.14 shows the schematic of SANS diffractometer installed at the guide tube laboratory of Dhruva reactor. The neutron beam from the guide is monochromated using a velocity selector. The velocity selector selects the particular velocity neutrons using multi-sloted multi-discs

rotating at very high speed (rpm=4000-7000). The mean wavelength (λ) and wavelength spread (Δλ/λ) of the monochromated beam can be varied in the range 4 to 10 Å and 10 to 20%, respectively. This beam passes through two slits S_1 (2 cm × 3 cm) and S_2 (1 cm × 1.5 cm) before it reaches the sample. Distance between S_1 and S_2 is 2 m and gives an angular divergence of $\pm$0.5º. The angular distribution of neutrons scattered by the sample is recorded using a one-dimensional position sensitive detector. The sample to detector distance is 1.85 m. The *Q* range of the diffractometer is 0.015-0.35 $Å^{-1}$.

The SANS facilities at SINQ, PSI, Switzerland and ILL, France are 40 m long state-of-art instruments [167-168]. These instruments make use of a cold neutron source to get sufficient flux at higher wavelengths. The two-dimensional (96 cm × 96 cm) detector and variable sample to detector distance (1 to 20 m) are used to obtain lower *Q* values and high signal to background ratio. Both the instruments can collect the data in the *Q* range of 0.001 to 1 $Å^{-1}$.

2.2.6. Data reduction and analysis

In a SANS measurement from a sample in solution requires also evaluation of the scattered intensity contributions from the solvent I_{so} and the ambient background I_B. The transmissions of the sample and the solvent should also be determined to correct for the attenuation of neutrons in traversing them. The transmission of the sample T_s should be kept high to minimize multiple scattering effects. The sample cells are usually flat quartz cells with path lengths of 1 to 10 mm. The measured intensity from the sample I_S is corrected for the above various contributions [146-147].

The background is determined by blocking the beam using a cadmium sheet. The measured intensity $I_B(Q)$ consists of the two contributions, namely the room background [$BKG(Q)$] and the fast neutrons [$I_F(Q)$] because cadmium does not block the fast neutrons.

$$I_B(Q) = BKG(Q) + I_F(Q) \tag{2.44}$$

The measured intensity with solvent I_{SO} consists of three terms: first from the fast neutrons [$I_F(Q)$], second from the room background [$BKG(Q)$] and the third is unscattered transmitted intensity from the solvent $I_O T_{SO}$, where T_{SO} is the transmission of the solvent and I_O is the intensity of thermal neutrons in the beam.

$$I_{SO}(Q) = I_O T_{SO} + BKG(Q) + I_F(Q) \tag{2.45}$$

When the scattered intensity ($\boldsymbol{I_S}$) with the sample is measured, we get

$$I_S(Q) = I_O T_S + BKG(Q) + I_F(Q) + I_c(Q) \tag{2.46}$$

where T_S is the transmission of the sample, $I_O T_S$ is the unscattered transmission intensity from the sample and $I_c(Q)$ is the scattered intensity of interest from the sample. The counting time for the experiment is controlled using the monitor detector, which is installed in the incident beam. Solving equations 2.44-2.46 for $I_c(Q)$, we get

$$I_c(Q) = \left[\frac{I_S(Q) - I_B(Q)}{T_S} - \frac{I_{SO}(Q) - I_B(Q)}{T_{SO}} \right] T_S \tag{2.47}$$

In a SANS experiments, the sample is usually taken in a cell, so that it has uniform thickness over the beam area. If $d\Sigma/d\Omega(Q)$ is the differential scattering cross section per unit volume of the sample, the measured scattered neutron intensity is given by

$$I_c(Q) = K T_S t \frac{d\Sigma}{d\Omega}(Q) \tag{2.48}$$

where t is the sample thickness, K is a constant, which depends on instrumental parameters such as incident neutron flux, detector efficiency, solid angle subtended by detector element at sample position etc.

By combining equations 2.47 and 2.48, we get the following expression for the scattering cross section of the sample

$$\frac{d\Sigma}{d\Omega}(Q) = \frac{1}{Kt}\left[\frac{I_S(Q) - I_B(Q)}{T_S} - \frac{I_{SO}(Q) - I_B(Q)}{T_{SO}}\right] \tag{2.49}$$

The instrumental constant K is determined by recording the data from a standard sample (e.g. H_2O, Vanadium, etc.), the measurement thus provides $d\Sigma/d\Omega\,(Q)$ in absolute units (cm^{-1}).

In actual experiment the measured SANS data is a convolution of the theoretical $d\Sigma/d\Omega\,(Q)$ (equation 2.10) and the resolution function of the instrument. The instrument resolution effects have to be taken into account while comparing the calculated and the experimental distributions. In small angle scattering the model function can be written as

$$\mathrm{I}^{mod}\left(\langle Q\rangle\right) = \int R\left(\langle Q\rangle, Q\right)\frac{d\Sigma}{d\Omega}(Q)dQ \tag{2.50}$$

where $R(<Q>,Q)$ is the instrument resolution function. There are three components responsible for the resolution function. These contributions arise from the finite collimation, the wavelength distribution and the spatial resolution of the detector.

The data are analyzed by fitting the calculated scattering intensity (equation 2.50) to that with measured scattered intensity (equation 2.10) using non-linear least square fitting programs.

2.3. Dynamic light scattering (DLS)

Light scattering experiments can be performed as a function of two variables: the scattering angle (θ) and the observation time (t). Thus there are two classes of light scattering techniques: (i) static (elastic) light scattering in which one measure the time averaged scattering intensity at various angles and (ii) dynamic (quasielastic) light scattering in which the time dependence of the intensity is measured. The static light scattering (SLS) yields information on the static properties of the scattering medium such as size and shape of the scatterers at a length scale of the order of wavelength of the light. In dynamic light scattering (DLS), hydrodynamic

size of the particle is measured from its diffusion motion in solution [144-145]. The suspended particles in solution move about or diffuse in a random walk fashion executing Brownian motion. The phases of the scattered waves arriving at the detector fluctuate randomly in time due to random fluctuations in the relative positions of the particles. These fluctuations in the phases of the scattered waves at detector generate random intensity fluctuations with time. These fluctuating bright and dark spots on the detector are called speckles. The information about the fluctuations in scattered light intensity with time is related to the diffusion coefficient of particles undergoing Brownian motion. Smaller particles diffuse with faster speeds and generate rapid fluctuations in scattering light intensities, whereas diffusion of larger particles is more sluggish and result in slowly fluctuating light intensities.

2.3.1. Theory of dynamic light scattering

In dynamic light scattering, the temporal fluctuations in the scattering light intensity are measured using a monochromatic light at a particular scattering angle [144-145]. The DLS technique is also called photon correlation spectroscopy as the technique measures the autocorrelation in scattering light intensity with time. Let $I(t)$ and $I(t+\tau)$ be the scattered light intensity at an arbitrary time t and $t+\tau$ at a particular scattering angle (2θ). The normalized intensity autocorrelation function can be written as [144-145]

$$g^{(2)}(\tau) = \frac{\langle I(t) I(t+\tau) \rangle}{\langle I(t) \rangle^2} \tag{2.51}$$

The $g^{(2)}(\tau)$ is related to the normalized field autocorrelation function $g^{(1)}(\tau)$ as

$$g^{(2)}(\tau) = 1 + \beta \left| g^{(1)}(\tau) \right|^2 \tag{2.52}$$

where β is the spatial coherence factor and depends on the instrument optics and defines the resolution of the measurement.

The spatial coherence factor (β) is defined as the ratio of aperture area of photodetector (A_d) to the coherence area (A_c). The area of a single speckle is known as coherence area (A_c) given by relation $A_c = \lambda^2 r^2 / \pi x^2$, where λ is wavelength of the laser beam used, r is particle to detector distance and x is the radius of the scattering volume. Thus to achieve a high coherence factor ($\beta = A_d/A_c$ and $0<\beta<1$) as well as better resolution, we require optimum aperture area and appropriate pin holes in front of the detector.

The origin of light scattering is polarizability inhomogeneities in the sample. If $\langle\alpha\rangle$ is the average polarizability of the sample, then the excess polarizability of the volume element of the sample at position r is related as $\delta\alpha(\mathbf{r}) = \alpha(\mathbf{r}) - \langle\alpha\rangle$.

The excess polarizability $\delta\alpha(\mathbf{r})$ can be approximate by the fluctuation in solute concentration (δc) for smaller particle sizes (maximum dimension < Q^{-1}) and in dilute solution. In that case, the scattered electric field at time t will be proportional to the fluctuations in solution concentration (δc). The Brownian motion of the particles is responsible for the concentration fluctuations at any time t. The diffusion equation can be used for the temporal evolution of a concentration fluctuation in the case of monodisperse solutions as given by

$$\frac{\partial \delta c(\mathbf{r},t)}{\partial t} = D\nabla^2 \delta c(\mathbf{r},t) \tag{2.53}$$

where D is the diffusion coefficient, expressing c($\mathbf{r}$, t) through a Fourier transform,

$$c(\mathbf{r},t) = \int d^3\mathbf{Q} e^{i\mathbf{Q}\mathbf{r}} c(\mathbf{Q},t) \tag{2.54}$$

we obtain

$$\frac{d}{dt}\int d^3\mathbf{Q} e^{i\mathbf{Q}\mathbf{r}} \delta c(\mathbf{Q},t) = D\nabla^2 \int d^3\mathbf{Q} e^{i\mathbf{Q}\mathbf{r}} \delta c(\mathbf{Q},t) \tag{2.55}$$

and

$$\frac{\partial \delta c(\boldsymbol{Q},t)}{\partial t} = -\boldsymbol{Q}^2 D \delta c(\boldsymbol{Q},t) \tag{2.56}$$

which has the solution

$$\delta c(\boldsymbol{Q},t+\tau) = \delta c(\boldsymbol{Q},t) e^{-\boldsymbol{Q}^2 D\tau} \tag{2.57}$$

For a system fluctuating around its equilibrium state, one does not know the initial condition of $c(\boldsymbol{Q},t)$. However it can be calculated using suitable statistical averages. Multiplying both sides of equation 2.57 with $\delta c(\boldsymbol{Q},t)$ and averaging yields,

$$\left\langle \delta c(\boldsymbol{Q},t+\tau)\delta c(\boldsymbol{Q},t)\right\rangle_t = \left\langle \delta c(\boldsymbol{Q},t)^2\right\rangle_t e^{-\boldsymbol{Q}^2 D\tau} \tag{2.58}$$

where $\langle\rangle_t$ indicates the time average. Since the scattered field amplitude is proportional to the concentration fluctuation, we also have

$$\frac{\left\langle \boldsymbol{E}_s(\boldsymbol{Q},t+\tau)\boldsymbol{E}_s(\boldsymbol{Q},t)\right\rangle_t}{\left\langle \boldsymbol{E}_s(\boldsymbol{Q},t)^2\right\rangle_t} = e^{-\boldsymbol{Q}^2 D\tau} = g^{(1)}(\tau) \tag{2.59}$$

Thus the electric field autocorrelation function decays exponentially with time, where the decay rate ($\Gamma = DQ^2$) is proportional to the diffusion coefficient (D) of particle for fixed momentum transfer Q.

2.3.2. Determination of hydrodynamic size

For a monodisperse system, combining the equation 2.52 and equation 2.59 gives

$$g^{(2)}(\tau) - 1 = \beta e^{-2\boldsymbol{Q}^2 D\tau} \tag{2.60}$$

The experimental values of decay of intensity autocorrelation function are used to calculate the diffusion coefficient of particle from above equation. The Stokes-Einstein relation correlates the diffusion coefficient of particles to its hydrodynamic radius as given by [144-145]

$$R_h = \frac{k_B T}{6\pi\eta D} \tag{2.61}$$

where k_B is the Boltzmann's constant, η is the viscosity of the solvent, and T is absolute temperature.

Intensity autocorrelation function for two different diffusion coefficients (50 and 10 × 10^{-8} cm^2/s) are shown in Figure 2.15. Small particles diffuse rapidly and yield fast intensity fluctuations and rapidly decreasing intensity auto correlation function, whereas larger particles generate slowly decreasing intensity auto correlation function.

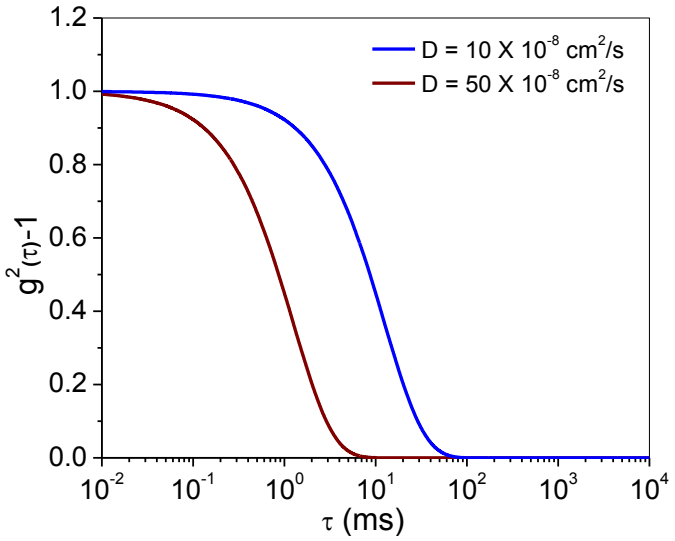

Figure 2.15. Intensity autocorrelation function for particles with different diffusion coefficients.

For a system of polydisperse particles

$$g^{(1)}(\tau) = \int_0^\infty G(D)\exp(-DQ^2\tau)dD \tag{2.62}$$

where $G(D)$ is the distribution of particles with different diffusion coefficients about the mean value. For the monomodal narrow distributation of diffucion coeffecients, the cumulant analysis method is used to calculate the mean value of diffusion coefficient (D_m) and polydispersity index (PI) [169-170]. In this analysis, the equation 2.59 is simplified to

$$g^{(1)}(\tau) = \exp\left[-D_m Q^2\tau + \frac{\mu_2\tau^2}{2}\right] \tag{2.63}$$

where *PI* is given by the ratio of variance (μ_2) to the square of mean of the decay rate ($\Gamma_m=D_mQ^2$).

The intensity autocorrelation function and mean diffusion coefficient under the cumulant analysis approach [equation 2.52 and equation 2.63] are related by

$$g^{(2)}(\tau)-1=\beta\exp\left[-2D_mQ^2\tau+\mu_2\tau^2\right] \tag{2.64}$$

The above equation is used to calculate the mean value of diffusion coefficient (D_m) and polydispersity index ($PI=\mu_2/\Gamma_m^2$).

2.3.3. Experimental aspects of dynamic light scattering

The DLS experiments in this thesis have been carried out using SZ-100 particle size analyzer by Horiba, Japan. The DLS setup consists of 10 mW diode pumped solid state laser used to obtain a monochromatic beam of light with wavelength of 532 nm. The laser beam is converged at the sample using a lens. An ND filter is used in the path of the beam to control the incident intensity at sample and correspondingly optimizing the scattered intensity at the detector. The transmission of the sample is measured using a transmission detector after the sample and in line with the laser beam. The transmission of ND filter is controlled to obtain optimum value of transmission for that particular sample. The optimum transmission ensures the scattering intensity from the sample at the detector will be under the saturation of the detector. The incident laser beam is scattered from the sample at all the scattering angles. The present instrument provides the choice of scattering intensity detection at two scattering angles as perpendicular scattering (90^0) and backscattering (173^0) detection. The scattered light is focused on the detector using a lens. The detector comprises a photo-multiplier tube (PMT) to amplify the photon signal and a photon counter. The intensity fluctuations are converted into electrical pulses and fed into a digital correlator which generates the autocorrelation function. The schematic of DLS instrument is shown in Figure 2.16.

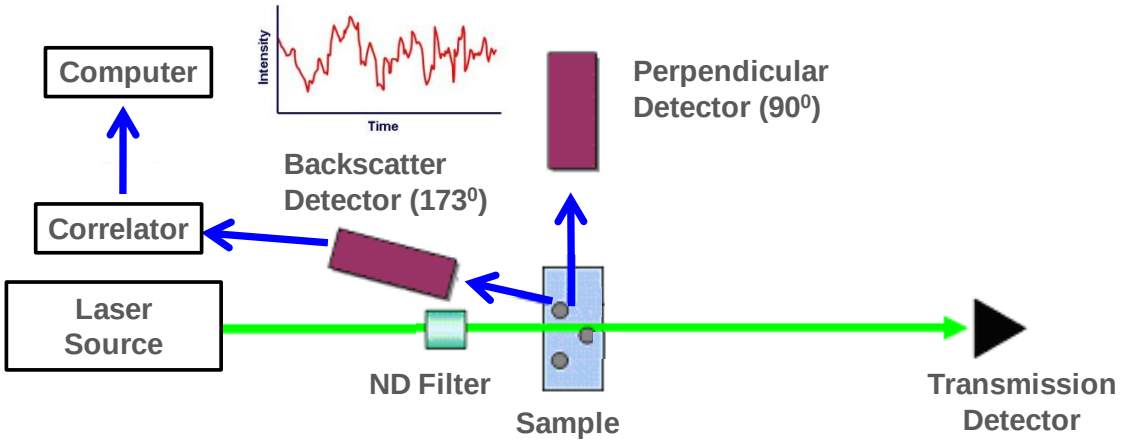

Figure 2.16. Schematic of dynamic light scattering set up.

2.4. Usefulness of scattering techniques for studying multi-components systems

SANS and DLS can be used for characterization of particles having sizes in a length scale (1 to 100 nm) where most of the constituents of soft matter such as protein, micelles, and nanoparticle exist. In particular, SANS is most suitable technique for studying multi-components systems. Usefulness of SANS in investigating multi-component system is multifold and some of the important advantages are:

(i) SANS can probe both interaction and structure in the system [143]. The measured scattering intensity in SANS is the product of the intraparticle structure factor $P(Q)$ and interparticle structure factor $S(Q)$, where the $P(Q)$ provides information on the structure (shape and size) of particles and $S(Q)$ depends on the interaction between particles.

(ii) The unique advantage of SANS to study multi-components systems is easy possibility of contrast-variation in this technique. The scattering due to internal variation of scattering length density could be separately determined if the solvent scattering density is changed isomorphously. The scattering intensity depends on $(\rho_p - \rho_s)^2$, which is square of the difference of scattering length densities of the particle and solvent. Due to large difference between neutron scattering amplitudes of hydrogen and deuterium, SANS is of considerable importance for multi-

component systems unlike the complementary SAXS and light scattering techniques. The constituents of the multi-component systems usually have neutron scattering densities that are between those of H_2O and D_2O. These systems are selectively simplified by matching the scattering density of one of the components with the solvent.

(iii) SANS measures the scattering intensity in the absolute scale and this fact can be used to obtain different levels of information such as particle concentration, internal structure of particle, formation of aggregates.

(iv) In SANS, the measurements are done under native and in-situ conditions. The structures of such systems can be investigated by other techniques such as TEM or SEM. Even though these techniques provide a direct image of the system, they have disadvantage of requiring a frozen or dried sample. The actual structure in such case could be different from those in native solution conditions.

In this thesis, SANS has been mostly used to probe the structure of different protein-surfactant complexes and effect of addition of nanoparticles in these systems. The possibility of contrast-variation is utilized in order to simplify the system by contrast matching the individual components. The protein-surfactant complexes are investigated in chapter 3 under the contrast condition where both the components are visible. The effect of nanoparticles in different protein-surfactant complexes in chapters 3 - 6 are studied for contrast conditions where (i) all the three components are visible, (ii) nanoparticles are contrast-matched and (iii) surfactants are contrast-matched. DLS is used as a complementary technique wherever possible.

Chapter 3

Structure and Interaction of Protein-Surfactant Complexes

3.1. Introduction

The surfactant molecules are known to interact with protein via electrostatic binding at low concentrations and cooperative binding at high surfactant concentrations [36,80,93,97-98,171]. Tuning of the interaction between protein and surfactant by different means leads to a wide range of applications of their complexes [37,83-84,101]. The applications as well as scientific interest of protein-surfactant systems require a detailed understanding of the structure and interaction in these complexes. The interactions of globular proteins with surfactants have been widely reported in the literature [62,66,100,172-177]. Proteins are usually charge stabilized and therefore they have strong interactions with ionic surfactants. Both cationic and anionic surfactants can interact with proteins because of the site-specific interaction of surfactants on the oppositely charged patches of the protein [177-179]. On the other hand, nonionic surfactants, because of the absence of any electrostatic interaction, can have only the hydrophobic interaction with proteins [86,174,177]. The differences in the interaction behavior of ionic and nonionic surfactants suggest that the protein-surfactant interaction is primarily driven by their electrostatic interaction. At low concentrations, the surfactant molecules individually bind to the protein, resulting in the expansion of the folded protein [98,174]. The protein unfolds beyond a critical aggregation concentration of surfactant, where the micelle-like clusters of surfactants are formed around the hydrophobic patches of the protein. These complexes are referred as bead-necklace structures [80,97-98]. There is also interest in knowing innovative ways by virtue of which an

unfolded protein can fold back or prevent protein unfolding [57-59,62]. The competition of electrostatic and hydrophobic interactions plays an important role for this purpose [65,180]. This requires understanding of the role of each of these interactions. In this chapter, the tuning of the protein-surfactant interaction to modify the resultant structure has been examined by varying the surfactant type, ionic strength of the solution, and mixing surfactants. The model protein bovine serum albumin protein (BSA) with the surfactants anionic sodium dodecyl sulphate (SDS), cationic dodecyl trimethyammonium bromide (DTAB), and nonionic polyoxyethylene 10 lauryl ether (C12E10) has been used to study their complexes. The systems are characterized by SANS and DLS techniques. The protein-surfactant interaction and resultant structure are found to be very different for ionic and nonionic surfactants. The work has resulted in a useful method for the refolding of unfolded protein and prevention of surfactant-induced protein unfolding.

3.2. Experimental section

Protein [BSA (catalogue no. A2153)] and surfactants [anionic SDS (catalogue no. L4390), cationic DTAB (catalogue no. D5047) and nonionic C12E10 (catalogue no: P9769)] were purchased from Sigma-Aldrich. The stock solutions of protein (10 wt%) and surfactants (400 mM) were prepared by dissolving the required weighted amounts of components in 20 mM phosphate buffer at pH=7. All the protein-surfactant complexes under study were prepared from the dilution of these stock solutions and in presence of salt (NaCl). The addition of salt is used to reduce the electrostatic interaction between different components. The samples were prepared in D_2O (99.9 atom% D), which provides better contrast for hydrogenous components (protein and surfactant) in neutron scattering experiments [98]. Small-angle neutron scattering experiments were performed using SANS facilities at the Dhruva reactor, Bhabha Atomic Research Centre, Mumbai [146] and SANS-I facility, Swiss Spallation Neutron Source

SINQ, Paul Scherrer Institut (PSI), Switzerland [167]. These two facilities together provide the data collection in a wide wave vector transfer ($Q = 4\pi\sin(\theta/2)/\lambda$, where θ is scattering angle) range of 0.004 to 0.30 $Å^{-1}$ to probe different length scales of the system. The SANS facility at SINQ, PSI allows to achieve lower Q values by increasing the sample-to-detector distance. The measurements were carried out for the fixed concentration of protein (1 wt%) and varying concentration of surfactants in the range of 0 to 100 mM. The effect of ionic strength has been studied by varying the salt concentration up to 0.5 M NaCl. The interaction of protein with mixed ionic-nonionic surfactants (SDS-C12E10 and DTAB-C12E10) is examined for the different mole ratios of two surfactants. All the measured data were corrected and normalized to absolute unit of cross section using standard procedures [181]. DLS experiments were carried out using SZ-100 particle size analyzer (Horiba, Japan) having 10 mW diode pumped solid state laser at wavelength of 532 nm. The scattering angle was kept fixed at 173^{o} during the measurements. The choice of backscatter detection minimizes any contamination from dust particles and multiple scattering from the sample.

3.3. Data analysis

3.3.1. Small-angle neutron scattering

The differential scattering cross section per unit volume ($d\Sigma/d\Omega$) as a function of Q is measured in a SANS experiment. In the case of monodisperse interacting particles, $d\Sigma/d\Omega$ can be expressed as [147,182]

$$\frac{d\Sigma}{d\Omega}(Q) = nV^2\left(\rho_p - \rho_s\right)^2 P(Q)S(Q) + B \tag{3.1}$$

where n is the particle number density and V is particle volume. ρ_p and ρ_s are scattering length densities of particles and solvent, respectively. $P(Q)$ and $S(Q)$ are intraparticle structure factor

and interparticle structure factor, respectively. *B* is the incoherent background arising mostly due to presence of hydrogen in the sample. The expressions of $P(Q)$ for different shapes of the particles and $S(Q)$ for interacting particles as used in modeling individual protein and surfactant systems are described in chapter 2.

The protein-surfactant interaction has been modeled using the bead-necklace model, which is based on random distribution of micelle-like clusters of surfactant along the unfolded polypeptide chain of protein. These structures are usually characterized by mass fractals. The scattering cross section for such system can be expressed as [66,97]

$$\frac{d\Sigma}{d\Omega}(Q) = \frac{N_1^2}{N_p M}(b_m - V_s\rho_m)^2 P_m(Q)S_f(Q) + B \qquad (3.2)$$

where N_p and N_1 are the number density of protein and number density of surfactant molecules that form protein-surfactant complexes. V_s is the volume of surfactant molecule and M is the number of micelle-like clusters attached to a polypeptide chain. The aggregation number of micelle-like clusters in the complex is given by $N=N_1/(N_pM)$. The b_m, ρ_m are the scattering length and scattering length density of surfactant molecule. $P_m(Q)$ denotes the form factor of a single micelle-like cluster. $S_f(Q)$ is the structure factor of a mass fractal as given in equation 2.40.

The data have been analyzed by comparing the calculated model scattering with the experimental data. The corrections for instrumental smearing were made throughout the data analysis. The modeled scattering profiles were smeared by the appropriate resolution function to compare with the measured data. The nonlinear least-square fitting program was used to optimize the fitted parameters in data analysis [151].

3.3.2. Dynamic light scattering

In dynamic light scattering, the temporal intensity autocorrelation function $g^2(\tau)$ is measured using a monochromatic light at a particular scattering angle. It is related to the diffusion coefficient of particle through the relation [144]

$$g^2(\tau) = 1 + \beta \left| \exp(-DQ^2\tau) \right|^2 \tag{3.3}$$

where D is the diffusion coefficient of particle and β is the spatial coherence factor which depends on the instrument optics. The cumulant analysis method is used to calculate the mean value of diffusion coefficient and polydispersity index (equation 2.64). The structural information is obtained through the hydrodynamic radius (R_h) of particles from diffusion coefficient using Stokes-Einstein relation (equation 2.61).

3.4. Results and discussion

3.4.1. Characterization of individual protein and surfactant systems

The individual protein and surfactant systems are characterized using SANS. Data from individual components 1 wt% BSA protein and 40 mM surfactants (anionic SDS, cationic DTAB, and nonionic C12E10) are shown in Figure 3.1. The SANS data of BSA protein are similar to that of dilute system, $S(Q) \sim 1$. The data are therefore fitted with the model of $P(Q)$ alone. It is found that BSA protein macromolecules are oblate ellipsoidal having semi-minor and semi-major axes of 13.6 Å and 42.3 Å, respectively [183]. In the case of micelles unlike protein, SANS data cannot be fitted by $P(Q)$ only and require some contribution from $S(Q)$. This could be because of the higher number density of micelles as compared to that of the protein in the respective systems. The data of ionic micelles (SDS and DTAB) are fitted with $S(Q)$ of interacting charged particles through screened Coulomb interaction, whereas nonionic micelles

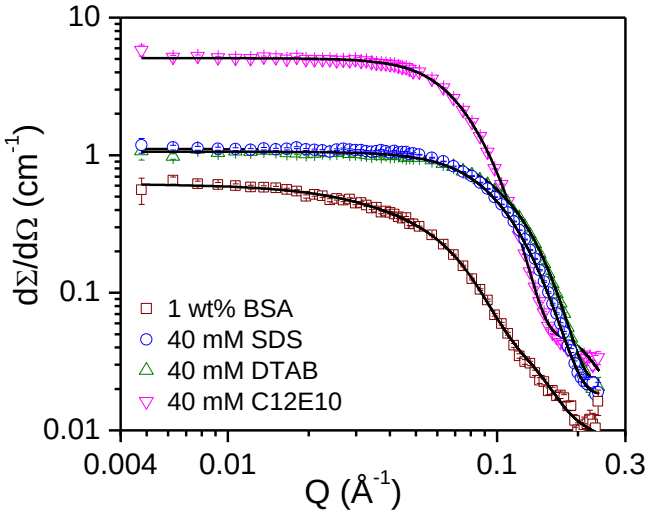

Figure 3.1. SANS data of 1 wt% BSA protein and 40 mM of surfactants (anionic SDS, cationic DTAB, and nonionic C12E10) at pH=7 and 0.2 M NaCl in D_2O.

Table 3.1. The fitted structural parameters of SANS data of individual components of (a) BSA protein and (b) surfactants (anionic SDS, cationic DTAB and nonionic C12E10) at pH=7 and 0.2 M NaCl in D_2O. The aggregation number of micelles is calculated by dividing the micellar volume by the volume of surfactant molecule.

(a) 1 wt% BSA protein

Protein system	Shape	Structural dimensions		
BSA	Oblate ellipsoidal	Semi-major axis R = 42.3±0.5 Å	Semi-minor axis εR = 13.6±0.2 Å	Effective radius $\varepsilon^{1/3}R$ = 29.0±0.4 Å

(b) 40 mM surfactants

Surfactant system	Shape	Structural dimensions				
		Semi-major axis εR (Å)	Semi-minor axis R (Å)	Shell thickness t (Å)	Aggregation number N	Charge Z (e.u.)
SDS	Prolate ellipsoidal	28.6±0.4	16.7±0.2	5.0	95	-23.8±2
DTAB	Prolate ellipsoidal	20.5±0.3	16.7±0.2	5.8	68	+19.7±2
C12E10	Spherical	17.3±0.2	17.3±0.2	12.2*	62	0

*Radius of gyration of hydrophilic chains

of C12E10 are fitted by the hard sphere interaction [158]. The fitted parameters of protein and different micelles are given in Table 3.1. The ionic micelles are found to have the prolate ellipsoidal core-shell structure with semi-minor axis, semi-major axis and shell thickness as 16.7 Å, 28.6 Å and 5.0 Å, respectively for SDS and 16.7 Å, 20.5 Å and 5.8 Å, respectively for DTAB [71]. The SDS and DTAB micelles have aggregation number of 95 and 68 with total charge on them -23.8 and +19.7 e.u., respectively. The lower effective size of the head group gives rise to higher value of aggregation for SDS than DTAB. The C12E10 micelles are fitted with $P(Q)$ of spherical hydrophobic core and shell of hydrophilic Gaussian chains around the core. The radius of core is found to be 17.3 Å and radius of gyration of hydrophilic chain 12.2 Å [184]. The structural parameters of protein and micelles as obtained are in good agreement with the literature [71,185-186].

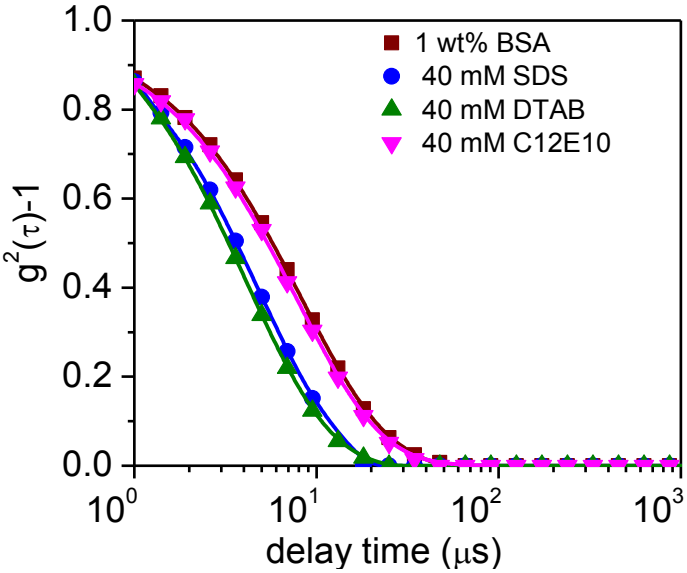

Figure 3.2. DLS data of 1 wt% BSA protein and 40 mM of surfactants (anionic SDS, cationic DTAB, and nonionic C12E10) at pH=7 and 0.2 M NaCl in D_2O.

DLS has also been used to measure the individual protein and surfactants. The intensity autocorrelation function of individual protein (1 wt% BSA) and micelles (40 mM anionic SDS,

cationic DTAB, and nonionic C12E10) are shown in Figure 3.2. The differences in the decay of the intensity autocorrelation function $g^2(\tau)$ correspond to the different values of diffusion coefficients in these systems [144]. The decay of intensity autocorrelation function of BSA protein is found to be slower than all the three different micelles. It follows the decreasing order of decay of intensity autocorrelation function DTAB>SDS>C12E10 for different micelles. The calculated diffusion coefficients and hydrodynamic radii for these systems are given in Table 3.2. It is observed that the hydrodynamic sizes from DLS are larger than the effective sizes of the individual components from SANS. This is consistent with the fact that proteins and micelles are fairly hydrated and thus higher values of the hydrodynamic sizes [187]. The three surfactants used have different charged head groups attached to the same hydrophobic chain, which in the present study allows examining the role of electrostatic vs. non-electrostatic interactions in the protein-surfactant complexes.

Table 3.2. Fitted parameters of DLS data of individual components of BSA protein and surfactants (anionic SDS, cationic DTAB, and nonionic C12E10) at pH=7 and with 0.2 M NaCl in H_2O. The results of DLS data (hydrodynamic radii) are also compared with that of the SANS data (effective radii). The numbers in the brackets of hydrodynamic radii are the values of polydispersity index of the systems.

System	Diffusion coefficient D (10^{-8} $cm^{-2}s^{-1}$)	Hydrodynamic radius R_h(Å)	Effective radius* (Å)
40 mM SDS	81.2	26.5 (0.13)	25.1
40 mM DTAB	86.1	25.0 (0.10)	23.1
40 mM C12E10	56.6	38.0 (0.11)	29.5
1 wt% BSA	53.8	40.0 (0.10)	29.0

*obtained from the SANS data (Table 3.1)

3.4.2. Formation of protein-surfactant complexes

The interaction of surfactant with protein results in the formation of protein-surfactant complexes. SANS data of 1 wt% BSA protein with 40 mM of anionic SDS, cationic DTAB and nonionic C12E10 surfactants in the presence of varying salt concentrations (0 to 0.5 M NaCl) is shown in Figure 3.3. The scattering profile of protein-surfactant complexes with anionic SDS surfactant show systematically decrease in the low Q scattering intensity at lower salt concentrations and in the absence of salt [Figure 3.3(a)]. The scattering depends on the form factor and structure factor contributions. The structure factor contribution can arise from the protein-protein, protein-micelle and micelle-micelle interactions [185,188]. The presence of salt can change both the form factor and structure factor contribution and hence the change in the scattering data. In the case of single-component system, the structure factor $S(Q)$ can be calculated from dividing the scattering intensity by the form factor, where the form factor is determined separately under the solution conditions such that $S(Q) \sim 1$. However, the difficulty comes from to model the structure factor for multi-component system because of increased number of particle-particle correlations. The lower value of scattering in the low Q of SANS data in Figure 3.3(a) in the absence of salt suggests the contribution of structure factor in the data. Therefore, the presence of salt is used to minimize the contributions of structure factor these systems. The data of salt concentrations at 0.2 M NaCl and above almost become flat in the low Q region, where probably the structure factor contribution between protein-surfactant complexes has been suppressed. Therefore, the salt concentration of 0.2 M NaCl was fixed in all the experiments for examining the interaction of BSA protein with SDS surfactant. The effect of salt in the SANS data of 1 wt% BSA protein with 40 mM DTAB and 40 mM C12E10 are shown in Figures 3.3(b) and 3.3(c), respectively. These data unlike those of SDS do not show any significant changes in the scattering with the variation in salt concentration. In the case of BSA with DTAB, it could be because of the charge neutralization by the strong interaction of the two oppositely components in forming their complexes. On the other hand, for nonionic surfactant as expected no noticeable effect of salt is observed [86,139]. The interaction of protein with

different surfactants (SDS, DTAB, and C12E10) has been therefore compared under the same solution condition of 0.2 M NaCl.

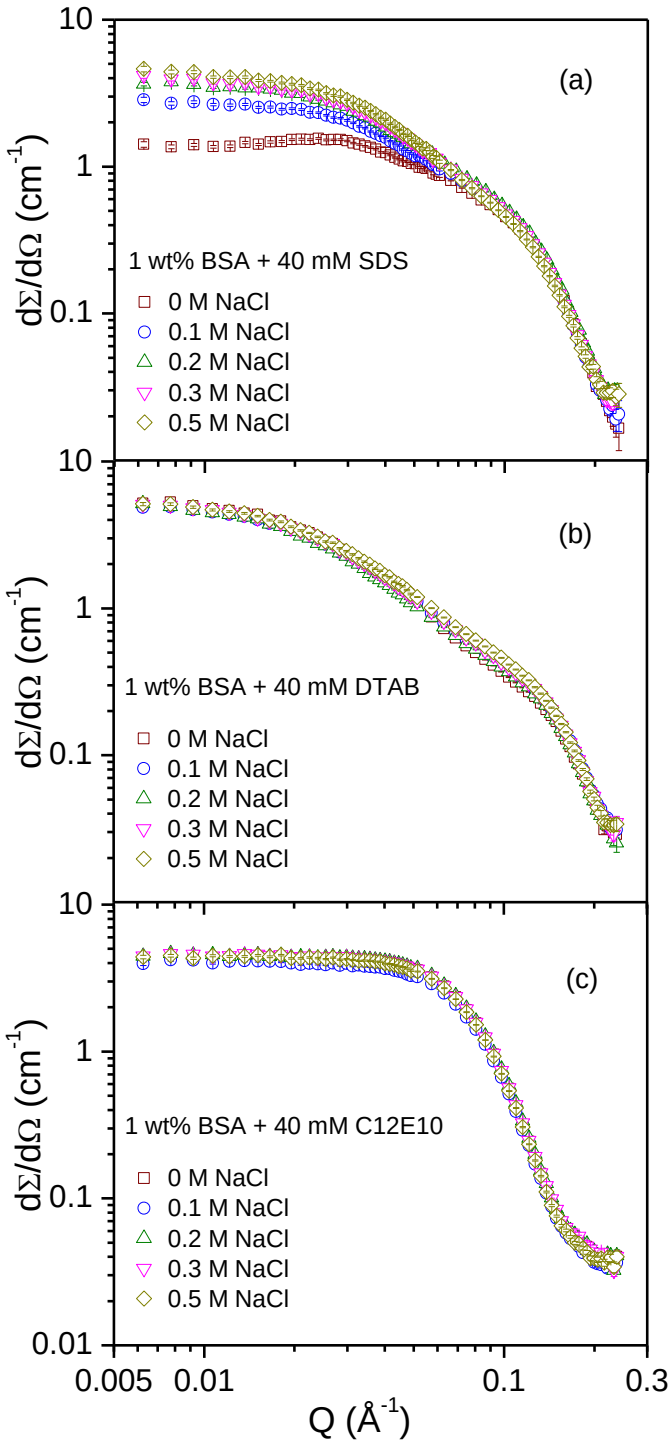

Figure 3.3. SANS data of 1 wt% BSA protein with 40 mM of (a) anionic SDS, (b) cationic DTAB and (c) nonionic C12E10 surfactants for varying salt concentration from 0 to 0.5 M NaCl at pH=7 in D_2O.

The comparison of SANS data of 1 wt% BSA protein with 40 mM of each of anionic SDS, cationic DTAB, and nonionic C12E10 surfactants in presence of 0.2 M NaCl are shown in Figure 3.4. The scattering features of protein-surfactant systems are significantly different for different surfactants. It is observed that for ionic surfactants the scattering of protein-surfactant complex is very different from the sum of individual components. However, the scattering of protein-surfactant complex with nonionic surfactant match to sum of the individual components. This indicates to strong interaction of protein with ionic surfactants (both anionic and cationic) and almost no interaction of protein with the nonionic surfactant. The similar kind of interaction of anionic protein BSA with anionic surfactant SDS and cationic surfactant DTAB can be

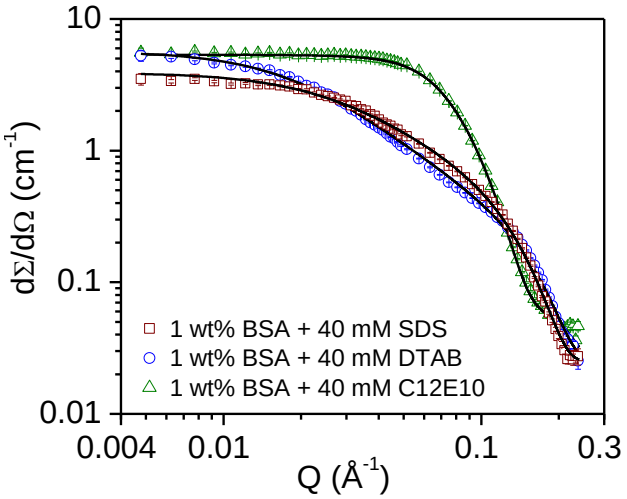

Figure. 3.4. SANS data of 1 wt% BSA protein with 40 mM of anionic SDS, cationic DTAB, and nonionic C12E10 surfactants at pH=7 and 0.2 M NaCl in D_2O.

TABLE 3.3. Fitted parameters of SANS data of protein-surfactant systems characterized by mass fractal structure representing bead-necklace model of their complexes.

System	Micelle radius r (Å)	Correlation length ξ (Å)	Fractal dimension D	Number of micelles M	Aggregation number N
1 wt% BSA+40 mM SDS	18.6±0.2	37.8±2.5	1.70±0.10	5	52
1 wt% BSA+40 mM DTAB	16.8±0.2	56.2±3.0	1.82±0.10	8	34

interpreted as a result of site-specific electrostatic binding of surfactant on the oppositely charged patches of the protein [86,139,177]. The SANS data of protein-surfactant systems for ionic surfactants show linearity in the intermediate *Q* region, which indicates the formation of fractal structure of their complexes [98,163]. This fractal structure is modeled by the bead-necklace model of protein-surfactant complexes representing the micelle-like clusters formed along the unfolded polypeptide chain of protein [80,98]. The high *Q* cut-off, low *Q* cut-off and slope of linearity in SANS data are decided by the building block size (micelle-like cluster), correlation length (overall size of complex) and fractal dimension (packing of micelles) of protein-surfactant complex, respectively [98,189]. The slope of the data in the linear-*Q* range is observed between 1 and 3. Therefore, $S(Q)$ of mass fractal along with $P(Q)$ of spherical micelles has been used in analyzing the scattering profiles [98]. The fitted parameters are given in Table 3.3. There are notable differences in the data of protein complex with the two ionic surfactants. The building block size is smaller and overall size of complex is larger for the case of cationic surfactant (DTAB) than anionic surfactant (SDS). The possible reason for these differences is the site-specific electrostatic binding of cationic and anionic surfactants with different oppositely charged patches on anionic BSA protein. Since there are more negative patches for the binding of cationic surfactant than anionic surfactant, it will lead to more number of cationic DTAB micelles than anionic SDS micelles attached to protein [90,94,139]. The smaller number of micelles for anionic SDS will require larger amount of unfolded protein to pack within the individual micelles, which thereby increases the size of the micelles. The correlation length representing overall size of the protein-surfactant complex is higher for DTAB than SDS as more number of micelles attached with protein for DTAB [139]. The higher number of micelles attached to protein also make the structure of complex more compact as evident from the higher value of its fractal dimension for DTAB than SDS. There is no significant interaction of protein with nonionic surfactant C12E10 observed and the data are fitted with the sum of the scattering from individual components [86,139]. The results are complemented by DLS measurements.

Figure 3.5 shows the intensity autocorrelation functions of DLS measurements of protein-surfactant complexes for all the three anionic SDS, cationic DTAB and nonionic C12E10

surfactants. The intensity autocorrelation functions of protein-surfactant complexes are also compared with the individual BSA protein. In the case of nonionic surfactant, the intensity autocorrelation function of protein-surfactant complex is same to that of the protein. This observation along with the fact that the individual protein and nonionic surfactant have almost similar intensity autocorrelation function (Figure 3.2) supports to non-interaction of two components as consistent with the SANS results [139]. The decay of intensity autocorrelation function of protein-surfactant complexes for ionic surfactants is slowed because of the strong-interaction of protein and surfactant forming larger structures. The hydrodynamic sizes of these complexes are compared with the correlation length of the bead-necklace structure of the complexes by SANS (Table 3.4). The hydrodynamic sizes are again larger than those from SANS analysis because of the hydration associated with the complexes. The hydrodynamic sizes as obtained from DLS for BSA-DTAB and BSA-SDS are almost same as the molecular weights of two compositions are nearly same. On the other hand, SANS technique gives very different correlation lengths for these two systems as the neutrons can see the difference in distribution of micelles and protein in their complex (DTAB micelles are distributed over larger size).

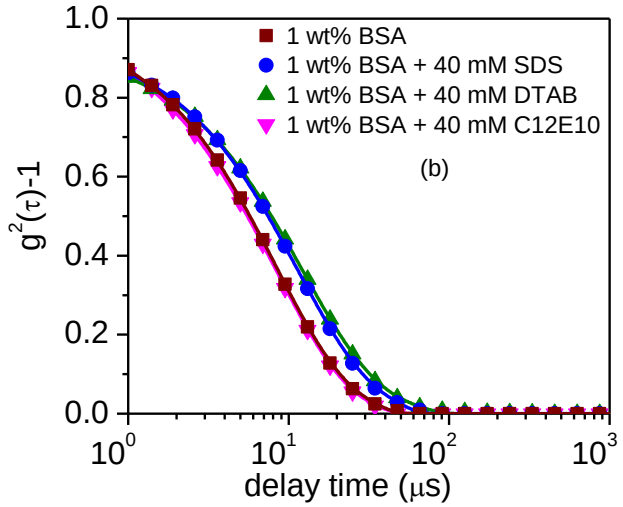

Figure. 3.5. DLS data of 1 wt% BSA protein with 40 mM of anionic SDS, cationic DTAB, and nonionic C12E10 surfactants at pH=7 and 0.2 M NaCl in D_2O. The DLS data of 1 wt% BSA protein is also shown for comparison.

Table 3.4. Fitted parameters of DLS data of protein-surfactant systems at pH=7 and 0.2 M NaCl. The results of DLS data (hydrodynamic radii) are also compared with that of the SANS data (correlation length).

System	Diffusion coefficient D (10^{-8} $cm^{-2}s^{-1}$)	Hydrodynamic radius R_h(Å)	Correlation length* ξ (Å)
1 wt% BSA+40 mM SDS	36.5	59.0 (0.13)	37.8±2.5
1 wt% BSA+40 mM DTAB	34.7	62.0 (0.13)	56.2±3

*obtained from the SANS data (Table 3.3)

3.4.3. Effect of surfactant concentration in protein-surfactant systems

The effect of surfactant concentration on protein-surfactant interaction is examined in Figure 3.6. The figure shows SANS data of 1 wt% BSA protein with varying concentration (0-100 mM) of each of the surfactants (anionic SDS, cationic DTAB and nonionic C12E10). The features of the data for ionic surfactants (anionic and cationic) are same irrespective of the different charge state of the surfactant. The data for nonionic surfactant are different from that with ionic surfactant. The scattering of protein-surfactant complexes for ionic surfactant can be divided into three regions (specific binding, cooperative binding, and saturation region) [80,174]. In specific binding region (low surfactant concentrations), the surfactant molecules bind to the oppositely charged patches on protein through electrostatic interaction but retaining its folded structure. In cooperative binding region (intermediate surfactant concentrations), the interaction of surfactant with protein is enhanced because of dominance of hydrophobic interaction leading to micelle-like clusters formed along the unfolded polypeptide chain of protein. In saturation region (high surfactant concentrations), the excess of surfactant does not bind to the protein. The free surfactant thereafter coexists as micelles with the protein-surfactant complexes in the saturation region. The fitted parameters of the protein-surfactant complexes as a function of ionic surfactant concentration are given in Table 3.5. These parameters are fitted independently as obtained from the different regions of the SANS data. The high Q cut-off

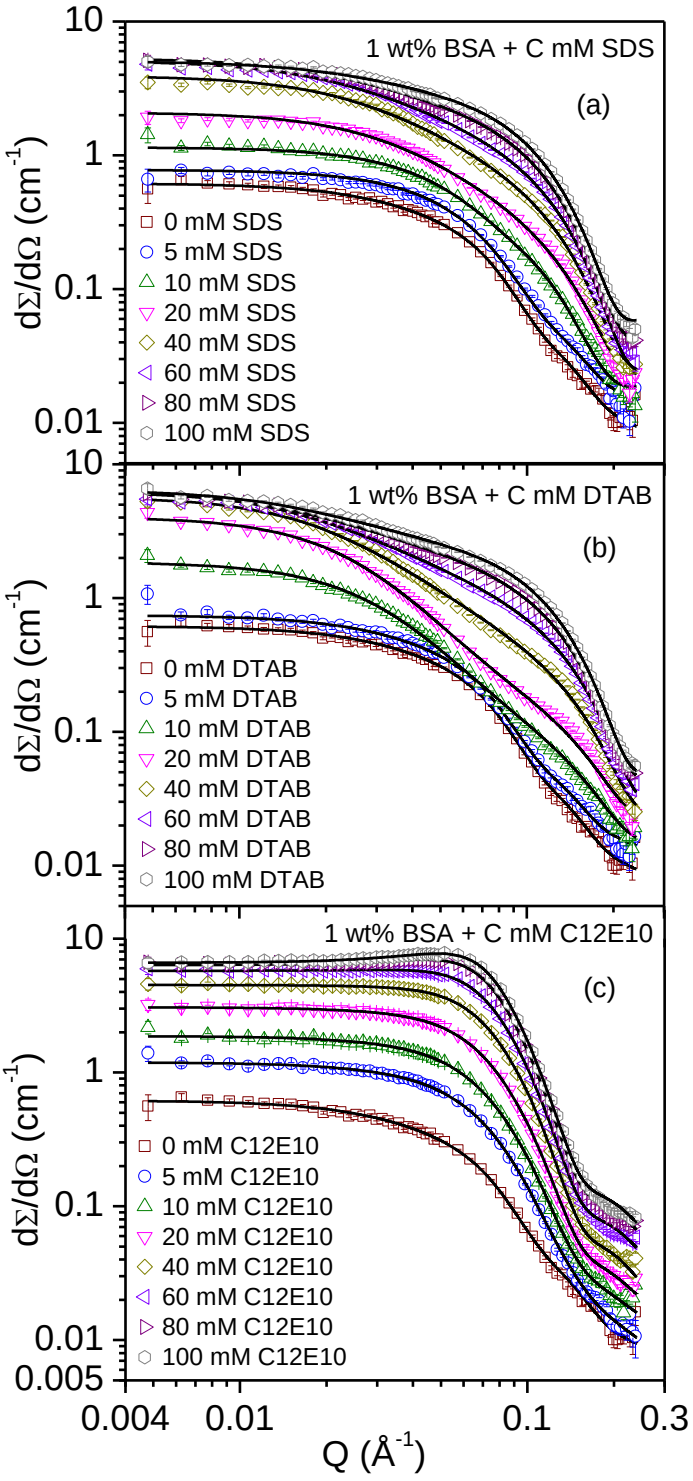

Figure. 3.6. SANS data of 1 wt% BSA protein with varying concentration of surfactants [(a) anionic SDS, (b) cationic DTAB and (c) nonionic C12E10] at pH=7 and 0.2 M NaCl in D_2O.

TABLE 3.5. (a) Fitted parameters of SANS data of protein-surfactant system (1 wt% BSA + C Mm SDS) characterized by mass fractal structure representing bead-necklace model of their complexes.

System	Micelle radius r (Å)	Correlation length ξ (Å)	Fractal dimension D	Number of micelles M	Aggregation number N	Free micelle concentration (mM)
10 mM SDS	18.6±0.2	22.0±3.0	2.41±0.15	1	63	0
20 mM SDS	18.6±0.2	28.0±3.0	2.05±0.10	2	58	0
40 mM SDS	18.6±0.2	37.8±3.0	1.70±0.10	5	52	0
60 mM SDS	18.6±0.2	46.5±3.5	1.50±0.10	6	49	15
80 mM SDS	18.6±0.2	47.6±3.5	1.42±0.10	7	47	32
100 mM SDS	18.6±0.2	49.8±4.0	1.36±0.10	8	46	47

(b) Fitted parameters of SANS data of protein-surfactant system (1 wt% BSA + C Mm DTAB) characterized by mass fractal structure representing bead-necklace model of their complexes.

System	Micelle radius r (Å)	Correlation length ξ (Å)	Fractal dimension D	Number of micelles M	Aggregation number N	Free micelle concentration (mM)
10 mM DTAB	16.8±0.2	24.9±3.0	2.80±0.15	2	38	0
20 mM DTAB	16.8±0.2	36.1±3.0	2.46±0.10	4	35	0
40 mM DTAB	16.8±0.2	56.2±3.5	1.82±0.10	8	34	0
60 mM DTAB	16.8±0.2	62.0±4.0	1.55±0.10	9	32	15
80 mM DTAB	16.8±0.2	63.4±4.0	1.49±0.10	10	31	33
100 mM DTAB	16.8±0.2	65.2±4.0	1.42±0.10	11	30	50

determines the size of the micelle, low *Q* cut-off gives the correlation length of the complex and slope of the data in the intermediate *Q* range provides the fractal dimension of the complex. The number of micelles and micelle aggregation are obtained by the magnitude of scattering intensity on absolute unit and known composition (protein and surfactant concentrations) of the complex [equation 3.2]. The correlation length (extent of unfolding) increases and fractal dimension (packing of micelles in the protein-surfactant complex) decreases with the increase in both anionic and cationic surfactant concentration [98]. The micelle size remains same whereas surfactant aggregation number decreases as unfolded protein component in micelles is increased. Both the ionic surfactants show the binding saturation at almost similar surfactant concentration (~ 45 mM SDS/DTAB) [36,80,91]. There is no interaction of protein with nonionic surfactant C12E10 over the whole concentration range of surfactant and the data are fitted with the sum of the scattering contributions from protein and micelles. The buildup of correlation peak at higher C12E10 concentrations indicates the contribution from inter-micelle correlations.

3.4.4. Protein interaction with mixed surfactants

It has been observed that the interaction of protein with ionic and nonionic surfactants is very different. The ionic surfactant irrespective of its charge nature can unfold the protein,

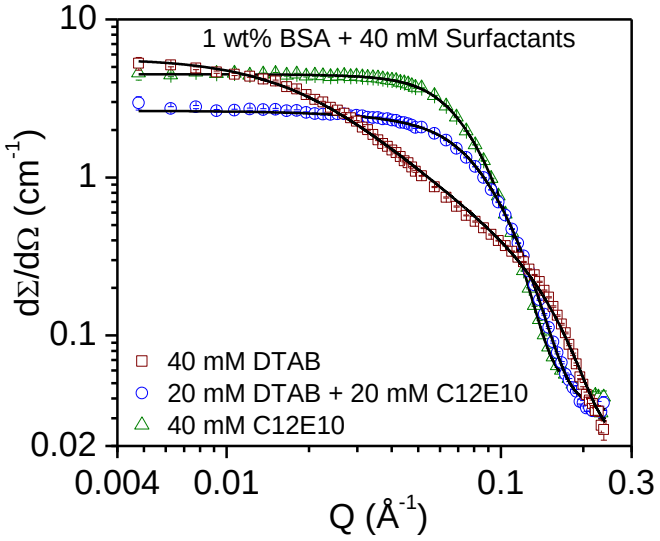

Figure 3.7. SANS data of 1 wt% BSA protein with mixed surfactants (20 mM DTAB and 20 mM C12E10) system at pH=7 and 0.2 M NaCl in D_2O. For comparison the data of 1 wt% BSA protein with 40 mM DTAB and 40 mM C12E10 alone are also given.

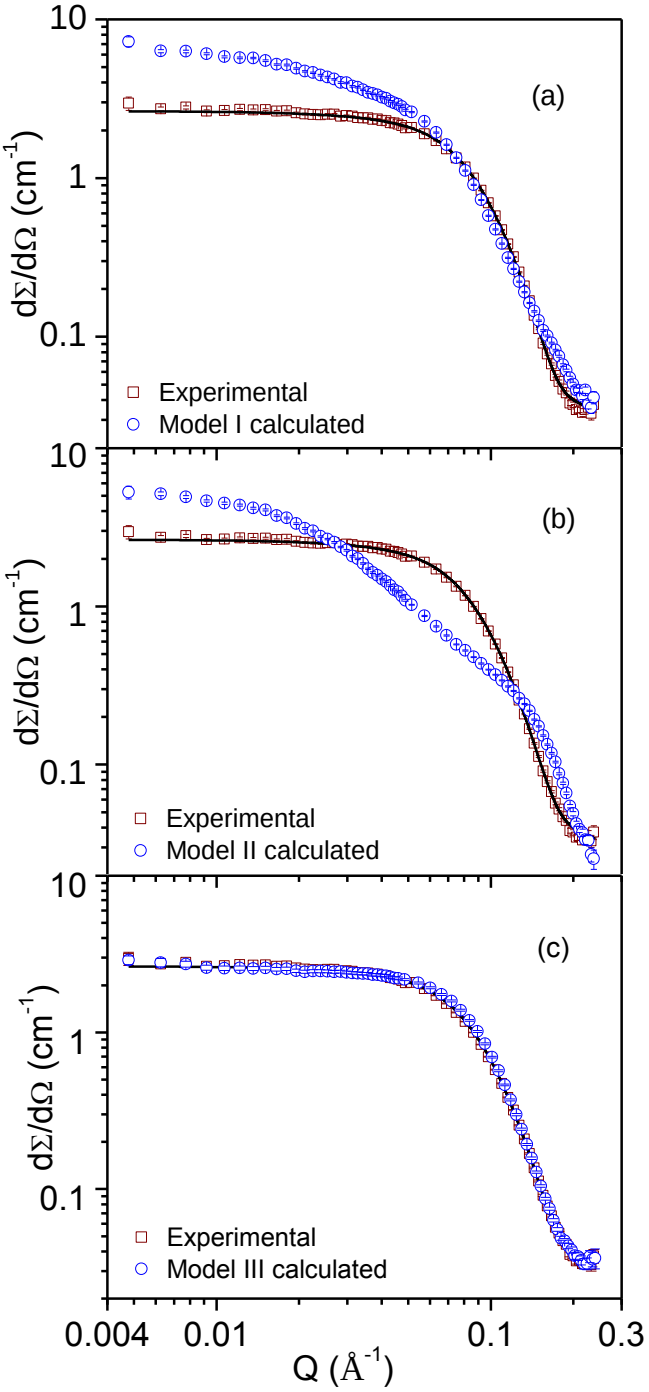

Figure 3.8. The comparison of model scattering with the experimental data of 1 wt% BSA protein with mixed surfactants (20 mM DTAB and 20 mM C12E10) system at pH=7 and 0.2 M NaCl in D_2O. (a) Model I: Nonionic micelles coexist with the complexes of protein-ionic surfactant, (b) Model II: protein forms complexes with mixed ionic and nonionic surfactants and (c) Model III: native protein coexists with the mixed micelles of ionic and nonionic surfactants. The model calculations are done from the experimental data of different individual and mixed components.

whereas nonionic surfactant does not alter the native structure of protein. The effect of these two types of surfactants (ionic and nonionic) together with protein has been examined. The data of 1 wt% BSA with 20 mM DTAB and 20 mM C12E10 mixed surfactant system are compared with 1 wt% BSA with 40 mM DTAB and 1 wt% BSA with 40 mM C12E10 in Figure 3.7. The scattering features of protein with mixed surfactants are very different from that of protein-ionic surfactant system but similar to protein-nonionic surfactant system. The linearity in the intermediate *Q* range of protein-ionic surfactant system is completely diminished in the case of mixed surfactants system and attains the features close to that of protein with nonionic surfactant alone. The three possible models can be considered for the interactions in these mixed systems. (i) Only ionic surfactant interacts with protein. This leads to ionic surfactant induced unfolding of proteins, which coexists with non-interacting nonionic micelles. (ii) Both ionic and nonionic surfactants interact with protein. The system primarily consists of mixed surfactant induced unfolded proteins. (iii) None of the surfactant interacts with the protein. In this case, the system will have folded protein coexisting with mixed micelles. The comparison of scattering from different models with experimental data is shown in Figures 3.8(a-c). The Figure 3.8(a) compares the scattering from protein-mixed surfactants system with the sum of experimental scattering from protein-ionic surfactant and nonionic micelles. The vast difference in model and measured scattering curves rules out the possibility of coexistence of non-interacting nonionic surfactants and interacting ionic surfactant with protein. The model scattering of protein interaction via mixed micelles of ionic and nonionic surfactants also do not match with the experimental data [Figure 3.8(b)]. The experimental data match with the model scattering of non-interacting micelles of ionic and nonionic surfactants coexisting with the unperturbed folded protein [Figure 3.8(c)]. The data in Figure 3.7 have been therefore fitted with the model of native folded protein coexisting with mixed micelles of ionic and nonionic surfactants. It is an interesting observation where the presence of nonionic surfactant makes ionic surfactant from interacting to non-interacting to the protein. This mechanism can be understood based on the competition of charge driven binding of ionic surfactant with protein to that of hydrophobic driven mixed micellization of ionic surfactant with nonionic surfactant. Our results show that the

dominance of hydrophobic interaction of ionic and nonionic surfactants over the electrostatic binding of ionic surfactant with protein governs the structure of these systems.

The nonionic surfactant induced refolding of ionic surfactant mediated unfolded protein has been analyzed under different mole fraction of ionic-nonionic mixed surfactants. Figure 3.9 shows the SANS data of 1 wt% BSA protein with 40 mM of mixed cationic DTAB-nonionic C12E10 surfactants with varying mole fraction of C12E10 surfactants. It is clearly visible that the interaction of protein with mixed surfactants depends on the mole fraction of the nonionic surfactant. The scattering features of protein-mixed surfactant complex are similar to that of the protein-ionic surfactant complex up to 0.2 mole fraction of nonionic surfactant, whereas data of 0.4 mole fraction and beyond resemble to that of protein-nonionic surfactant system. These data have been used to model the nonionic surfactant-dependent modification in the interaction of ionic surfactant with the protein. The data suggest that the binding of ionic surfactant to protein decreases with the increase in the concentration of nonionic surfactant. This has been modeled through the decrease in the number of micelles attached to unfolded protein in the protein-ionic surfactant complex as the concentration of nonionic surfactant is increased Table 3.6. The number of ionic micelles attached to unfolded protein decreases by about 50% for the 0.2 mole fraction of nonionic surfactant, whereas all the ionic micelles detached for 0.4 mole fraction and beyond to form the mixed micelle with the nonionic surfactant.

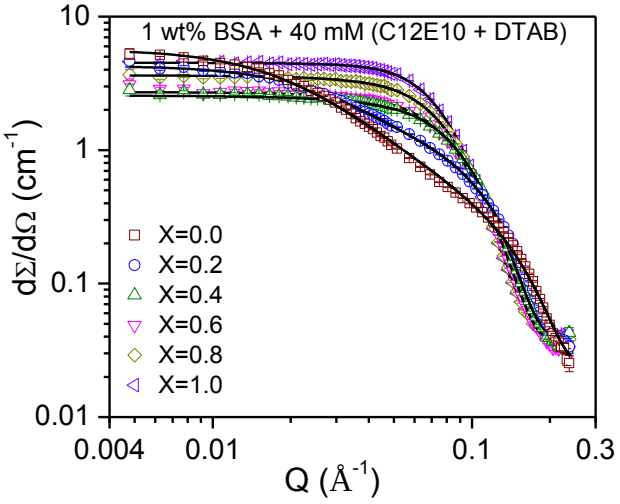

Figure 3.9. SANS data of 1 wt% BSA protein with 40 mM of mixed surfactants (DTAB and C12E10) with varying mole fraction (X) of nonionic surfactant at pH=7 and 0.2 M NaCl in D_2O.

Table 3.6. Fitted parameters of SANS data of protein-mixed surfactant system of (a) 1 wt% BSA + 40 mM DTAB-C12E10 and (b) 1 wt% BSA + 40 mM SDS-C12E10) characterized by mass fractal structure, representing bead-necklace model of protein-ionic surfactant complex coexisting with mixed micelles. For mole fraction of nonionic surfactant 0.4 and beyond, the systems BSA-DTAB-C12E10 and BSA-SDS-C12E10 consist of native unfolded protein coexisting with the 100% fraction of mixed micelles.

(a) BSA-DTAB-C12E10 system

Mole fraction of C12E10	Micelle radius r (Å)	Correlation length ξ (Å)	Fractal dimension D	Number of micelles attached n	Aggregation Number N	Fraction of Free Mixed Micelles (%)
0	16.8±0.2	56.2±3.5	1.82±0.10	8	36	0
0.2	16.8±0.2	31.7±4.0	2.32±0.15	4	37	48

(b) BSA-SDS-C12E10 system

0	18.6±0.2	37.8±3.5	1.70±0.10	5	52	0
0.2	18.6±0.2	26.0±4.0	2.40±0.15	2	60	55

DLS measurements of protein-mixed surfactant systems are shown in Figure 3.10. Figure 3.10(a) shows the variation in intensity autocorrelation function with the change in the mole fraction of nonionic surfactant in protein-mixed (cationic DTAB-nonioic C12E10) surfactant system. The decay of intensity autocorrelation function becomes faster indicating ionic micelles detachment from the protein-ionic surfactant complex with the increase in the mole fraction of nonionic surfactant. The change in the effective hydrodynamic size of the system with varying mole fraction of nonionic surfactant is plotted in the Figure 3.10(b). The hydrodynamic size decreases up to 0.4 mole fraction of nonionic surfactant and thereafter remains constant to that of the folded protein. The effect of addition of C12E10 to BSA-SDS is also found similar to that of BSA-DTAB [Figure 3.11 and Table 3.6 (b)]. Thus, both the SANS and DLS techniques

independently confirm the nonionic surfactant-dependent refolding of the ionic surfactant-induced unfolded protein.

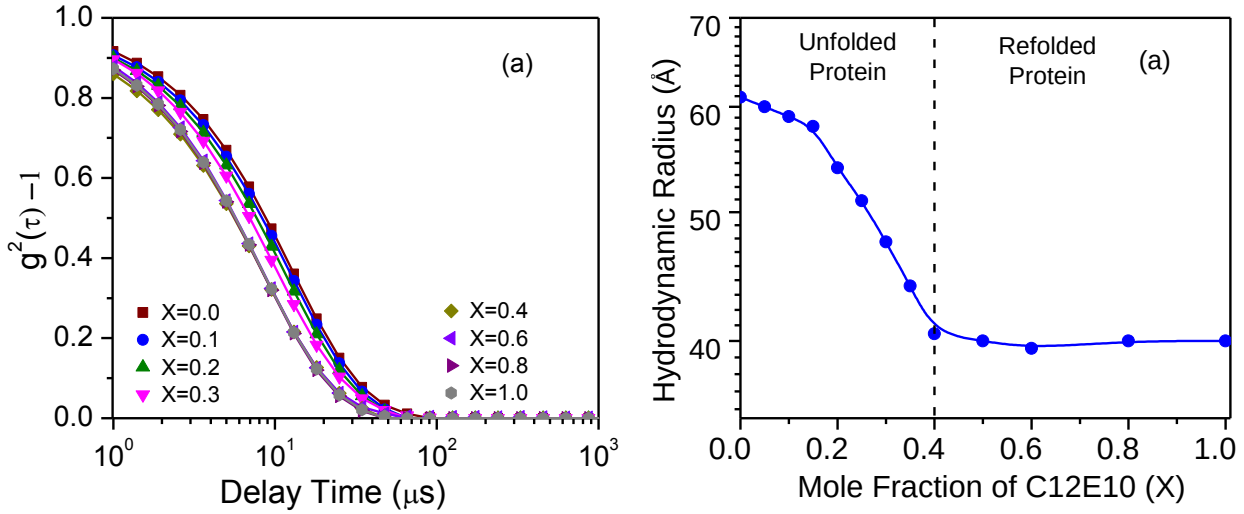

Figure 3.10. (a) DLS data of 1 wt% BSA protein with 40 mM of mixed surfactants (DTAB and C12E10) with varying mole fraction (X) of nonionic surfactant at pH=7 and 0.2 M NaCl in D_2O. (b) The variation in hydrodynamic radii of 1 wt% BSA protein with 40 mM of mixed surfactants (DTAB and C12E10) with varying mole fraction (X) of nonionic surfactant at pH=7 and 0.2 M NaCl.

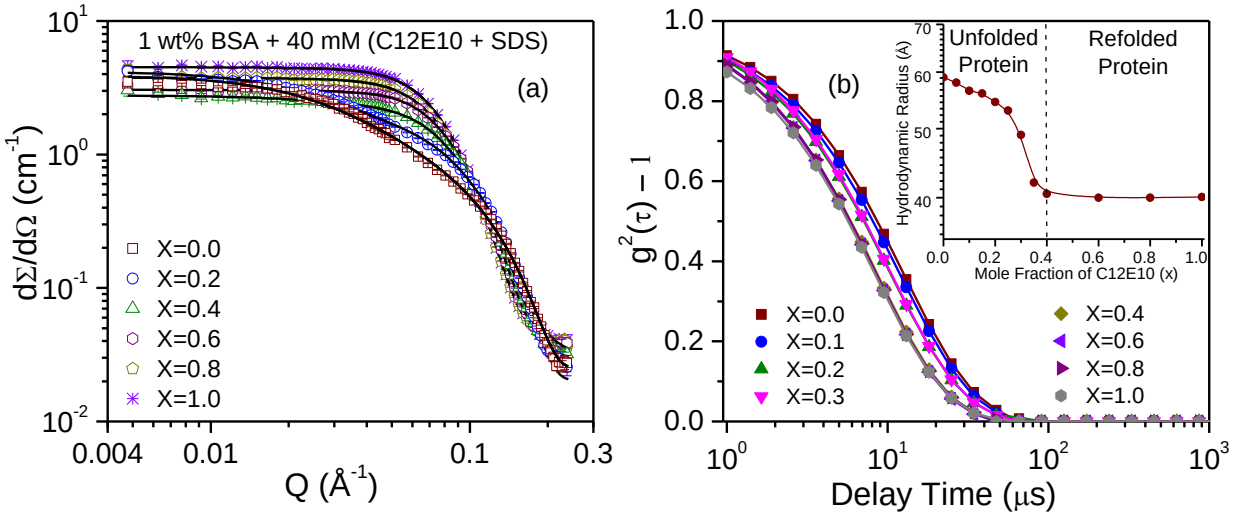

Figure 3.11. (a) SANS and (b) DLS data of 1 wt% BSA protein with 40 mM of mixed surfactants (SDS and C12E10) with varying mole fraction (X) of nonionic surfactant at pH=7 and 0.2 M NaCl in D_2O. The inset in Figure (b) shows the variation of effective hydrodynamic radius with the change in the mole fraction of nonionic surfactant.

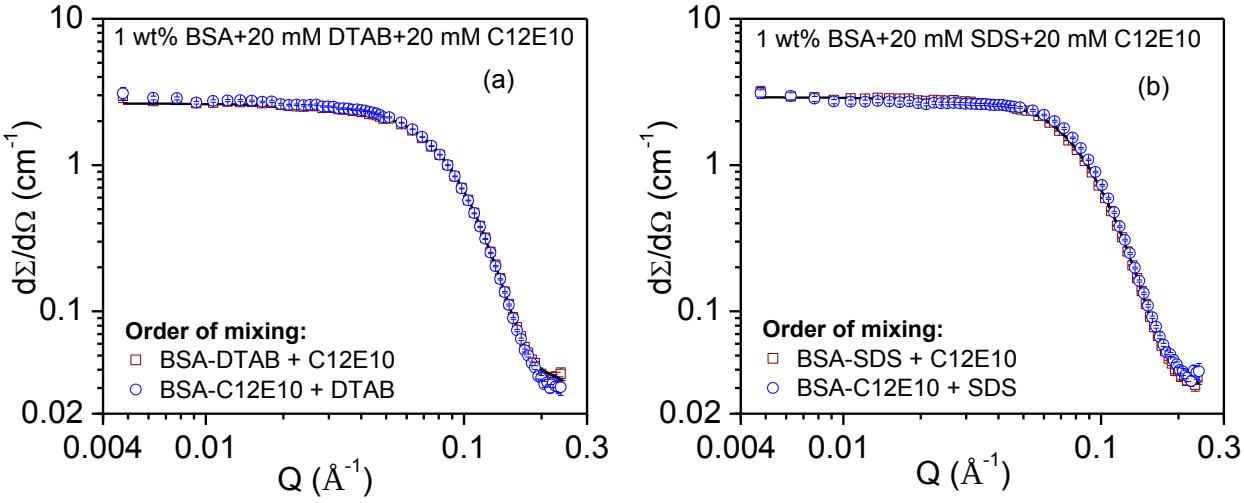

Figure 3.12. SANS data of 1 wt% BSA protein with 40 mM of mixed surfactants (a) DTAB and C12E10 and (b) SDS and C12E10 at 1:1 mole fraction of ionic and nonionic surfactants at pH=7 and 0.2 M NaCl in D_2O. The data are compared with the change in the order of mixing of ionic and nonionic surfactants.

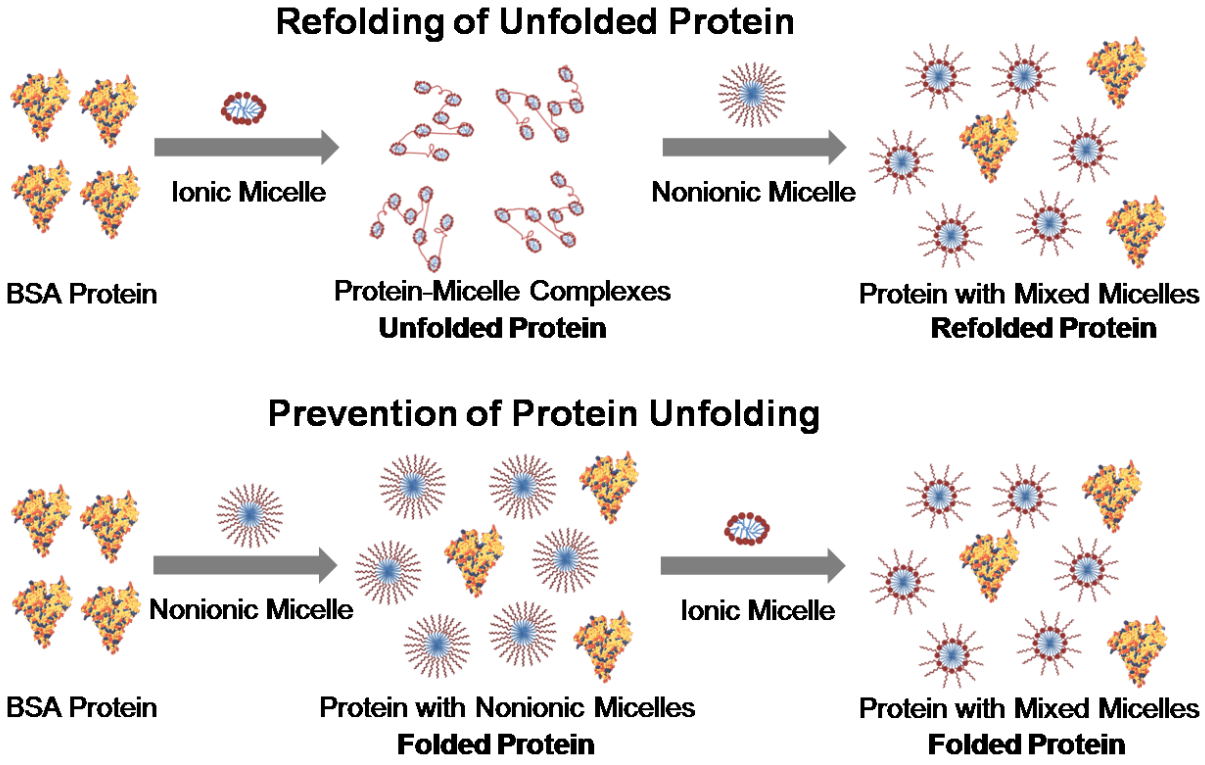

Figure 3.13. Schematic of the protein unfolding and refolding using ionic, nonionic and mixed surfactants.

It has also been observed that the interaction of protein with mixed surfactants system is independent of the order in which two surfactants (ionic and nonionic) are added [Figure (3.12)]. This in turn shows that presence of nonionic surfactant can be used to refold the unfolded protein (nonionic surfactant addition to the protein-ionic surfactant system) as well as prevent ionic surfactant-induced unfolding of the protein using nonionic surfactant (ionic surfactant addition to the protein-nonionic surfactant system). The schematic of the protein unfolding and refolding using surfactants is shown in Figure 3.13.

3.5. Conclusions

The role of different surfactants, concentration of surfactant, ionic strength and mixed surfactants on protein-surfactant interaction and their resultant structure has been studied. The ionic and nonionic surfactants show very different interactions with protein. The ionic surfactants bind to the protein by the site-specific electrostatic interaction and forming micelle-like clusters along the unfolded protein chain. On the other hand, nonionic surfactants do not interact with protein and coexist independently with unperturbed folded protein. The interaction of protein and ionic surfactant can be enhanced by increasing ionic strength and/or surfactant concentration. The ionic surfactants binding to proteins follow three concentration regions (specific binding, cooperative binding, and saturation region). Further, the nonionic-ionic mixed surfactants fold back the unfolded protein as well as prevent ionic surfactant induced protein unfolding. This behavior is explained as a result of the dominance of hydrophobic interaction of mixed surfactants over the electrostatic binding of ionic surfactant with protein. The bead-necklace structure of protein-surfactant system is characterized by the mass fractal structure and results are interpreted in terms of change in the fractal dimension, overall size of the protein-surfactant complex and number of micelles attached to the protein.

Chapter 4

Structure of Protein with Anionic Surfactant in Presence of Nanoparticles

4.1. Introduction

Multi-component systems provide synergistic effects which cannot be achieved through individual components [34,134-135,190]. Nanoparticle addition to protein-surfactant system results in such a three-component system. Nanoparticles due to their small size and large surface-to-volume ratio possess unique and distinct properties which are useful for their numerous applications [106,111,117-118,122]. Many of these applications require interaction of nanoparticles with amphiphilic molecules like proteins, surfactants and their complexes [34,110,134,191-192]. The interactions in three-component nanoparticle-protein-surfactant system are expected to be governed by two-component nanoparticle-protein, nanoparticle-surfactant and protein-surfactant interactions. In the case of protein-surfactant system, ionic surfactants bind to the protein through site-specific electrostatic binding at lower concentration and cooperative binding at higher surfactant concentrations [193]. The cooperative binding of surfactant with protein results in protein unfolding and formation of bead-necklace structure of their complexes as has been discussed in Chapter 3. Unlike protein-surfactant system, the nanoparticle-protein and nanoparticle-surfactant systems show non-cooperative interactions. These systems depending on the nature of the components (nanoparticles, protein or surfactant) and solution condition exhibit very different properties of the systems. In nanoparticle-protein systems, the protein has tendency to adsorb on the nanoparticles, which can be simply controlled by the charge of the protein or nanoparticle [38,194]. For example, in the case of lyszoyme protein, they interact strongly with oppositely charged (anionic) silica

nanoparticles, resulting in aggregation of nanoparticles mediated by protein [195-196]. On the other hand, likely charged BSA protein interacts weakly with silica nanoparticle which is believed to be through the site specific adsorption on nanoparticles [197-198]. The similar results of interaction of nanoparticles with proteins have also been observed for nanoparticles with surfactants. The micelles mimic to the proteins and their interaction and resultant structure with nanoparticles can be varied by the type (anionic, cationic or nonionic) of the surfactant used [199]. It is clear that the varying system conditions can tune the interaction among the components and result in multiple functional hybrid materials [38,41,131,200-201]. In this chapter, the interaction of protein-surfactant complexes with nanoparticles has been investigated. The nanoparticles used are Ludox HS40 silica nanoparticles in the BSA protein and SDS surfactant complexes, where all the components are anionic. The chapter reports the structure and interaction of three-component systems as understood in terms of the interactions of two components. The SANS measurements have been carried out by selectively contrast matching components wherever required to simplify the scattering from complex systems.

4.2. Experimental section

The electrostatically stabilized Ludox HS40 silica nanoparticles (catalogue no: 420816) was purchased from Sigma-Aldrich. BSA protein and SDS surfactant used were same as in chapter 3. The mixed solvents of D_2O and H_2O were used for contrast matching individual components as per the requirement. The stock solutions of each component were prepared by dissolving the required weighted amounts of components in 20 mM phosphate buffer (pH=7) in presence of 0.2 M NaCl. Small-angle neutron scattering measurements were carried out at SANS Facility at DHRUVA Reactor, BARC, Mumbai and D11 SANS facility at Institut Laue Langevin (ILL), Grenoble, France [168]. These two facilities together provide the data collection in a wide wave vector transfer (Q) range of 0.006 to 0.30 $Å^{-1}$ to probe different length scales of the system. In particular, D11 SANS facility at ILL, Grenoble provides the data to lower Q values.

All the samples were measured at 1 wt% concentration of silica nanoparticles to minimize their interparticle interactions. The silica nanoparticle interaction with protein and surfactant is studied independently by varying BSA (0 – 5 wt%) and SDS (0 – 100 mM) concentrations. The interaction of protein with surfactant is examined at a fixed concentration of BSA (1 wt%) with varying concentration of surfactant (0 – 100 mM). The three-component system is studied for fixed nanoparticle (1 wt%) and protein (1 wt%) with varying concentration of SDS (0 – 100 mM). Samples were held in standard 1 mm or 2 mm path length quartz cells during the experiments. The lower thickness of the cells is preferred for the samples having solvents with higher contents of H_2O, to lower the incoherent background. Data were corrected for background and empty cell, and normalized to absolute unit of cross section using standard procedures.

4.3. SANS analysis

The differential scattering cross section per unit volume $d\Sigma/d\Omega$ as a function of Q as measured in a SANS experiment can be expressed as [147,151]

$$\frac{d\Sigma}{d\Omega}(Q) = \phi V_p \Delta\rho^2 P(Q) S(Q) + B \qquad (4.1)$$

where ϕ is volume fraction of particles, V_p is particle volume and $\Delta\rho^2$ is scattering contrast of particles. $P(Q)$ and $S(Q)$ are the intraparticle and interparticle structure factors, respectively. B is the incoherent background. The expressions of different form factors and interparticle structure factors as used are described in chapter 2. The protein-surfactant complexes as well as nanoparticle aggregates wherever formed are characterized by structure factor of fractals (equation 2.40 and 2.41) [97,163,165].

The scattering length density and corresponding contrast match point of different constituents are given in Table 4.1. Experimental verification of contrast-match conditions of silica nanoparticles and SDS micelles is shown in Figure 4.1.

The data have been analyzed by comparing the scattering from different models to the experimental data. Throughout the data analysis corrections were also made for instrumental

smearing. The modelled scattering profiles were smeared by the appropriate resolution function to compare with the measured data. The corrections for incoherent background were taken in the model calculations as a fitting parameter. The fitted parameters in the analysis were optimized by means of nonlinear least-square fitting program [151]. The fitted data are given by the solid lines to the experimental data points.

Table 4.1. The calculated scattering length density and contrast match point of silica nanoparticles, BSA protein and different surfactants (SDS, DTAB and C12E10).

Component	Scattering length density (cm^{-2})	Contrast-match point (% vol D_2O)
Silica	3.81×10^{10}	63
BSA	2.59×10^{10}	40
SDS	0.31×10^{10}	13
DTAB	-0.42×10^{10}	2
C12E10	0.30×10^{10}	13

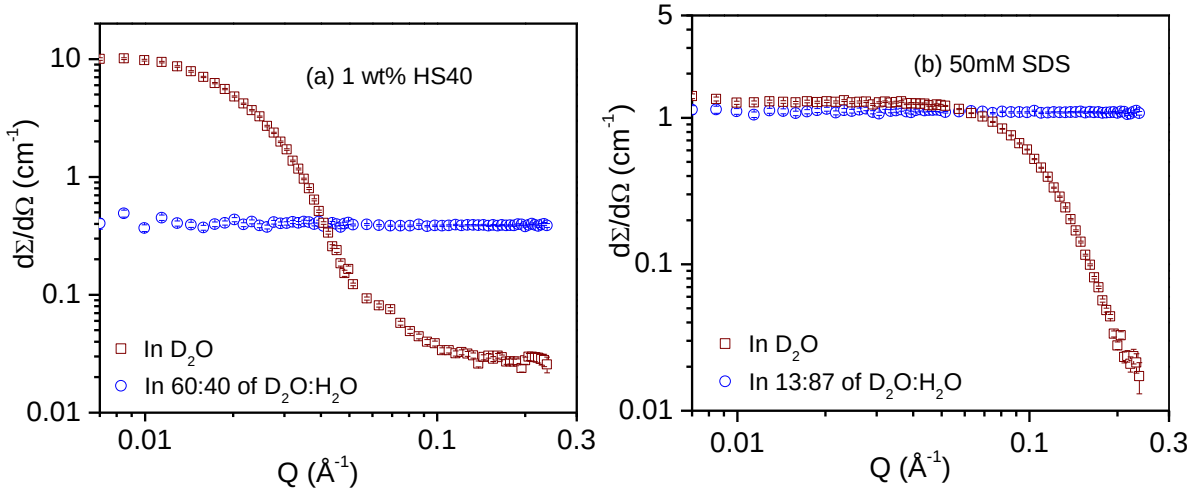

Figure 4.1. Experimental verification of contrast-matched conditions (a) silica nanoparticles and (b) SDS micelles. A flat pattern is obtained of incoherent scattering as compared to that scattering from D_2O as solvent.

4.4. Results and discussion

4.4.1. Characterization of individual components

SANS data from pure 1 wt% HS40 nanoparticle, 1 wt% BSA protein and 50 mM SDS surfactant systems are shown in Figure 4.2. The monotonically decreasing scattering profile of silica nanoparticles indicate that these systems can be treated as dilute and the scattering is determined by the intraparticle structure factor $P(Q)$ [195]. This fact was further confirmed by scaling of the data with those of the lower concentration of nanoparticles. The BSA protein and SDS surfactants are fitted by oblate ellipsoidal and prolate ellipsoidal structure as in chapter 3 and presented here for comparison with nanoparticles. The scattering profiles are significantly different for nanoparticle, protein and surfactant systems, which correspond to different sizes and contrast of the components (equation 4.1). The fitted parameters are given in Table 4.2. The HS40 nanoparticles have a mean radius of 87.1 Å with a polydispersity of 0.22 [195]. The BSA protein fits to the oblate ellipsoidal shape having semi-minor and semi-major axes of 13.6 and 42.3 Å; respectively [183]. The SDS surfactant forms prolate core-shell ellipsoidal micelles with semi-minor axis, semi-major axes and shell thickness as 16.7 Å, 29.0 Å and 5.0 Å, respectively [71]. S(Q) for charged micelles was calculated using the screened Coulomb potential between micelles under mean spherical approximation and the effective charge on the micelle is found to be around 25 e.u [156]. The structural parameters of all the above components (HS40 silica nanoparticles, BSA protein and SDS micelles) are found to be in agreement to those reported earlier [71,183,195]. The observed difference in the sizes of the components is important from the point of view of optimizing interaction of different components. The larger size difference between nanoparticle and protein enhance protein adsorption on nanoparticles, if any [202]. The C12 chain length is optimum for protein unfolding, which is used in many practical applications [65,171,188].

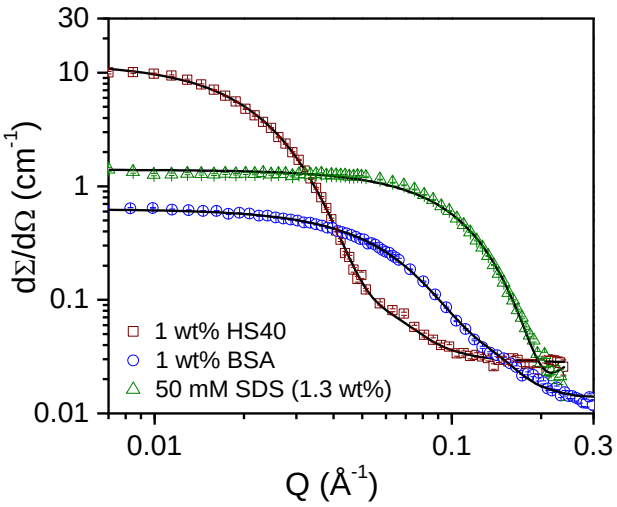

Figure 4.2. SANS data from 1 wt% HS40 silica nanoparticles, 1 wt% BSA protein and 50 mM SDS surfactant in presence of 0.2 M NaCl in D_2O. Data have been fitted by different structural models for differences in the scattering profiles of silica nanoparticles (polydisperse spheres), BSA protein (oblate ellipsoid) and SDS micelles (prolate ellipsoid).

Table 4.2. The fitted parameters of 1 wt% HS40 silica nanoparticles, 1 wt% BSA protein and 50 mM SDS surfactant in presence of 0.2 M NaCl in D_2O.

System	Shape	Structural dimensions		
Silica nanoparticles	Polydisperse spherical	Radius R_m = 87.1±1.0 Å	Polydispersity σ = 0.22±0.02	
Bovine serum albumin	Oblate ellipsoidal ($\varepsilon < 1$)	Semi-major axis R = 42.3±0.5 Å	Semi-minor axis εR = 13.6±0.2 Å	
Sodium dodecyl sulphate	Prolate core-shell ellipsoidal ($\varepsilon > 1$)	Semi-minor axis R =16.7±0.2 Å	Semi-major axis εR = 29.0±0.4 Å	Shell thickness t = 5.0 Å
		Aggregation number N = 97±4	Charge Z = 25±2 e.u.	

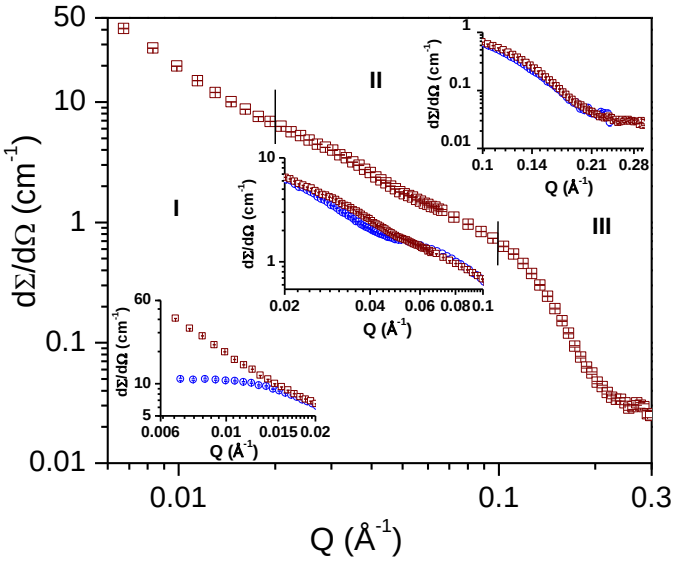

Figure 4.3. SANS data from the three-component system of 1 wt% HS40 silica nanoparticles, 1 wt% BSA protein and 50 mM SDS surfactant mixed together in presence of 0.2 M NaCl in D_2O. Insets show the differences between the measured data of the three-component system with that of the addition of data of individual components (nanoparticle, protein and surfactant) as shown in different *Q* (low, intermediate and high) regions.

Figure 4.3 shows the SANS data from a three-component complex system of 1 wt% silica nanoparticle, 1 wt% BSA protein and 50 mM SDS surfactant mixed together. These data of mixed system clearly show a very different behavior than those of the individual components (Figure 4.2). The calculated data of the addition of three individual components (nanoparticle, protein and surfactant) with the measured data of three-component system is compared in the insets. The comparison is made in three different *Q* (low, intermediate and high) regions of the data in order to understand how the mixed system behaves differently from the behavior of individual components. The scattering data of mixed system shows a buildup of scattering intensity in the low *Q* region as compared to the sum of scattering from individual components. The mixed system also show significant differences on log-log scale in the intermediate *Q* region from the sum of scattering of individual components. The measured data in the high *Q* region of the mixed system almost match to the calculated scattering of addition of individual components.

These observed differences suggest a strong interaction of components in spite of the fact that the components are similarly (anionic) charged. The properties of mixed system are expected to be determined by the different possible interactions of components with each other (e.g. nanoparticle-protein, nanoparticle-surfactant and protein-surfactant). To correlate the role of each of these two-component interactions on mixed system, they have been investigated in different combinations as discussed in the following.

4.4.2. Structure of different two-component systems

SANS data from 1 wt% HS40 with 1 wt% BSA along with corresponding pure components (1 wt% HS40 and 1 wt% BSA) in solvents D_2O and H_2O are given in Figure 4.4. It is observed that there is buildup of scattering intensity in the low Q region in the mixed system. It cannot be explained by the sum of the scattering of the two components [inset of Figure 4.4(a)] which suggests the presence of significant interaction between the components. This interaction may arise because of either adsorption of protein on nanoparticle [change in $P(Q)$] or by the increase in attractive interaction of particles [change in $S(Q)$] through the non-adsorption of protein on nanoparticles [195,203]. Only site-specific adsorption of anionic BSA on anionic nanoparticles is possible [204-206]. This kind of adsorption is expected to enhance the charge stability of nanoparticles. However, the nanoparticles are found to be aggregated in the mixed system as appeared from the observed turbidity of the system. It may be added that our system in present study is much beyond the onset of attractive interaction where the nanoparticles have achieved the complete aggregation. The aggregation in SANS data is also reflected by the linear Q dependence on log-log scale in the low Q region. In the case of fractal aggregates of particles, SANS data show a linear Q dependence whose higher and lower cut offs are decided by the building block (particle) size and overall size of the aggregates, respectively

[163,195]. In the high *Q* region, the data of mixed system match to that of addition of nanoparticle and BSA, suggesting nanoparticle aggregates coexist with the free proteins. In the case of SANS experiments using solvent H_2O, the scattering from protein is minimized [Figure 4.4(b)]. The scattering data of 1 wt% HS40 with 1 wt% BSA in H_2O still shows similar features to that of in D_2O. The scattering is dominated by fractal aggregates of nanoparticles. The nanoparticle aggregation can be explained as a result of depletion force of non-adsorption of protein on the nanoparticles [25,207-208].

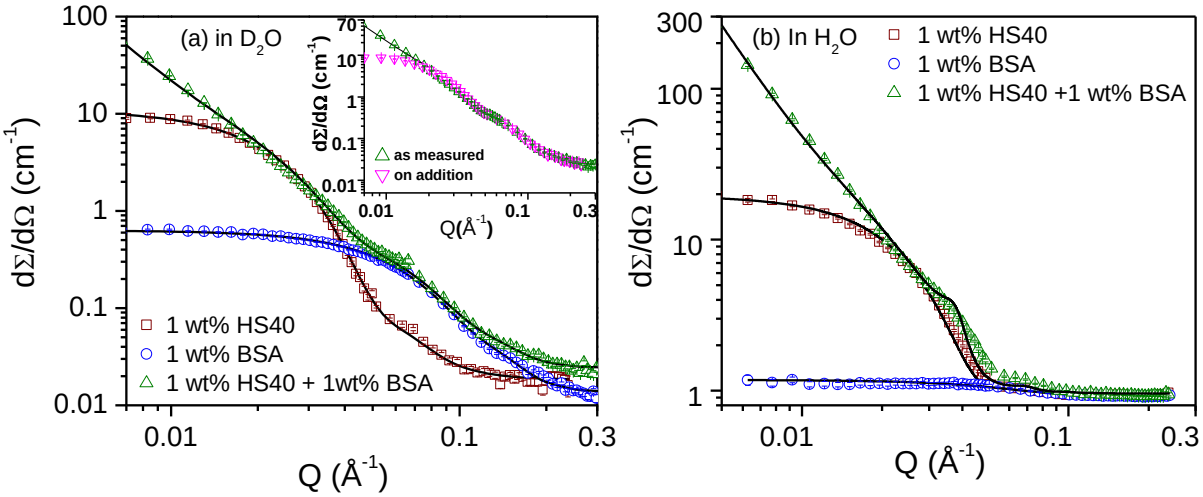

Figure 4.4. SANS data from 1 wt% HS40 silica nanoparticles with 1 wt% BSA protein is compared with individual components (1 wt% HS40 and 1 wt% BSA) in presence of 0.2 M NaCl (a) in D_2O and (b) in H_2O. Inset of (a) shows the comparison of experimentally measured data of 1 wt% HS40 + 1 wt% BSA to the calculated sum of individual component data. Scattering data of 1 wt% HS40 + 1wt% BSA are fitted by the model of coexistence of nanoparticle aggregates with BSA protein in the system.

SANS data of 1 wt% HS40 silica nanoparticle with varying concentration of BSA protein (0.5 – 5 wt%) are shown in Figure 4.5. All the data in the low *Q* region have similar features irrespective of protein concentration whereas differ in the high *Q* region. The linear behavior of SANS data on log-log scale in low *Q* region suggests fractal aggregates of nanoparticle even formed at 0.5 wt% of protein concentration [163,209]. The buildup of scattering in the higher *Q*

region with increase in protein concentration is because of scattering from protein is enhanced. The data are fitted with the coexistence of nanoparticle aggregates with BSA protein in the system. The fitting parameters of HS40 nanoparticles with varying protein concentration are given in Table 4.3. There is no layer coating of BSA found around the nanoparticles. This is confirmed by the fitting of S(Q), where the higher Q cut-off correspond to the size of nanoparticle (not to the size of sum of nanoparticle and protein). The fitted parameters of BSA protein in the mixed systems are found to be same as that of the pure systems. The value of fractal dimension (~ 2.5) suggests that the nanoparticle aggregation is governed by the process of diffusion limited aggregation (DLA) [210]. There is no lower cut-off observed in the SANS data indicating the overall size of aggregates could be much larger than 1000 Å (~ $2\pi/Q_{min}$) that can be measured from the present Q range of the data.

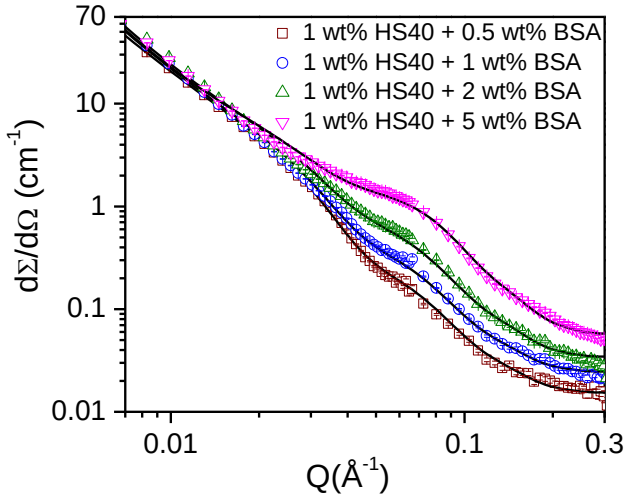

Figure 4.5. SANS data from 1 wt% HS40 silica nanoparticles with varying concentration of BSA protein in presence of 0.2 M NaCl in D_2O. Data are fitted by the model of coexistence of nanoparticle aggregates with BSA protein in the system. The buildup of scattering in the higher Q region arises from the free (non-adsorbing) protein in the system.

Table 4.3. The fitted fractal dimension of aggregation of silica nanoparticles (1 wt% HS40) with varying concentration of BSA protein in presence of 0.2 M NaCl in D_2O. The mixed system (nanoparticle-protein) consists of aggregates of nanoparticles coexisting with individual proteins. The building block size of the fractal aggregates is same in all the cases that of the size of nanoparticle (87.1 Å), whereas the extent of aggregates has been taken a value larger than $2\pi/Q_{min}$ (~ 1000 Å) because of absence of lower Q cut-off.

[BSA] (wt%)	0.5	1	2	5
Fractal dimension (D)	2.40±0.15	2.53±0.18	2.55±0.18	2.56±0.18

SANS data of 1 wt% HS40 nanoparticles in presence of 50 mM SDS surfactant along with individual components are shown in Figure 4.6. The data for mixed system are found to be dominated by scattering from larger-sized HS40 nanoparticles in the low Q region whereas by smaller-sized SDS micelles in the high Q region (see Table 4.2). The inset of the figure shows that scattering from the mixed (nanoparticle + micelle) system can be represented almost by adding of scatterings from individual components of nanoparticles and micelles. This indicates the absence of any kind of physical interaction between components, which has also been supported in Figure 4.7 by either contrast matching nanoparticles or surfactant micelles to the solvent. The overlapping of data of mixed (1 wt% HS40 + 50mM SDS) system with that one of the pure components (other is contrast-matched), confirms there exists no physical interaction between the components. These results are unlike the case of nanoparticle and protein system. In spite of the fact that both the micelles and proteins are anionic, their interaction with anionic nanoparticles has been observed to be significantly different. The non-significant observation of depletion interaction for the micelles may be due to their much smaller size and having a higher charge on them than the protein [25,207]. These two contributions are expected to suppress the excluded volume effect for micelles with nanoparticles and hence their depletion interaction [25,211]. The data have been fitted by considering HS40 nanoparticles and SDS micelles coexist

independently. Further, the independent coexisting of two components has been examined over a wide range (5 – 100 mM) of surfactant concentration [Figure 4.8(a)]. In all the cases data are

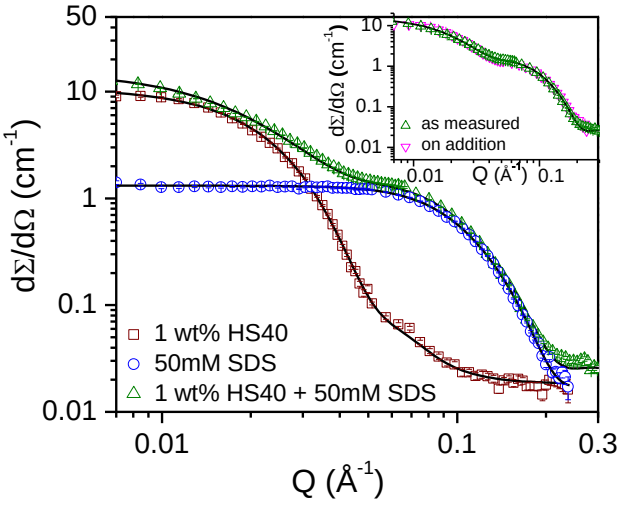

Figure 4.6. SANS data from 1 wt% HS40 silica nanoparticles with 50 mM SDS micelles compared with individual components (1 wt% HS40 and 50 mM SDS) in presence of 0.2 M NaCl in D_2O. Inset shows the comparison of as measured data (1 wt% HS40 + 50 mM SDS) with that of the addition of individual components. Data of 1 wt% HS40 + 50 mM SDS are fitted by sum of model scattering from individual components of nanoparticles and micelles.

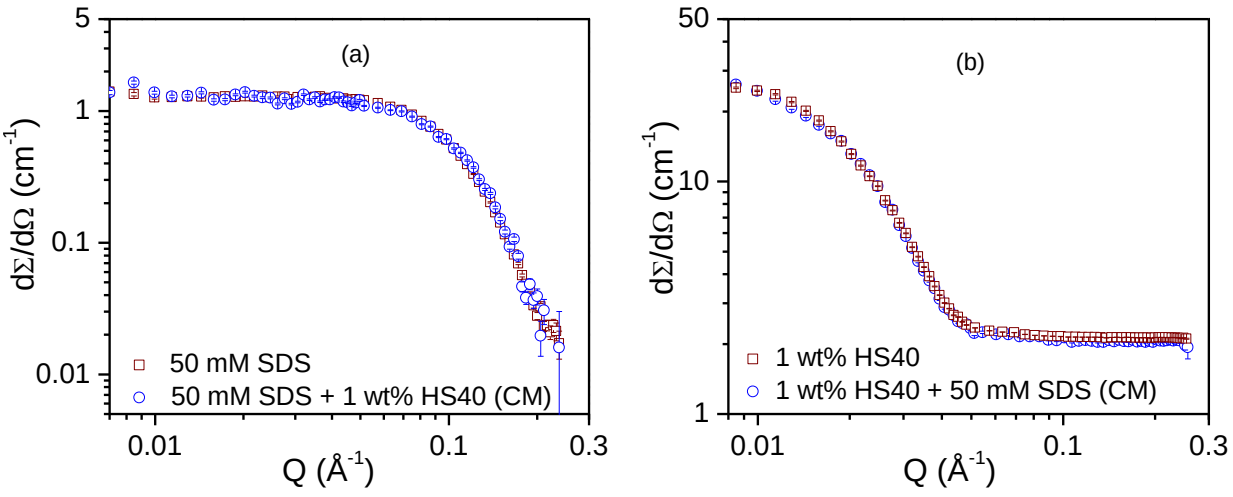

Figure 4.7. SANS data of 1 wt% HS40 with 50 mM SDS (a) nanoparticles are contrast-matched along with data from pure surfactant (SDS) system and (b) micelles are contrast-matched along with data from pure nanoparticle (HS40) system.

fitted by the scattering which is sum of the individual components. The fitted parameters are given in Table 4.4. It is also interesting to note that the micellar structure did not show any observable changes without or with silica nanoparticles. The micellar structure is also found to be almost similar over the measured concentration range of 0 to 100 mM. The increase in aggregation number of surfactant micelles is known to depend on salt to surfactant molar ratio [13,73,212]. The aggregation numbers in Table 4.4 are from the combined effect of (i) surfactant concentration effect which increases with the surfactant concentration and (ii) salt to surfactant molar ratio effect which decreases with the surfactant concentration for a fixed salt concentration. The SANS data for pure SDS in salt solutions are given in Figure 4.8(b). The fact they look almost parallel to each other, suggests they correspond to similar structure (aggregation number) of micelles.

Table 4.4. The fitted structural parameters of (5 - 100 mM) SDS micelles coexisting with (1 wt%) HS40 nanoparticles in presence of 0.2 M NaCl in D_2O. Data are fitted for prolate core-shell ellipsoidal shape of SDS micelles residing independently in solution. The similar parameters are also obtained for pure SDS micellar solution without HS40 nanoparticles.

[SDS] mM	Semi-major axis (Å)	Semi-minor axis (Å)	Shell thickness (Å)	Charge Z (e.u.)	Aggregation number (N)
5	27.2±0.9	16.7±0.3	5.0	-	90±6
10	27.5±0.6	16.7±0.3	5.0	-	91±5
25	28.3±0.5	16.7±0.2	5.0	-	94±4
50	29.0±0.4	16.7±0.2	5.0	25±2	97±4
100	29.1±0.4	16.7±0.2	5.0	25±2	97±4

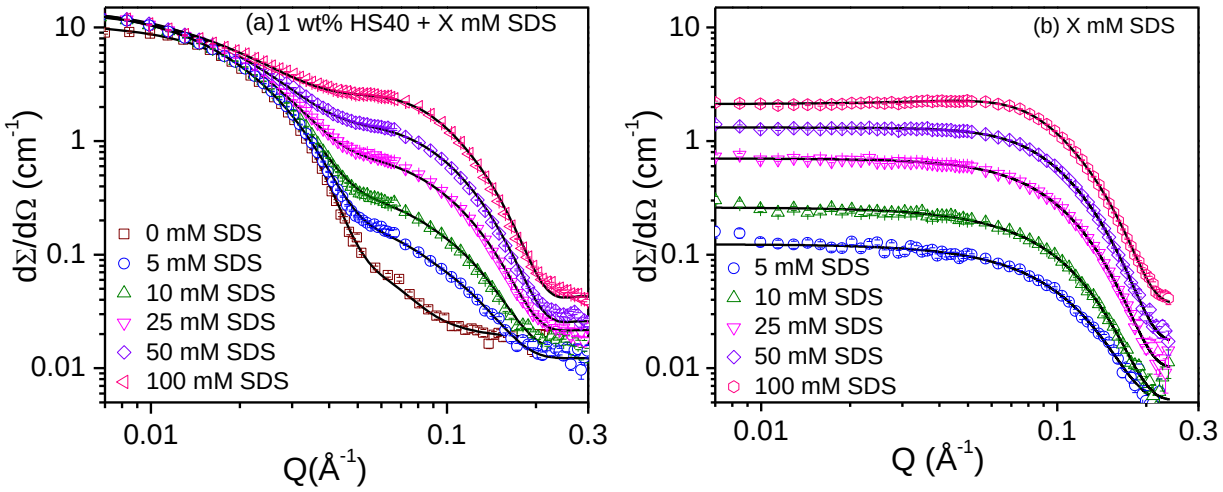

Figure 4.8. SANS data from (a) 1 wt% HS40 silica nanoparticles with varying concentration of SDS surfactant (b) different concentrations of individual SDS surfactants in presence of 0.2 M NaCl in D_2O. Data of mixed system are fitted by sum of model scattering from individual components of nanoparticles and micelles.

Unlike the interaction of SDS surfactants with nanoparticle, the surfactants are known to be strongly interacting with the protein as discussed in chapter 3. The surfactants show concentration dependent interaction with the protein. SANS data of 1 wt% BSA with varying surfactant concentrations from 0 to 100 mM SDS are shown in Figure 4.9. The surfactants bind to protein through site specific binding at low concentration, cooperative binding at intermediate concentration region and show saturation at still higher concentrations. The protein unfolds in cooperative binding region resulting in formation of the bead-necklace structure characterized by mass fractal as discussed in chapter 3. The fitted parameters are shown in Table 4.5. The free micelles are also found to be coexisting with protein-surfactant complex at higher surfactant concentration beyond 50 mM. The value of free micelles at 100 mM is determined about 35%.

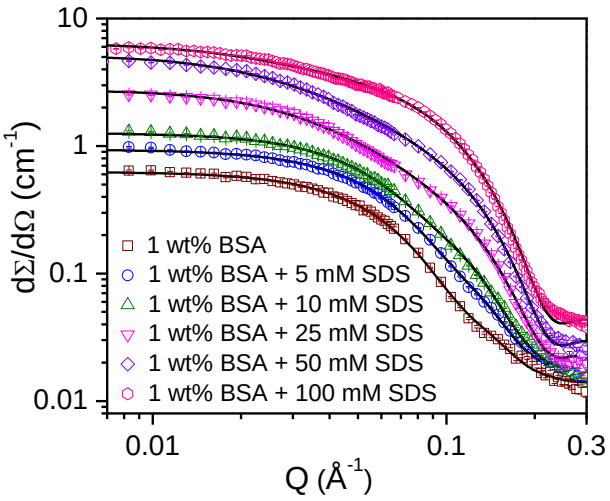

Figure 4.9. SANS data from 1 wt% BSA protein with varying concentration of SDS surfactant in presence of 0.2 M NaCl in D_2O. Data in lower surfactant concentration (0 – 10 mM) are fitted by the expanded protein structure whereas by fractal structure of micelle-like clusters randomly distributed along the unfolded protein chain for higher concentrations of surfactant (25 – 100 mM). The free micelles are also found to be coexisting with protein-surfactant fractal structure in the case of 100 mM SDS.

Table 4.5. The fitted parameters of SANS analysis of protein-surfactant complex for 1 wt% BSA with varying concentration of SDS surfactant in presence of 0.2 M NaCl in D_2O.

(i) Oblate ellipsoidal shape of the protein macromolecule for lower concentrations of surfactant (0 – 10 mM).

System	Semi-minor axis (Å)	Semi-major axis (Å)
1 wt% BSA	13.6±0.2	42.3±0.5
1 wt% BSA+5 mM SDS	13.6±0.2	44.3±0.5
1 wt% BSA+10 mM SDS	13.6±0.2	50.3±0.6

(ii) Fractal structure of micelle-like clusters randomly distributed along the unfolded protein chain for higher concentrations of surfactant (25 - 100 mM).

System	Fractal dimension D	Correlation length ξ (Å)	Micelle radius r (Å)	Number of micelles n	Aggregation number N
1 wt% BSA+25mM SDS	2.18±0.10	25.2±1.0	18.6	3	55
1 wt% BSA+50mM SDS	1.62±0.08	39.8±2.5	18.6	6	50
1 wt% BSA+100mM SDS	1.35±0.08	49.5±4.0	18.6	8	50

4.4.3. Structure of resultant three-component system

The interaction of the three-component system nanoparticle-protein-surfactant has been looked into based on the above discussed interactions of two component systems (nanoparticle-protein and protein-surfactant). SANS data of the three-component system of 1 wt% HS40 mixed with 1 wt% BSA and 50 mM SDS is compared to two-component systems of 1 wt% HS40 with 1 wt% BSA and 1 wt% BSA with 50 mM SDS in Figure 4.10. It is interesting to note that the scattering behavior of the three-component system is the cumulative effect of two-component systems corresponding to protein-surfactant interaction as seen in the higher *Q* region and nanoparticle-protein in the lower *Q* region. This structure of protein-surfactant complex is found showing similar features with and without the presence of nanoparticles. The low *Q* scattering behavior of the three-component system is similar to that observed in the two-component system of nanoparticle-protein but unlike the case of the nanoparticle-surfactant system. This suggests that the protein-surfactant complex behaves more like that of protein but unlike surfactant in interaction with nanoparticles. This is possible as the surface charge density of surfactant micelles is expected to decrease on the formation of the

protein-surfactant complex, which makes the complex to behave more like that of nanoparticle-protein (depletion induced nanoparticle aggregation) than nanoparticle-surfactant (non-aggregation of particles). The effect of varying surfactant concentration on the nanoparticle-protein-surfactant system is shown in Figure 4.11. It is observed that the data in the low *Q* region corresponding to the nanoparticle aggregation remain more or less same with the increase in surfactant concentration (0 – 100 mM). There are systematic changes in the higher *Q* region, which are similar to that of the protein-surfactant system. This suggests that irrespective of absence or presence of nanoparticles, the interaction of protein and surfactant is maintained over a wide concentration range of surfactant. The schematic of the resultant structures formed in the three component nanoparticle-protein-surfactant system are given in Figure 4.12.

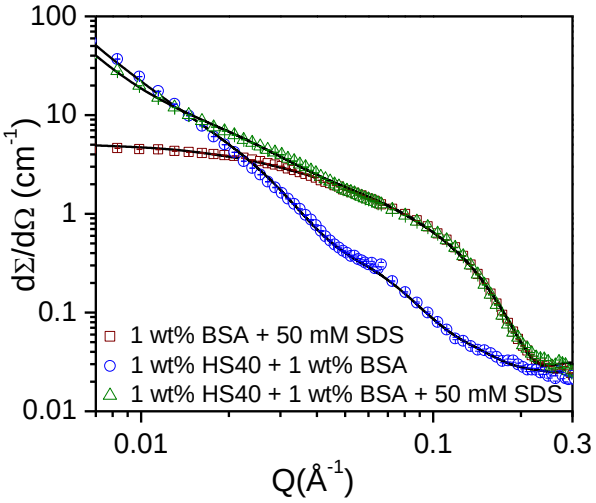

Figure 4.10. SANS data from three-component system of 1 wt% HS40 silica nanoparticles mixed with 1 wt% BSA protein and 50 mM SDS surfactant and compared along with two-component systems of 1 wt% HS40 + 1 wt% BSA and 1 wt% BSA + 50 mM SDS in presence of 0.2 M NaCl in D_2O. Data of three-component system are fitted by the sum of the scattering contributions of protein-surfactant complexes and nanoparticle aggregates as induced by proteins.

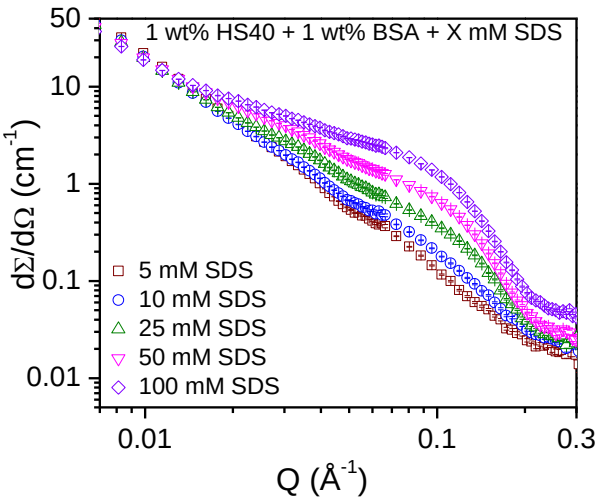

Figure 4.11. SANS data from 1 wt% HS40 silica nanoparticles mixed with 1 wt% BSA protein and varying concentration of SDS surfactant (5 – 100 mM) in presence of 0.2 M NaCl in D_2O.

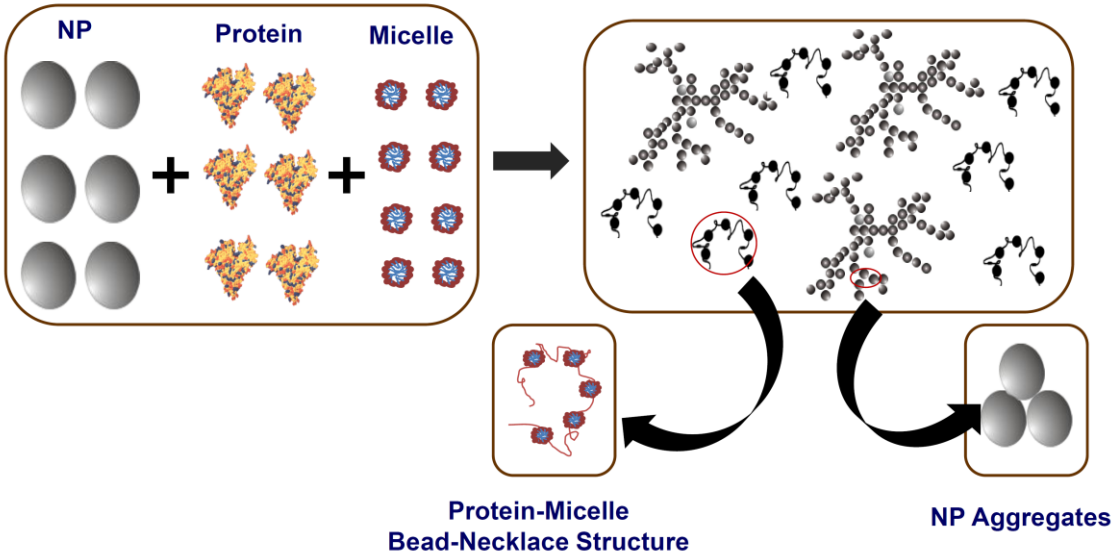

Figure 4.12. Schematic of the structures formed in the three-component nanoparticle-protein-surfactant system.

4.4.4. Role of individual component in three-component system

The combined effect of nanoparticle-protein and protein-surfactant systems in their three-component system (nanoparticle-protein-surfactant) is further examined by the contrast variation SANS experiments. In the case, when nanoparticles are contrast matched,

the SANS data of nanoparticle-protein-surfactant system have similar features to that of protein-surfactant system [Figure 4.13(a)]. This confirms that protein-surfactant interaction is

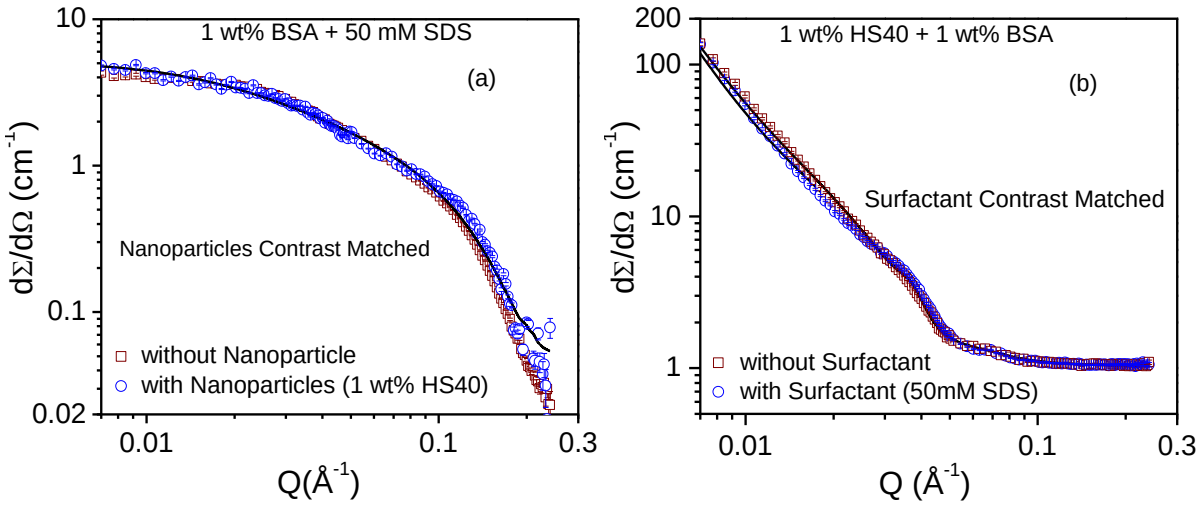

Figure 4.13. SANS data (a) 1 wt% HS40 + 1 wt% BSA + 50 mM SDS having silica nanoparticles contrast matched are compared with 1 wt% BSA + 50 mM SDS and (b) 1 wt% HS40 + 1 wt% BSA + 50 mM SDS having surfactant contrast matched are compared with 1 wt% HS40 + 1 wt% BSA in presence of 0.2 M NaCl. Data of 1 wt% BSA + 50 mM SDS without and with nanoparticles (contrast matched) are fitted by bead-necklace structure of BSA-SDS complex whereas data of 1 wt% HS40 + 1 wt% BSA without and with surfactant (contrast matched) are fitted by coexistence of nanoparticle aggregates with BSA protein in the system.

Table 4.6. Fitted parameters of fractal structure of protein-surfactant complex (1 wt% BSA + 50 mM SDS) without and with nanoparticles. The analysis for protein-surfactant system with nanoparticles (1 wt% HS40) is from when the nanoparticles are contrast matched. Both the systems have been studied in presence of 0.2 M NaCl.

System	Fractal dimension D	Correlation length ξ (Å)	Micelle radius r (Å)	Number of micelles n	Aggregation number N
Without nanoparticle	1.62±0.08	39.8±2.5	18.6	6	50
With nanoparticles	1.45±0.11	49.7±4.0	18.6	7	43

maintained in the absence as well as presence of nanoparticles. However, there are significant differences observed with nanoparticles, which is an indication of their favoring of the protein unfolding. The fitted parameters of protein-surfactant complexes without and with nanoparticles are given in Table 4.6. The fractal dimension decreases with increase in the correlation length of the protein-surfactant complex in the presence of nanoparticles, which suggests to nanoparticle enhanced unfolding of protein with surfactant. The enhanced unfolding of protein is also consistent with the increase in number of micelles attached to polypeptide chain along with decrease in aggregation number of micelles. On the other hand, when the surfactant is contrast matched, the data of nanoparticle-protein-surfactant system look similar to that of the nanoparticle-protein system [Figure 4.13(b)]. These results confirm that nanoparticle aggregates that of nanoparticle-protein system also exist in nanoparticle-protein-surfactant system. The observed changes in the data without and with surfactant are expected to be due to enhanced aggregation of nanoparticles (low Q region) with the unfolding of protein in the presence of surfactant [135]. The fractal dimension of nanoparticle aggregation is found to be increased from 2.5 to 2.7 in presence of both protein and surfactant as compared to protein alone. This increase in fractal dimension also supports the enhancement in the aggregation of nanoparticles with protein in presence of surfactant. Both the protein and surfactant are non-adsorbing to the nanoparticles. The resultant depletion depends on the excluded volume, which is enhanced for protein in the presence of surfactant as the overall size of protein-surfactant complex is larger than the protein alone.

4.5. Conclusions

The silica nanoparticle effect in BSA protein and SDS surfactant system has been studied. It is found that there exists a strong interaction of components although the components

are similarly (anionic) charged. The properties of nanoparticle interaction with protein-surfactant system are determined by the different possible interactions of components with each other (e.g. nanoparticle-protein, nanoparticle-surfactant and protein-surfactant). Surfactants interact cooperatively with the protein to form bead-necklace structure comprising micelle-like clusters of the surfactant along the unfolded protein chain. In nanoparticle-protein system, the nanoparticle aggregates are formed through the depletion force of non-adsorbing protein to the nanoparticles. On the other hand, no physical interaction is observed between the components for nanoparticle-surfactant system. The resultant structural behavior of the three-component system is explained via synergetic effect of two-component nanoparticle-protein and protein-surfactant interactions. The non-adsorption of protein-surfactant complex on nanoparticles result in depletion induced nanoparticle aggregation (similar to nanoparticle-protein system) coexisting with the protein-surfactant complexes. Both the bead-necklace structure of protein-surfactant complexes and nanoparticle aggregates are characterized by the mass fractals. The protein unfolding as well as nanoparticle aggregation is found to be enhanced in the three-component system as compared to the corresponding two-component systems.

Chapter 5

Structure of Cationic versus Anionic Surfactants with Protein in Presence of Nanoparticles

5.1. Introduction

Tuning of the structure and interaction of nanoparticles with macromolecules can generate new properties for various applications. The properties of such complexes can be varied by various parameters which include charge on individual component, pH, ionic strength etc [200,209,213-214]. In all these, electrostatic interaction among the components plays an important role in controlling and easy tuning the structure and interaction of such complexes [194,200,209,215]. For example, the interaction of silica nanoparticle with oppositely charged lysozyme protein and DTAB surfactant provides strong adsorption of protein/micelle on nanoparticles, which in turn leads to protein/micelle mediated fractal aggregation of nanoparticles [185,196,209,216]. The nanoparticle aggregates coexist with unaggregated nanoparticles at the low protein/micelle concentrations whereas with free protein/micelle at high concentrations. In the case of similarly charged BSA protein and SDS surfactant, they show non-adsorption on silica nanoparticles which can lead to depletion force between silica nanoparticles (chapter 4). This depletion interaction can result in nanoparticle aggregation similar to that of oppositely charged nanoparticle-protein/surfactant systems [185,216]. On the other hand, the interactions in protein-surfactant complexes are significantly different and cooperative binding of surfactant with protein leads to the unfolding of protein through

micelle-like clusters attached along the unfolded polypeptide chain (chapters 3). The cooperative binding is predominantly hydrophobic so both the anionic (SDS) and cationic (DTAB) surfactants undergo quite similar binding with anionic (BSA) protein [193,217-218]. There is interest to know how the different two-component interactions control the structure and interaction in three-component systems. It is also interesting to examine the role of a particular component in modifying the interaction of other two components.

Chapter 4 discussed the results of the three-component system of silica nanoparticle, BSA protein and SDS surfactant, where all the three components are anionic [219-220]. It has been found that the interaction of individual two-components (nanoparticle-protein, nanoparticle-surfactant and protein-surfactant) governs the properties of three-component system. The nanoparticle-protein system shows depletion force induced nanoparticle aggregates coexisting with free protein. Both the components remain independently in nanoparticle-surfactant system, whereas the surfactant interacts cooperatively with protein leading to micelle-like cluster of the surfactants formed along the unfolded chain of protein. The structure of the three-component (nanoparticle-protein-surfactant) system is found to be determined by the synergetic effect of nanoparticle-protein and protein-surfactant interactions. The protein-surfactant complex controls the structure of three-component system leading to nanoparticle aggregates similar to that of nanoparticle-protein system. The nanoparticle aggregation in three-component system as compared to nanoparticle-protein as well as unfolding of protein in three-component system as compared to protein-surfactant is enhanced. In the present chapter, a three-component system where the anionic surfactant SDS has been replaced by cationic surfactant DTAB is examined. This kind of change in three-component system

is expected to significantly modify the nanoparticle-surfactant and protein-surfactant interactions [86,218,221]. The structure and interaction in these two-component systems and their role in three-component system have been studied by SANS.

5.2. Experimental section

Electrostatically stabilized colloidal suspension of ludox HS40 silica nanoparticles, BSA protein and DTAB surfactant were used same as in chapters 3 and chapter 4. The stock solutions of each component were prepared by dissolving the required weighted amounts of components in 20 mM phosphate buffer (pH=7) in presence of 0.2 M NaCl. The silica nanoparticle interaction with protein and surfactant is studied at fixed concentrations of nanoparticle (1 wt%), protein (1 wt%) and surfactant (50 mM). Small-angle neutron scattering experiments were performed using SANS facilities at the Dhruva reactor, Bhabha Atomic Research Centre, Mumbai [146] and SANS-I facility, Swiss Spallation Neutron Source SINQ, Paul Scherrer Institut, Switzerland [167]. The data were covered over a wave vector transfer (Q) range of 0.006 to 0.30 $Å^{-1}$. Samples were held in standard 1 mm or 2 mm path length quartz cells during the experiments. Data were corrected for background, empty cell and normalized to absolute unit of cross section.

5.3. SANS analysis

The differential scattering cross section per unit volume $d\Sigma/d\Omega$ for a system of monodisperse particles is given as [147,151,182]

$$\frac{d\Sigma}{d\Omega}(Q) = nV_p^2\Delta\rho^2 P(Q)S(Q) + B \qquad (5.1)$$

where n is number density of particles, V_p is particle volume and $\Delta\rho^2$ is scattering contrast of particles. $P(Q)$ and $S(Q)$ are the intraparticle and interparticle structure factors, respectively.

B is the incoherent background. The expressions for standard P(*Q*) and S(*Q*) as used are described in chapter 2.

In the case of interaction leading to the adsorption of micelles or proteins on nanoparticles, $d\Sigma/d\Omega$ for such core-shell structure can be expressed as [184]

$$\frac{d\Sigma}{d\Omega}(Q) = n\left[(\rho_c - \rho_{shell})V_1\left\{\frac{3j_1(Qr_1)}{Qr_1}\right\} + (\rho_{shell} - \rho_s)V_2\left\{\frac{3j_1(Qr_2)}{Qr_2}\right\}\right]^2 S(Q) + B \qquad (5.2)$$

where ρ_c, ρ_{shell} and ρ_s are, respectively, the scattering length densities of the core, shell and solvent. The dimensions r_1, r_2, V_1 and V_2 are the inner radius, outer radius, volume of core and volume of core along with shell, respectively.

The strong interaction between oppositely charged micelles or proteins with nanoparticles is known to result in aggregation of nanoparticles. The aggregates are characterized by a S(*Q*) of mass fractal as given in equation 2.40 (chapter 2). The mass fractal structure is also used for the bead-necklace model of protein-surfactant complex as given in equation 3.2 (chapter 3).

The data have been analyzed by comparing the scattering from the combination of different models to the experimental data. The corrections for instrumental smearing were made throughout the data analysis [222]. The fitted parameters in the analysis were optimized by means of nonlinear least-square fitting program [151]. The fitted data are represented by the solid lines to the experimental data points.

5.4. Results and discussion

5.4.1. Characterization of cationic versus anionic surfactants

The characterization of pure 1 wt% HS40 silica nanoparticles, 1 wt% BSA protein and 50 mM SDS surfactant is discussed in chapter 4 (Figure 4.2). The comparison of SANS scattering profiles of cationic DTAB and anionic SDS surfactant is shown in Figure 5.1. The scattering profiles are fitted with *P*(*Q*) of prolate ellipsoidal core-shell structure and *S*(*Q*) of screened Coulomb potential between micelles under the rescaled mean spherical approximation

(chapter 4) [158]. The fitted parameters of both the surfactants for comparison are given in Table 5.1. The structure of DTAB micelles is found to be similar to SDS micelle except they are oppositely charged. The use of DTAB versus SDS surfactants is to understand the role of electrostatic interactions in governing their interactions with protein and nanoparticles, and in turn resultant structure of three-component nanoparticle-protein-surfactant system.

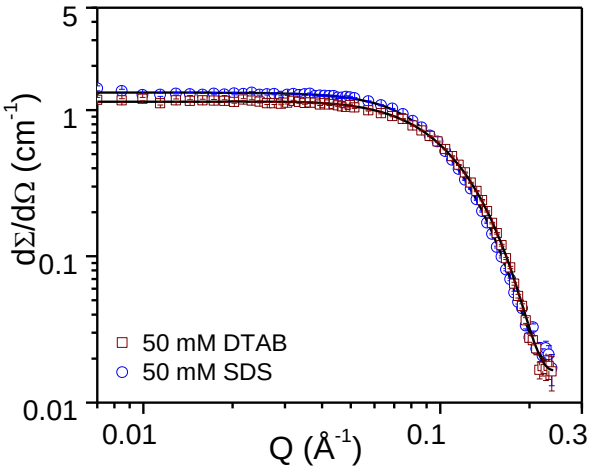

Figure 5.1. SANS data of 50 mM DTAB surfactant compared with 50 mM SDS surfactants at pH=7 and in the presence of 0.2 M NaCl in D_2O.

Table 5.1. The structural parameters of 50 mM DTAB and 50 mM SDS surfactant solutions at pH=7 and in the presence of 0.2 M NaCl in D_2O.

System	Shape	Structural dimensions		
dodecyl trimethylammonium bromide (DTAB)	Prolate core-shell ellipsoidal ($\varepsilon > 1$)	Semi-minor axis R =16.7±0.2 Å	Semi-major axis εR = 21.0±0.4 Å	Shell thickness t = 5.8 Å
		Aggregation number N = 70±4	Charge Z = +21±2 e.u.	
Sodium dodecyl sulfate (SDS)	Prolate core-shell ellipsoidal ($\varepsilon > 1$)	Semi-minor axis R =16.7±0.2 Å	Semi-major axis εR = 29.0±0.4 Å	Shell thickness t = 5.0 Å
		Aggregation number N = 97±4	Charge Z = -25±2 e.u.	

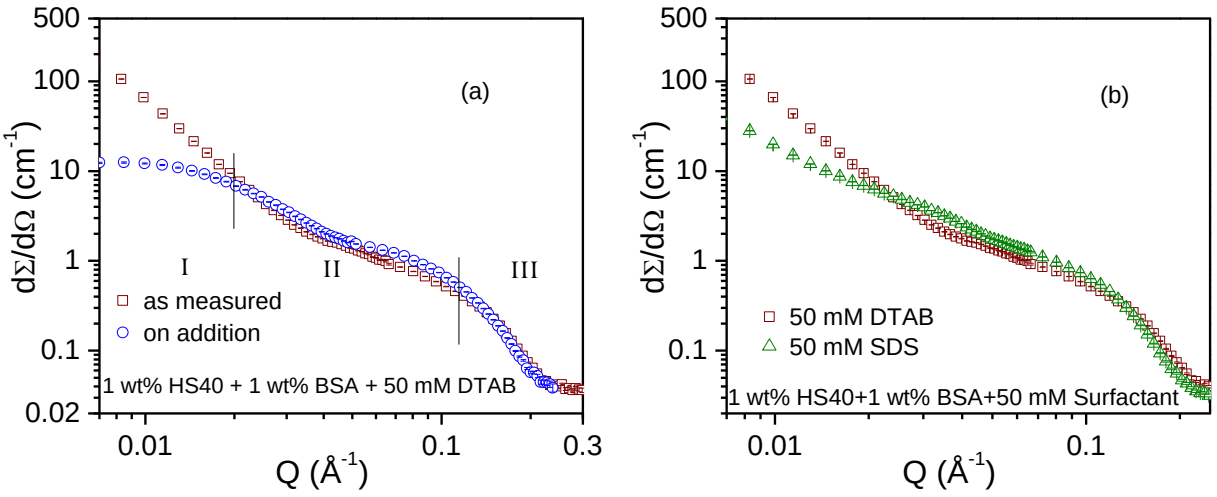

Figure 5.2. SANS data of 1 wt% HS40 silica nanoparticles + 1 wt% BSA protein + 50 mM DTAB surfactant are compared with (a) sum of scattering from individual components (1 wt% HS40 silica nanoparticles, 1 wt% BSA protein and 50 mM DTAB surfactant) and (b) 1 wt% HS40 silica nanoparticles + 1 wt% BSA protein + 50 mM SDS surfactant at pH=7 and in the presence of 0.2 M NaCl in D_2O.

SANS scattering profile of three-component system of anionic silica nanoparticle-anionic BSA protein-cationic DTAB surfactant is shown in Figure 5.2. The SANS data as measured are also compared with simple addition of scattering from the three individual components. The scattering profile of three-component system is significantly different from the sum of scattering of individual components indicating the strong interaction and/or structural evolution in three-component system as compared to individual components. The scattering profile over the whole *Q* range can be divided into three regions. The scattering from region III in high *Q* range almost overlap with the sum of scattering from individual components. There are significant differences of scattering from the two profiles in intermediate *Q* range (region II) and dramatic differences in the low *Q* range (region I). In particular, the strong build up of scattering and linearity on log-log scale in the low *Q* range (region I) indicates the formation of large size fractal aggregates in solution [196,216]. The SANS data of silica nanoparticle-BSA protein-

DTAB surfactant are also found to be significantly different than those of silica nanoparticle-BSA protein-SDS surfactant system [Figure 5.2 (b)]. The significant differences in scattering profiles indicate that the cationic versus anionic surfactant play important role in tuning the properties of three-component system. The differences in microstructure of nanoparticle-protein-surfactant system for DTAB vs SDS surfactants are expected from the difference in the interaction of nanoparticle-surfactant and protein-surfactant complexes.

5.4.2. Structure of different two-component systems

Amongst different possible two-component systems (nanoparticle-protein, nanoparticle-surfactant and protein-surfactant) in the three-component system of silica nanoparticle-BSA protein-DTAB surfactant, the nanoparticle-protein system has been discussed in chapter 4. The non adsorption of BSA protein on nanoparticles result in depletion force induced nanoparticle aggregation coexisting with the BSA protein [216,219]. The nanoparticle aggregates are characterized by mass fractal with fractal dimension D=2.55 indicating diffusion limited aggregation like fractal morphology. SANS data of 1 wt% HS40 silica nanoparticles + 50 mM DTAB surfactant is shown in Figure 5.3. The scattering profile of nanoparticle-surfactant system is also compared with the sum of scattering of individual components. The scattering in intermediate to high *Q* range is dominated by DTAB micelles, whereas the linearity in scattering profile in low *Q* range arises from the fractals of nanoparticle aggregates similar to nanoparticle-protein system [163,221]. In the case of nanoparticle-DTAB surfactant system, the electrostatic interaction mediated by oppositely charged surfactant micelles between nanoparticles is expected to govern the nanoparticle aggregation. SANS data of nanoparticle-surfactant system is also compared with nanoparticle-protein

(1 wt% HS40 + 1 wt% BSA) system in Figure 5.4(a). The difference in structures of nanoparticle aggregates in silica nanoparticle-DTAB surfactant system and silica nanoparticle-BSA protein system is also evident from the difference in scattering in low *Q* range. The nanoparticle aggregates in silica nanoparticle-DTAB surfactant system have higher slope in the low *Q* region than the case of silica nanoparticle-BSA protein system. The higher slope (fractal dimension) means higher packing fraction of nanoparticles in these aggregates, which is expected because of the strong electrostatic binding mediated by surfactant micelles among the nanoparticles [200,209]. The difference in scattering in the intermediate to high *Q* range is from the different scattering contrast and volume fractions of proteins and micelles in solution. The SANS data of silica nanoparticles with DTAB and SDS are compared in Figure 5.4(b). It had been found for SDS (very different than DTAB) that it is non-adsorbing as well non-depleting even up to very high concentration (chapter 4) [219]. It seems that nanoparticle-surfactant interaction is the most important one in deciding the differences in the structures of three-component system having surfactant as DTAB or SDS. Further, the role of surfactant micelles in the nanoparticle-surfactant aggregates has been examined by contrast matching the individual components systematically.

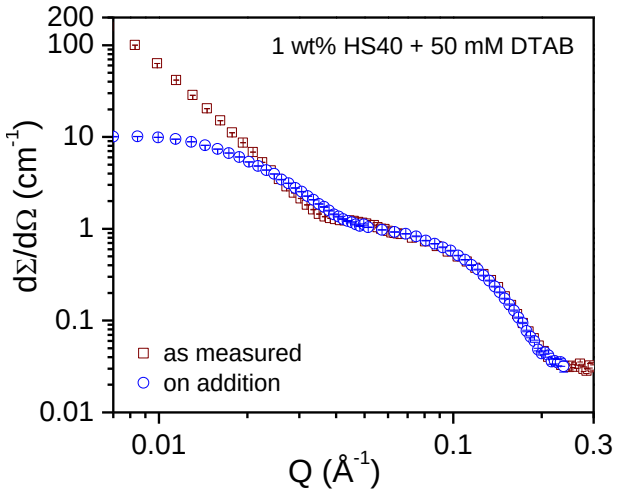

Figure 5.3. SANS data of 1 wt% HS40 silica nanoparticles + 50mM DTAB surfactant compared with the sum of scattering of individual components at pH=7 and in presence of 0.2 M NaCl in D_2O.

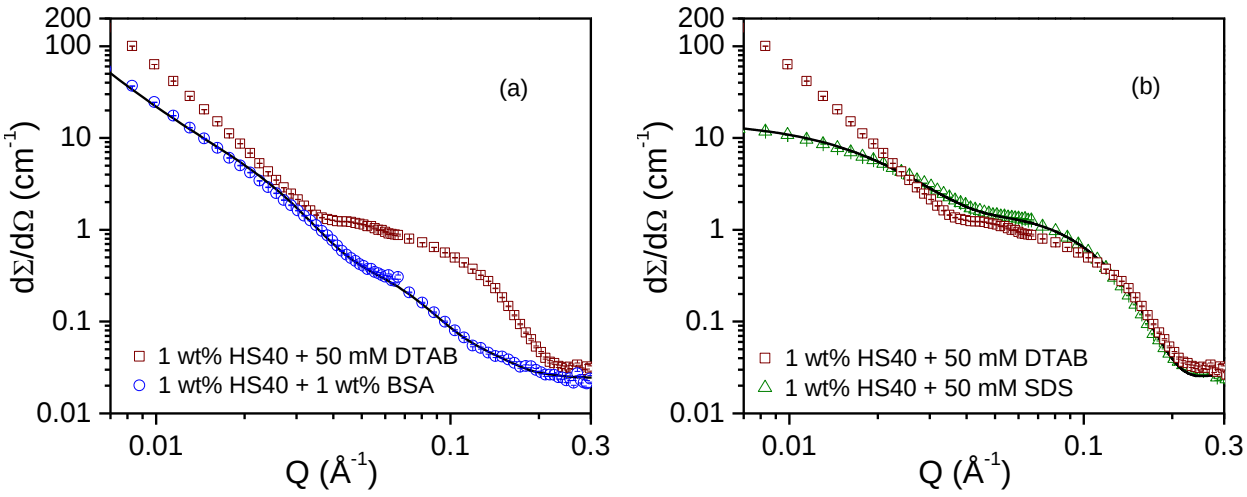

Figure 5.4. SANS data of 1 wt% HS40 silica nanoparticles + 50mM DTAB surfactant compared with (a) 1 wt% HS40 silica nanoparticles + 1 wt% BSA protein and (b) 1 wt% HS40 silica nanoparticles + 50 mM SDS surfactant at pH=7 and 0.2 M NaCl in D_2O.

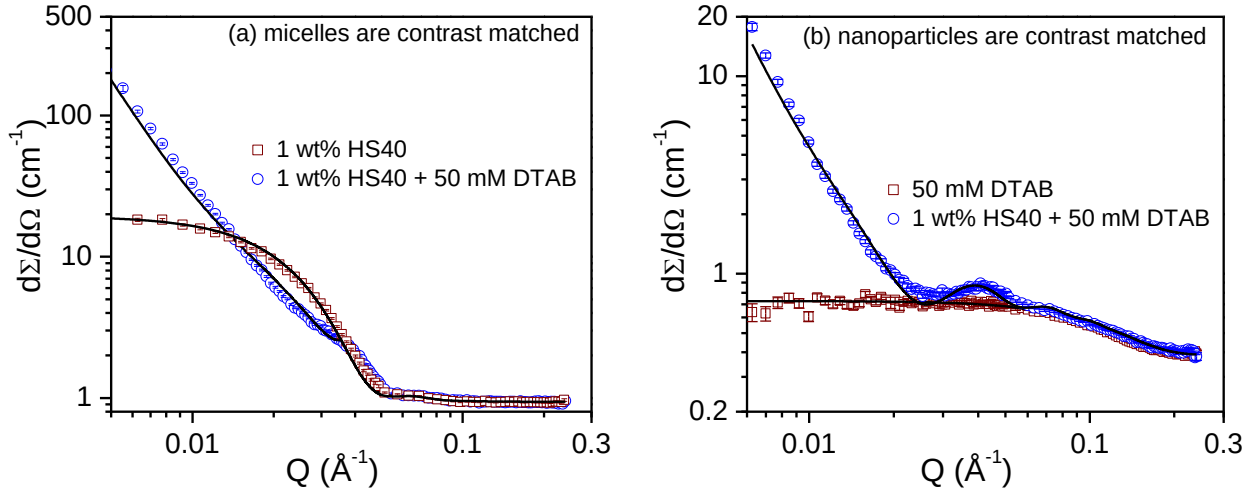

Figure 5.5. SANS data of 1 wt% HS40 silica nanoparticles + 50 mM DTAB surfactant with (a) micelles are contrast matched and compared with 1 wt% HS40 silica nanoparticles and (b) nanoparticles are contrast matched and compared with 50 mM DTAB surfactant at pH=7 and 0.2 M NaCl.

Figure 5.5 shows SANS data of HS40 nanoparticle-DTAB surfactant system with (a) surfactant is contrast matched and (b) nanoparticles are contrast matched. The scattering of nanoparticle-surfactant system as compared to only nanoparticle system under surfactant contrast matched condition (Table 4.1) has very different behavior [Figure 5.5(a)]. There are clearly two

distinct features observed in the low and intermediate *Q* regions to that of nanoparticle-surfactant system. This shows the formation of new structure of nanoparticles in presence of surfactant. The large scattering with linear dependence in low *Q* region confirms the new structure as nanoparticle aggregates which are characterized by a mass fractal. The fractal dimension for nanoparticle-surfactant system (D=2.72) is found to be significantly larger than diffusion limited aggregation of nanoparticles in presence of protein [210,223]. The lower scattering for nanoparticle-surfactant system than the only nanoparticle system in the intermediate *Q* range indicates that the building block size in the aggregate structure is significantly higher that of the nanoparticle size, which possibly arises because of the surfactant micelles mediating the nanoparticles aggregates. This point is made clear in [Figure 5.5(b)] when the nanoparticles in nanoparticle-surfactant system are contrast matched (60 vol% D_2O in mixed D_2O/H_2O solvent). The scattering from surfactant micelles in nanoparticle-surfactant system is observed to be very different than pure surfactant solution. Similar to Figure 5.5 (a), there are again two distinct features observed in Figure 5.5(b) at the low and intermediate *Q* regions of nanoparticle-surfactant system. The large scattering in the low *Q* region followed by a hump in the intermediate *Q* value arise from the aggregates of core-shell structure of surfactant micelles surrounding the non-visible nanoparticles [185,224]. The data are fitted using mass fractal distribution of shells of micelles [$d\Sigma/d\Omega(Q) \sim P(Q)S(Q)$] with corresponding $S(Q)$ and $P(Q)$. The fractal dimension of 2.72 of nanoparticle aggregates is found to be similar to when the micelles are contrast-matched and the thickness of micelles adsorbed around the nanoparticles has a value about the size (diameter 41 Å) of the micelles. Interestingly, the building block size (radius 107 Å) of the fractal aggregates is significantly less than that of the sum of the nanoparticle size (radius 87 Å) and micelle size (diameter 41 Å). This is an indication that the nanoparticles are bridged by the single micelle to favor the attractive electrostatic interaction

between them for their aggregation. The number of adsorbed DTAB micelles per nanoparticle (*N*) is found to be 50. The maximum number of micelles that can adsorb at the nanoparticle surface is given by $N_{max} = \frac{4\pi(R+r)^2}{\pi r^2}$, where *r* and *R* are radii of micelle and nanoparticles, respectively. This results N_{max}= 110 for *R*=87 Å and *r*= 20.5 Å. The large differenece between *N* and N_{max} arises because of *N* is decided by the competition of nanoparticle-micelle attraction and micelle-micelle repulsion.

It has been observed that nanoparticles undergo aggregation in presence of both the protein and surfactant despite of their very different nature of interaction with the nanoparticles. Therefore, the interaction of protein and surfactant is going to play important role when both the components are present in the nanoparticle solution. The surfactant molecules are known to be strongly interacting with the protein through electrostatic as well as hydrophobic interactions [179,193,218]. Both the cationic DTAB and anionic SDS surfactants unfold the BSA protein resulting in formation of bead-necklace structure of these complexes (chapter 3). SANS data of 1 wt% BSA protein with 50 mM DTAB surfactant is compared with 1 wt% BSA protein with 50 mM SDS as shown in Figure 5.6. The scattering profiles from these systems show quite similar features. The data are fitted using structure factor of mass fractal *S*(*Q*) and form factor *P*(*Q*) of spherical micelles as discussed in chapter 3 and fitted parameters are given in Table 5.2. The size of micelle-like clusters is found to be smaller (16.8 Å for BSA-DTAB as compared to 18.6 Å for BSA-SDS) and overall size of complex larger (61.8 Å for BSA-DTAB as compared to 39.8 Å for BSA-SDS) in case of DTAB than SDS [219]. This supports to the fact that cationic DTAB micelles are relatively more effective in protein unfolding than anionic SDS micelles [177-178,193]. However, it is expected because of different overall charge on the

protein-surfactant complex for the two surfactants (DTAB and SDS) will lead to their different interaction with nanoparticles.

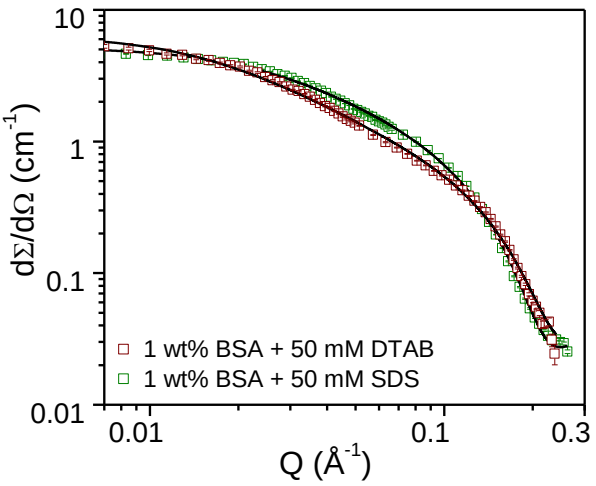

Figure 5.6. SANS data of 1 wt% BSA protein + 50 mM DTAB surfactant compared with 1 wt% BSA protein + 50 mM SDS surfactant at pH=7 and in the presence of 0.2 M NaCl in D_2O.

Table 5.2. The fitting parameters of two-component systems at pH=7 and in the presence of 0.2 M NaCl in D_2O.

(a) Nanoparticle-protein system characterized by depletion interaction induced fractal aggregates of nanoparticles (from chapter 4).

System	Particle radius R (Å)	Building block radius r (Å)	Fractal dimension D
1 wt% HS40 + 1 wt% BSA	87.1±1.0	87.1±1.0	2.55±0.20

(b) Nanoparticle-surfactant system characterized by surfactant micelle mediated fractal aggregates of nanoparticles.

System	Particle radius R (Å)	Shell Thickness t (Å)	Building block radius r (Å)	Fractal dimension D	Adsorbed micelles per particle (N)
1 wt% HS40 + 50 mM DTAB	87.1±1.0	41.0±0.5	107.0	2.72±0.20	50

(c) Protein-surfactant system characterized by fractal structure of micelle-like clusters formed along the unfolded protein chain.

System	Micelle radius r (Å)	Correlation length ξ (Å)	Fractal dimension D	Number of micelles n	Aggregation number N
1 wt% BSA + 50 mM DTAB	16.8±0.2	61.8±4.0	1.59±0.10	10	35

5.4.3. Structure of resultant three-component system

The structure of three-component nanoparticle-protein-surfactant system is now examined in Figure 5.7 in terms of behavior of two-component systems. In the three-component nanoparticle-protein-surfactant system, the possible two-component interactions which could play role in deciding the interaction and resultant structure are (i) nanoparticle-protein, (ii) nanoparticle-surfactant and (iii) protein-surfactant. However, the SANS data in Figure 5.7 show that the present system is represented by the features of silica nanoparticle-DTAB surfactant in low *Q* region and BSA protein-DTAB surfactant in high *Q* region. This indicates that the silica nanoparticle-BSA protein-DTAB surfactant consists of protein-surfactant complexes coexisting with surfactant or protein-surfactant complex mediated aggregates of nanoparticles. These results are clearly different from the SANS data of silica nanoparticle-BSA protein-SDS surfactant (inset of Figure 5.7), which are represented by silica nanoparticle-BSA protein in low *Q* region and BSA protein-SDS surfactant in high *Q* region [219]. In this case, the system consists of protein-surfactant complexes coexisting with their depletion induced aggregates of nanoparticles. In both the cases with cationic DTAB and anionic SDS surfactants, the interaction of these protein-surfactant complexes with nanoparticles governs the resultant structure of nanoparticle-protein-surfactant systems. This is perhaps expected amongst the three components (nanoparticle, protein and surfactant), protein and surfactant are much smaller in sizes, which therefore have higher possibility of interaction because of their higher mobility in

solution, and hence control the resultant structure. The schematic of microstructures formed in three-component system with cationic DTAB surfactants is shown in Figure 5.8.

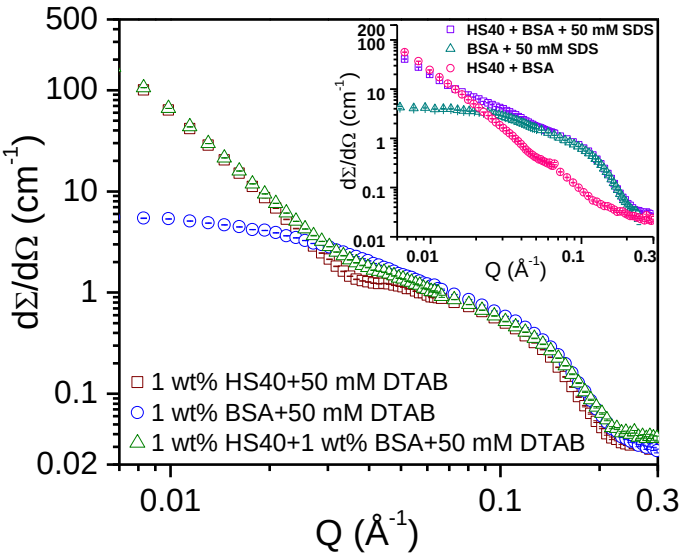

Figure 5.7. SANS data of 1 wt% HS40 silica nanoparticles + 1 wt% BSA protein + 50 mM DTAB surfactant along with scattering data of 1 wt% HS40 silica nanoparticles + 50 mM DTAB surfactant and 1 wt% BSA protein + 50 mM DTAB surfactant at pH=7 and in the presence of 0.2 M NaCl in D_2O. Inset shows the scattering profile of 1 wt% HS40 silica nanoparticles + 1 wt% BSA protein + 50 mM SDS surfactant along with 1 wt% HS40 silica nanoparticles + 1 wt% BSA protein and 1 wt% BSA protein + 50 mM SDS surfactant at pH=7 and 0.2 M NaCl in D_2O.

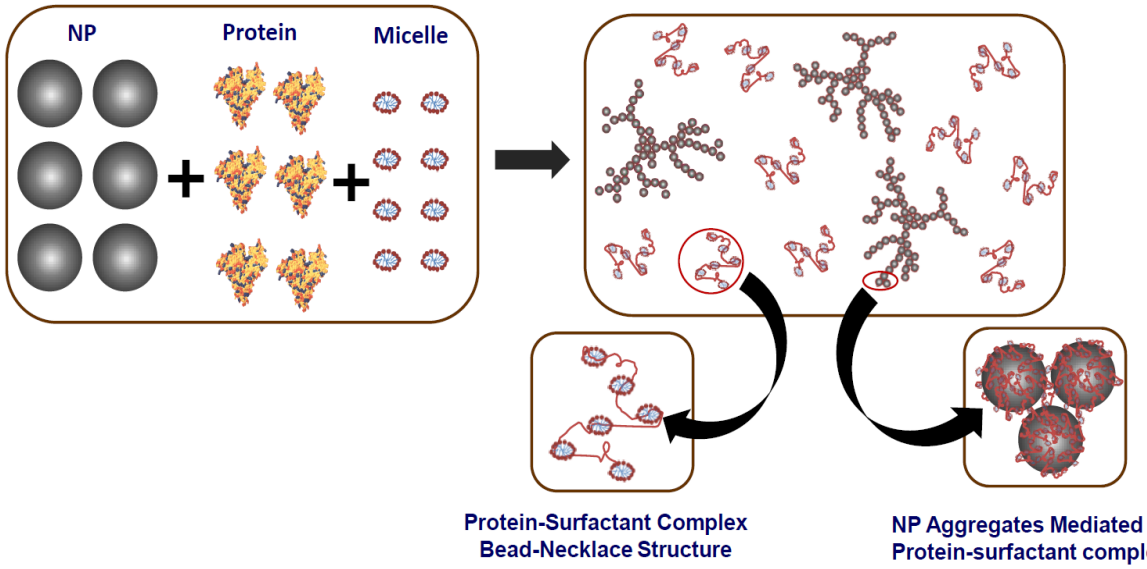

Figure 5.8. Schematic of structures formed in three-component system of anionic silica nanoparticles, anionic BSA protein and cationic DTAB surfactant.

5.4.4. Role of Individual component in three-component system

The details of three-component system have been further investigated by selectively contrast matching different components as shown in Figure 5.9 and 5.10. SANS data of nanoparticle-protein-surfactant (1 wt% HS40 silica nanoparticle + 1 wt% BSA protein + 50 mM DTAB surfactant) system is compared with two-component nanoparticle-protein (1 wt% HS40 silica nanoparticle + 1 wt% BSA protein) and nanoparticle-surfactant (1 wt% HS40 silica nanoparticle + 50 mM DTAB surfactant) systems under the surfactant contrast matched condition are shown in Figure 5.9. All these systems show fractal aggregates of nanoparticles as has been discussed. However, there are significant differences in the features of data of these systems, which may correspond to different structures formed through different mechanisms of nanoparticle aggregation [200,209]. The lower scattering intensity in the case of nanoparticle-protein-surfactant and nanoparticle-surfactant systems than nanoparticle-protein system corresponds to higher building block size, which is an indication of nanoparticle aggregation mediated by surfactant micelles or protein-surfactant complex for nanoparticle-protein-surfactant system similar to that of surfactant micelles for nanoparticle-surfactant system.[21] In the case of nanoparticle aggregation is also mediated by only surfactant micelles for nanoparticle-protein-surfactant system, the fraction of free micelles available for protein will decrease, which in turn should show significantly different scattering than that of protein-surfactant system in absence of nanoparticles. However, it has been observed that the scattering of nanoparticle-protein-surfactant system almost match to the protein-surfactant system in the intermediate to high Q region (> 0.05 $Å^{-1}$) (Figure 5.7). The rearrangement of micelles in protein-surfactant complex could be the reason for almost same value of building block size of nanoparticle-protein-surfactant and nanoparticle-surfactant aggregates. The fitted parameters are given in Table 5.3. The fractal dimension of nanoparticle-protein-surfactant aggregates is interestingly found to be quite similar to that of

nanoparticle-protein aggregates but less than that of nanoparticle-surfactant aggregates. This is possible as bridging of nanoparticles through protein-surfactant complex because of decrease in the charge on the micelle may not be as effective as with the surfactant micelles alone [185,200,209].

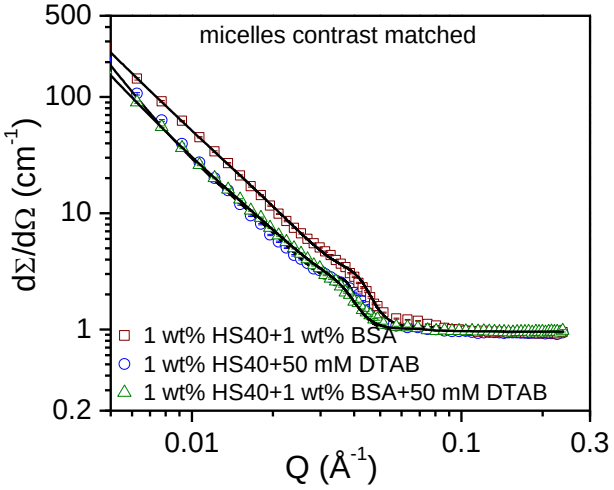

Figure 5.9. SANS data of 1 wt% HS40 silica nanoparticles + 1 wt% BSA protein + 50 mM DTAB surfactant compared with 1 wt% HS40 silica nanoparticles + 1 wt% BSA protein and 1 wt% HS40 silica nanoparticles + 50 mM DTAB surfactant at pH=7 and in 0.2 M NaCl with micelles contrast matched.

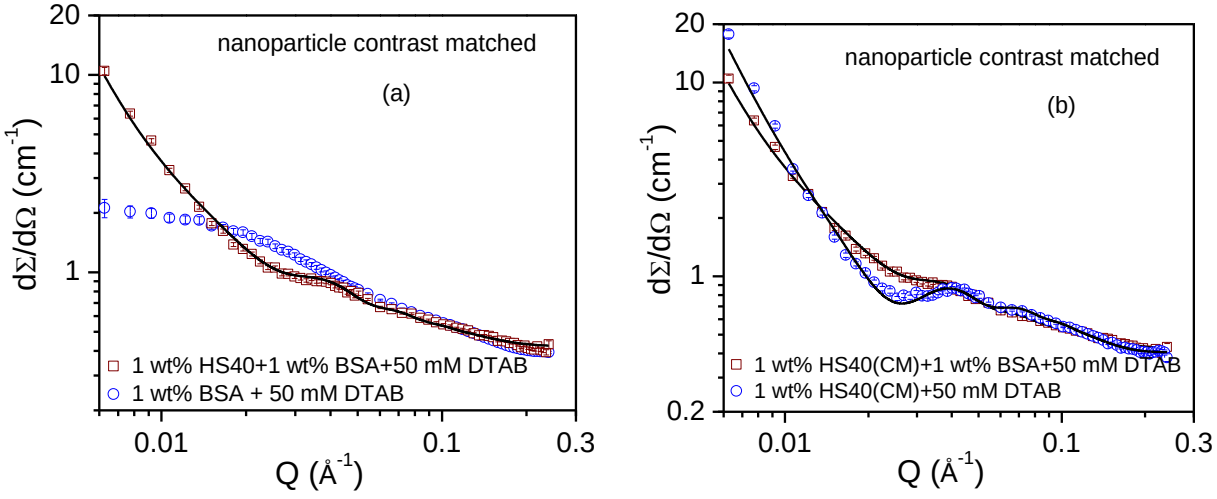

Figure 5.10. SANS data of 1 wt% HS40 silica nanoparticles + 1 wt% BSA protein + 50 mM DTAB surfactant compared with (a) 1 wt% BSA protein + 50 mM DTAB surfactant (b) 1 wt% HS40 silica nanoparticles + 50 mM DTAB surfactant at pH=7 and in the presence of 0.2 M NaCl with nanoparticles contrast matched.

Table 5.3. The fitting parameters of three-component nanoparticle-protein-surfactant system at pH=7 and in the presence of 0.2 M NaCl.

(a) Surfactant is contrast matched.

System	Particle radius R (Å)	Building block radius r (Å)	Fractal dimension D
1 wt% HS40 + 1 wt% BSA + 50 mM DTAB	87.1±1.0	108.0	2.55±0.20
1 wt% HS40 + 50 mM DTAB	87.1±1.0	107.0	2.72±0.20

(b) Nanoparticle is contrast matched.

System	Micelle radius r (Å)	Fractal dimension D	Correlation length ξ (Å)	Number of micelles n	Aggregation number N
BSA-DTAB	16.8±0.2	1.59±0.10	61.8±4.0	9	35
HS40-BSA-DTAB	16.8±0.2	1.30±0.12	70.0±4.4	11	29

Figure 5.10 shows the SANS data of three-component nanoparticle-protein-surfactant system compared with two-component protein-surfactant and nanoparticle-surfactant, where nanoparticles are contrast matched. The scattering profile of nanoparticle-protein-surfactant system clearly shows very different profile than protein-surfactant system [Figure 5.10(a)]. The build up of scattering in low *Q* region is due to the shell formation of micelle-like clusters of protein-surfactant complex around non-visible nanoparticles in these aggregates. The scattering profile of nanoparticle-protein-surfactant system is also compared with nanoparticle-surfactant system in the Figure 5.10(b). The scattering profile of nanoparticle-protein-surfactant system is considerably different than that of nanoparticle-surfactant system. The data are different in low *Q*

region because of differences in the fractal dimension of two systems (Table 5.3), whereas the differences in intermediate *Q* range arise because of different structures (micelles versus protein-surfactant complex) coexisting with nanoparticle aggregates. The data are fitted with a shell of protein-surfactant complex around the non-visible nanoparticles in their aggregates coexisting with free protein-surfactant complexes. The shell thickness is found to be around 43 Å. The similar values of shell thicknesses for nanoparticle-protein-surfactant and nanoparticle-surfactant systems [Table 5.2(b)] is in accordance with the rearrangement of micelles in adsorbed protein-surfactant complex on nanoparticles in leading to their (nanoparticle) aggregation. Moreover, the unfolding of protein in free protein-surfactant complex in the three-component system is found to be enhanced by the presence of nanoparticles. This in turn suggests that the structure in nanoparticle-protein-surfactant complexes is determined by the modified interactions of individual two components.

5.5. Conclusions

The structure and interaction of addition of anionic Ludox HS40 silica nanoparticle in anionic BSA protein and cationic DTAB surfactant have been studied. The results are compared with the similar complexes for DTAB surfactant interchanged by anionic SDS surfactant. The structures in these three-component systems are interpreted in terms of the interactions of individual two components. The non-adsorption of BSA leads to depletion force induced aggregation of nanoparticles. The micelle mediated aggregation of nanoparticles is also observed in the oppositely charged nanoparticle-surfactant system. These nanoparticle aggregates are characterized by mass fractals. In the case of protein-surfactant system, the surfactant molecules form micelle-like clusters adsorbed along the unfolded protein chain. The nanoparticle-surfactant (mediated through protein-surfactant complex) and protein-surfactant interactions for DTAB

govern the resultant structure of nanoparticle-protein-surfactant complexes. The fractal dimension of nanoparticle-protein-surfactant aggregates is found to be quite similar to that of nanoparticle-protein aggregates but less than that of nanoparticle-surfactant aggregates. There is rearrangement of micelles in adsorbed protein-surfactant complex on nanoparticles in leading to their (nanoparticle) aggregation in nanoparticle-protein-surfactant system. On the other hand, the unfolding of protein in free protein-surfactant complex is found to be significantly enhanced with respect to without the presence of nanoparticles. The role of DTAB than SDS is found to be interestingly different, where nanoparticle-protein (mediated through protein-surfactant complex) and protein-surfactant for SDS decide their resultant structure. It is thus shown that the structure and interaction of three-component nanoparticle-protein-surfactant systems can simply be modified by the change in the charge state of the surfactant.

Chapter 6

Structure of Nonionic-Ionic Mixed Surfactants with Protein in Presence of Nanoparticles

6.1. Introduction

The structure and interaction in there-component nanoparticle-protein-surfactant system depend on the characteristics of individual components and solution conditions [219,225]. The delicate balance of multiple interactions governs the phase behavior of these three-component systems. For example, cationic versus anionic surfactants form different microstructures in the three-component nanoparticle-protein-surfactant system, which are governed by different two-component interactions as studied in chapter 4 and 5. The charge nature of surfactant (cationic versus anionic) plays important role in governing the interaction between different components [219,225]. The use of nonionic surfactants in absence of any charge can significantly modify the interactions and resultant structures of these systems. The differences in the case of nonionic surfactants are expected from the different interaction of nonionic surfactants with proteins and nanoparticles [81,86,226]. In the case of protein-surfactant system, nonionic surfactants do not show any interaction with the protein and coexist individually in their mixed system (chapter 3) [193]. For nanoparticle-surfactant system, nonionic surfactants have tendency to adsorb on the nanoparticles and form a micellar corona around the nanoparticle surface [81,226]. These micelles become non-adsorbing to nanoparticles in salt solution as counterions are preferred over surfactants to adsorb on nanoparticles [227-228]. In the case of micelle adsorption on nanoparticles, the nanoparticle-surfactant system becomes more stable due to steric repulsion between adsorbed micelles [81,185,226]. However, the system tends to be unstable for non-adsorbing micelles because of the depletion interaction induced by

them between the nanoparticles. Thus, the microstructures in three-component nanoparticle-protein-surfactant system are expected to be different than the case with ionic surfactants. In this chapter, the structure and interaction of silica nanoparticles in BSA protein and nonionic C12E10 surfactant system have been studied. The there-component systems with mixed nonionic and ionic are also studied and compared with the results of individual surfactants. The mixed surfactants provide interesting systems where the protein-surfactant and nanoparticle-surfactant can be tuned between those of ionic and nonionic behavior of the surfactants.

6.2. Experimental section

Electrostatically stabilized colloidal suspension of ludox HS40 silica nanoparticles, BSA protein and surfactants (nonionic C12E10, anionic SDS and cationic DTAB) were used same as in chapters 3 and 4. The stock solutions of each component were prepared by dissolving the required weighted amounts of components in 20 mM phosphate buffer (pH=7) in presence of 0.2 M NaCl. The silica nanoparticle interaction with protein and nonionic surfactant was studied at fixed concentrations of nanoparticle (1 wt%), protein (1 wt%) and surfactant (50 mM). The concentration of mixed surfactants was also kept constant (50 mM) having components (nonionic and ionic) mixed in equal molar ratio. Samples were measured for three contrast conditions of solvent (100 %D_2O, 60% D_20 and 13% D_2O). Small-angle neutron scattering experiments were performed using SANS facilities at the Dhruva reactor, Bhabha Atomic Research Centre, Mumbai [146] and SANS-I facility, Swiss Spallation Neutron Source SINQ, Paul Scherrer Institut, Switzerland [167]. The data were covered over a wave vector transfer (Q) range of 0.006 to 0.30 $Å^{-1}$. Samples were held in standard 1 mm or 2 mm path length quartz cells during the experiments. Data were corrected for background, empty cell and normalized to absolute unit of cross section.

6.3. SANS analysis

The differential scattering cross section per unit volume $d\Sigma/d\Omega$ for a system of monodisperse particles is given as [147,182]

$$\frac{d\Sigma}{d\Omega}(Q) = nV_p^2\Delta\rho^2 P(Q)S(Q) + B \tag{6.1}$$

where n is number density of particles, V_p is particle volume and $\Delta\rho^2$ is scattering contrast of particles. $P(Q)$ and $S(Q)$ are the intraparticle and interparticle structure factors, respectively. B is the incoherent background. The expressions for standard $P(Q)$ and $S(Q)$ as used are described in chapter 2.

In the case of interaction leading to the adsorption of micelles or proteins on nanoparticles, $d\Sigma/d\Omega$ for such core-shell structure is calculated as given in equation 5.2. The aggregation of nanoparticles is characterized by $S(Q)$ of mass fractal or surface fractal as given in equation 2.40 and 2.41 (chapter 2). The mass fractal structure is also used for the bead-necklace model of protein-surfactant complex as given in equation 3.2 (chapter 3).

The data have been analyzed by comparing the scattering from the combination of different models to the experimental data. The corrections for instrumental smearing were made throughout the data analysis [222]. The fitted parameters in the analysis were optimized by means of nonlinear least-square fitting program [151]. The fitted data are represented by the solid lines to the experimental data points.

6.4. Results and discussion

6.4.1. Characterization of individual components

The individual components 1 wt% HS40 silica nanoparticles, 1 wt% BSA protein and 50 mM SDS/DTAB surfactants are same as discussed in chapters 3 and 4. The SANS data of

50 mM C12E10 surfactant along with 50 mM SDS or DTAB surfactant and their mixed systems are shown in Figure 6.1. The C12E10 micelles are fitted with $P(Q)$ of spherical hydrophobic core and shell of hydrophilic Gaussian chains around the core [184]. The radius of the micellar core and radius of gyration of hydrophilic chains around the core are found to be 17.3 Å and 12.2 Å, respectively [193]. The structure factor $S(Q)$ of hard sphere potential is used to account for repulsion between the micelles as given in equation 2.28 (chapter 2) . The fitted parameters of C12E10 along with SDS/DTAB and their mixed micelles are given in **Table 6.1.** The data of mixed micelles are fitted similar to nonionic micelles. This possibly works because of the larger hydrophilic region of the nonionic micelles, which can hide the head group of ionic surfactant in mixed micelles. The behavior of nonionic surfactant with nanoparticle and protein as well as in the three-component nanoparticle-protein-surfactant system is compared with those of ionic surfactants (SDS and DTAB). The role of mixing of nonionic and ionic surfactant in these systems is also addressed.

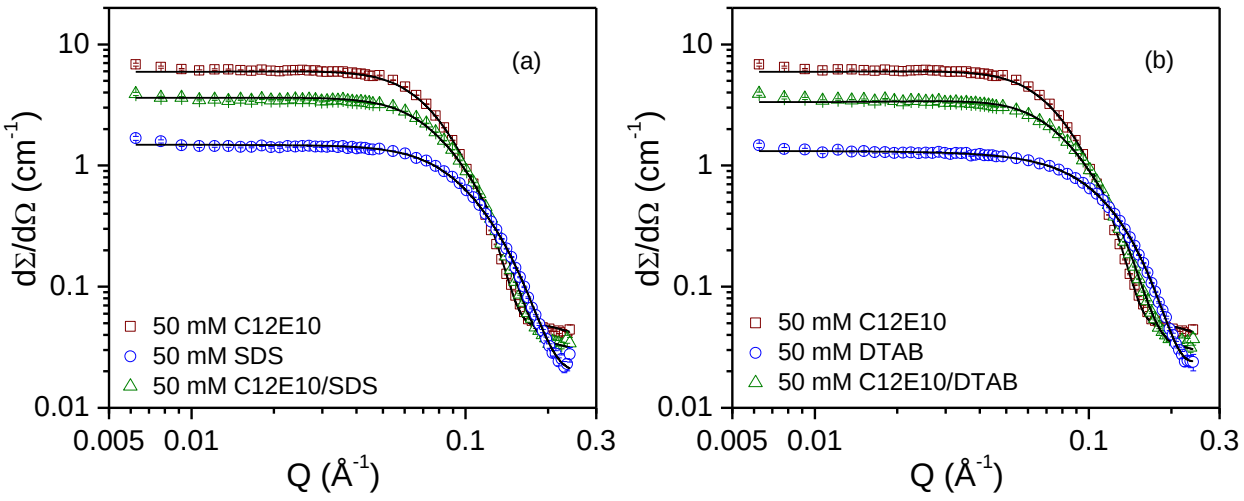

Figure 6.1. SANS data of 50 mM C12E10 surfactants compared with (a) 50 mM SDS and 50 mM C12E10/SDS mixed surfactants (b) 50 mM DTAB and 50 mM C12E10/DTAB mixed surfactants at pH=7 and 0.2 M NaCl in D_2O.

Table 6.1. The structural parameters of 50 mM of different pure and mixed surfactant solutions at pH=7 and 0.2 M NaCl in D_2O.

System	Shape	Structural dimensions		
Polyoxyethylene 10 lauryl ether (C12E10)	Spherical core-shell	Radius of core R = 17.3 Å	Shell size $^{*}R_g$ = 12.2 Å	Aggregation number N = 62
Dodecyl trimethylammonium bromide (DTAB)	Prolate core-shell ellipsoidal ($\varepsilon > 1$)	Semi-minor axis R =16.7±0.2 Å	Semi-major axis εR = 21.0±0.4 Å	Shell thickness t = 5.8 Å
		Aggregation number N = 70±4	Charge Z = +21±2 e.u.	
Sodium dodecyl sulfate (SDS)	Prolate core-shell ellipsoidal ($\varepsilon > 1$)	Semi-minor axis R =16.7±0.2 Å	Semi-major axis εR = 29.0±0.4 Å	Shell thickness t = 5.0 Å
		Aggregation number N = 97±4	Charge Z = -25±2 e.u.	
C12E10/SDS	Spherical core-shell	Radius of core R = 17.3 Å	Shell thickness t = 10.3 Å	Aggregation number N = 62
C12E10/DTAB	Spherical core-shell	Radius of core R = 17.3 Å	Shell thickness t = 10.0 Å	Aggregation number N = 62

*Radius of gyration of hydrophilic chain

The scattering from three-component silica nanoparticle-BSA protein-C12E10 surfactant system is shown in Figure 6.2. The scattering curve shows linear build up of scattering in the low *Q* range, nearly flat scattering in intermediate *Q* range and followed by fall in scattering in high *Q* range. The strong build up of scattering in low *Q* range is indication of some aggregation among the particles. The three-component systems with ionic surfactants (SDS and DTAB) had also shown the aggregation behavior, but the features observed with the nonionic surfactant are significantly different than those of ionic surfactants (Figure 6.2).The role of mixed surfactants in three-component nanoparticle-protein-surfactant system is also studied using C12E10/SDS and C12E10/DTAB mixed surfactants. SANS data of three-component system with mixed

(ionic-nonionic) surfactants are significantly different than nonionic surfactants (Figure 6.3). The data are understood in terms of the interaction of different two-component systems.

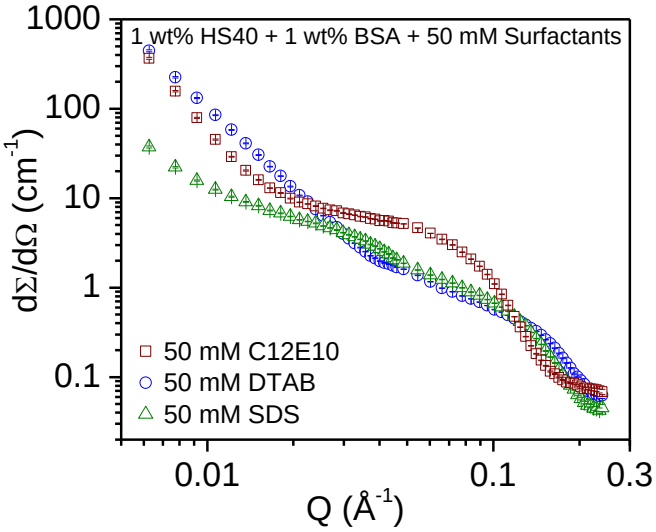

Figure 6.2. SANS data of 1wt% HS40 with 1 wt% BSA protein and 50 mM nonionic C12E10 surfactants compared to similar system with anionic SDS and cationic DTAB surfactants at pH=7 and 0.2 M NaCl in D_2O.

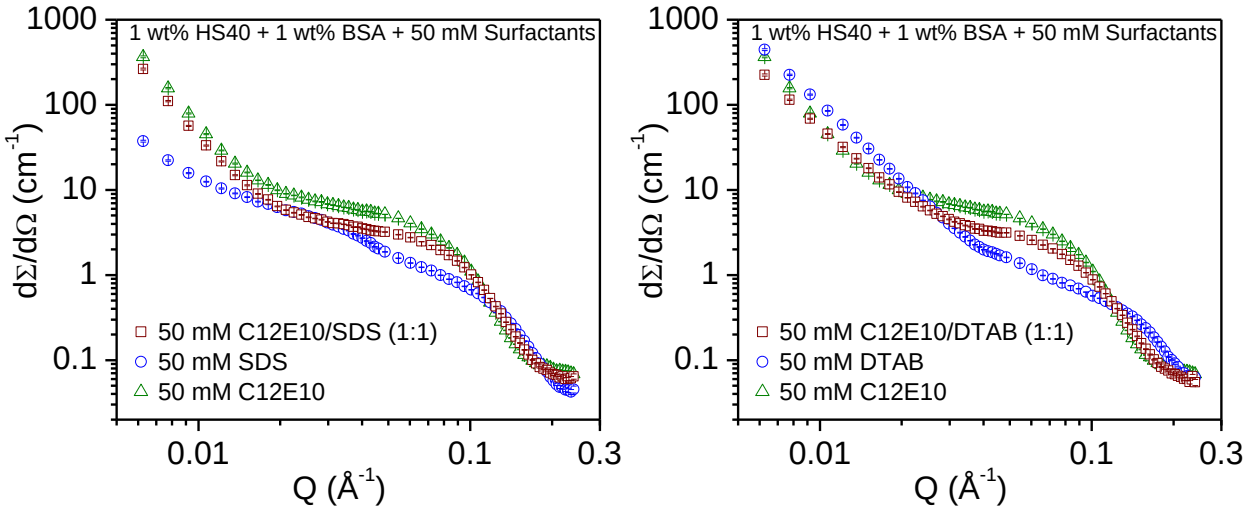

Figure 6.3. SANS data of 1wt% HS40 with 1 wt% BSA protein and (a) 50 mM of mixed C12E10/SDS surfactants compared to similar system with nonionic C12E10 and anionic SDS surfactants, (b) 50 mM of mixed C12E10/DTAB surfactants compared to similar system with nonionic C12E10 and cationic DTAB surfactants at pH=7 and 0.2 M NaCl in D_2O.

6.4.2. Characterization of two-component systems

The nanoparticle-protein interaction is same as discussed in Chapters 4 and 5, where the non-adsorption of protein on nanoparticles result in depletion force induced nanoparticle aggregation [219,225]. Therefore, the other two-component interactions which are important for the there-component system with nonionic surfactant are nanoparticle-surfactant and protein-surfactant interactions. SANS data of 1 wt% HS40 silica nanoparticles with 50 mM C12E10 surfactants are given in Figure 6.4. These data are clearly very different from that of the sum of individual components. The features in the low *Q* region are that of the nanoparticle aggregation in the system. It is known that C12E10 micelles in salt free solutions have tendency to adsorb on the nanoparticles and enhance their stability [81,226]. However, in the present case where there is salt (0.2 M) in the system, the micelles become non-adsorbing. This non-adsorption of micelles similar to that of protein gives rise to the depletion induced aggregation of the nanoparticles [227-229]. The SANS data of nanoparticle-C12E10 surfactant system compared with nanoparticle-BSA protein under the solution condition with micelle and protein contrast-matched are shown in Figure 6.5). There are differences in the data of silica nanoparticles with C12E10 and BSA in the low as well as in intermediate *Q* regions. The slope of the data is higher for C12E10 than BSA in the low *Q* region and Bragg-peak like behavior is observed only for C12E10 surfactants. The slope of data for C12E10 is around 3.5, which suggests the surface fractal morphology of nanoparticle aggregates. However, the aggregation of nanoparticles with BSA protein is mass fractal (chapters 4 and 5). The different morphology of nanoparticle aggregates with C12E10 and BSA protein is expected from the different charge nature of C12E10 and BSA, whereas the effective sizes of both of them are very similar. The non-ionic surfactants form surface fractals with nanoparticles as they show strong depletion interaction because of week micelle-micelle repulsion as compared to protein-protein charged repulsions. SANS data have also been taken from the two-component system with nonionic surfactant, where nanoparticles are contrast-matched. One would have expected the data of two-component system to match with that of individual nonionic micelles, however the data show

strong additional scattering in the low *Q* region. This contribution can be explained by the trapped micelles in the nanoparticle aggregates [228].

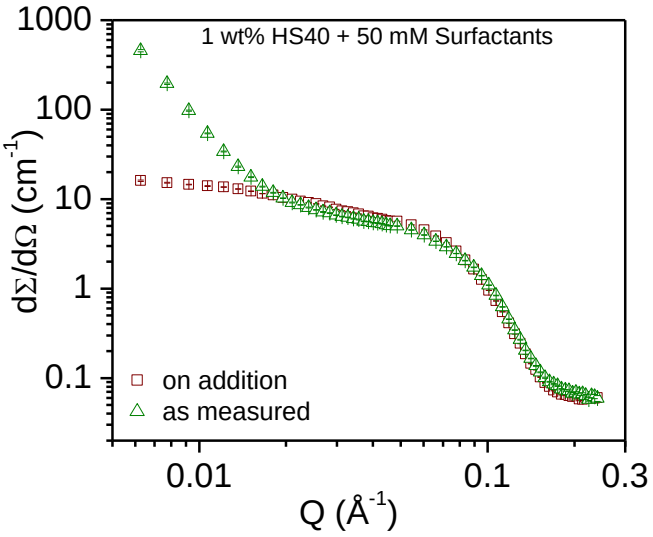

Figure 6.4. SANS data of 1 wt% HS40 nanoparticles with 50 mM of nonionic C12E10 surfactants compared to the sum of scattering of individual components (1 wt% HS40 nanoparticles and 50 mM nonionic C12E10 surfactants) at pH=7 and 0.2 M NaCl in D_2O.

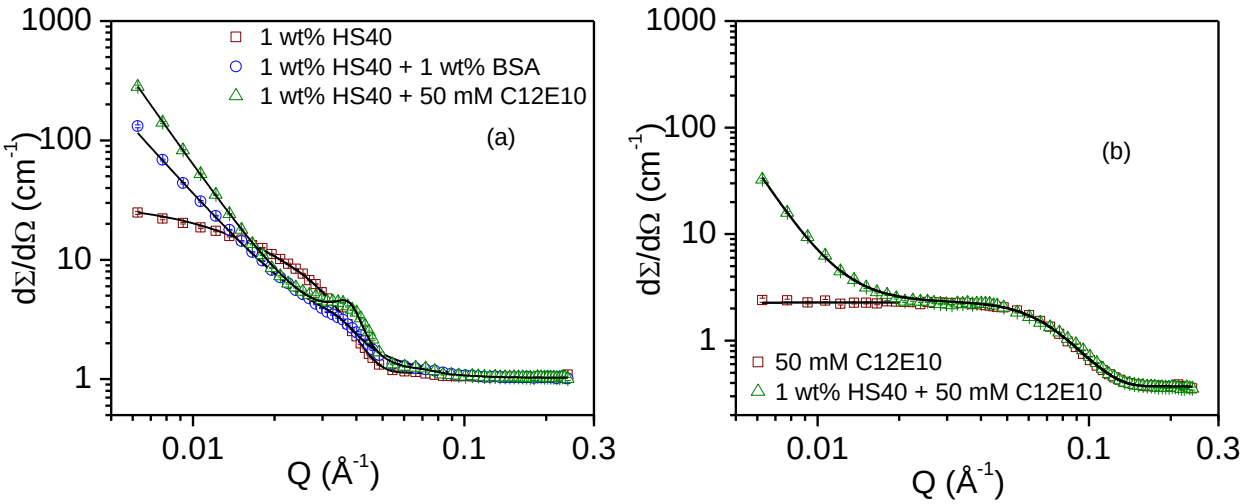

Figure 6.5. SANS data of (a) 1 wt% HS40 nanoparticles with 50 mM of nonionic C12E10 surfactants compared with individual nanoparticles and 1 wt% HS40 nanoparticles with 1 wt% BSA protein under micelles contrast matched, (b) 1 wt% HS40 nanoparticles with 50 mM of nonionic C12E10 surfactants compared with individual nonionic C12E10 surfactants with nanoparticles contrast matched at pH=7 and 0.2 M NaCl.

The interaction behavior of silica nanoparticles with mixed nonionic-ionic surfactants is examined in Figure 6.6. It has already been observed that silica nanoparticles show aggregation with DTAB and C12E10 surfactants. The individual nanoparticles coexist with the micelles in the case of SDS surfactant. However, both the DTAB and SDS mixed with the C12E10 surfactant show nanoparticle aggregation (Figure 6.6). The mechanism of the nanoparticle aggregation with mixed surfactants is further examined by the contrast-matching SANS experiments. SANS data of the same system with (a) micelles contrast-matched and (b) nanoparticles contrast-matched are shown in Figure 6.7. The features of C12E10-SDS mixed surfactants seem to be more like that of C12E10 surfactant with nanoparticles, whereas those of C12E10-DTAB mixed surfactants similar to DTAB surfactant with nanoparticles [inset in figure 6.7(a & b)]. In the case of C12E10-SDS, both components C12E10 and SDS are non-adsorbing on nanoparticles. The mixed micelles of these components behave like nonionic micelles and hence induce a depletion interaction between nanoparticles similar to that of C12E10 micelles [25,203,228]. The nanoparticle aggregates are surface fractal with C12E10-SDS mixed surfactants [Figure 6.7(a)]. In the case of nanoparticles contrast matched [Figure 6.7(b)], the scattering of C12E10-SDS mixed micelles is significantly lowered because of the smaller volume fraction of the mixed micelles than that of nonionic micelles for the same molar concentration of surfactants [Figure 6.1.(a)]. The scattering data of C12E10-DTAB mixed micelles are significantly different from that of C12E10 surfactant, but similar to that DTAB surfactant with nanoparticles. If C12E10-DTAB mixed micelles will behave more like nonionic micelles, then they cannot adsorb on nanoparticles. This contradicts to the experimental observation of similar behavior of C12E10-DTAB and DTAB with nanoparticles [inset of Figure 6.7(a & b)]. Therefore, the modeling of C12E10-DTAB mixed surfactants with

nanoparticles has been done using two kinds of micelles: (i) ionic micelles of DTAB which adsorb on the nanoparticles and lead to their aggregation and (ii) remaining DTAB surfactant forming non-adsorbing mixed micelles with C12E10 surfactant.

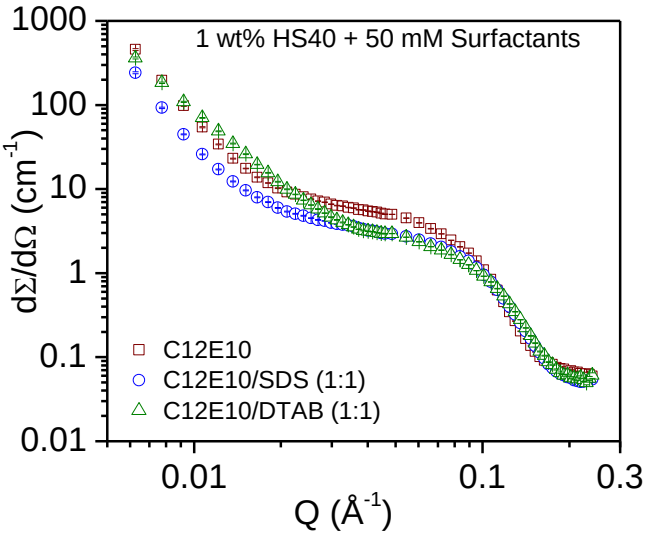

Figure 6.6. SANS data of 1 wt% HS40 nanoparticles with 50 mM of mixed C12E10/SDS, C12E10/DTAB and nonionic C12E10 surfactants at pH=7 and 0.2 M NaCl in D_2O.

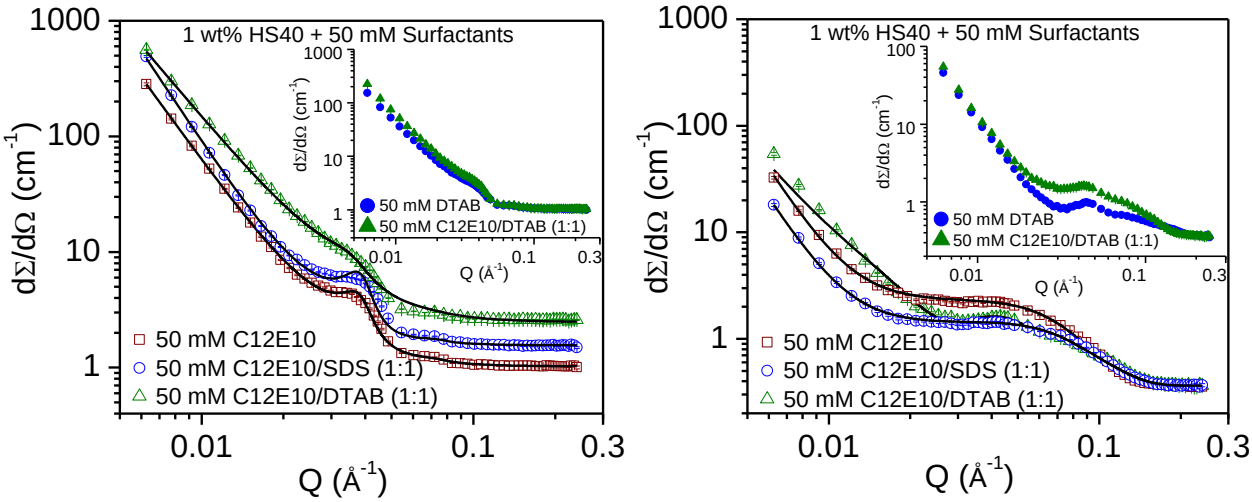

Figure 6.7. SANS data of 1 wt% HS40 nanoparticles with 50 mM of mixed C12E10/SDS, C12E10/DTAB and nonionic C12E10 surfactants under different contrast conditions, (a) surfactant contrast matched and (b) nanoparticles contrast matched at pH=7 and 0.2 M NaCl. Inset in both the figures shows the comparison of nanoparticles-C12E10/DTAB surfactant system with nanoparticles-DTAB surfactant system under micelles and nanoparticles contrast matched condition.

The two-component protein-surfactant interaction has been found to be strongly depending on the charge nature of the surfactant (chapter 3). SANS data of BSA protein interaction with nonionic surfactant and mixed nonionic-ionic surfactants are given in Figure 6.8. The BSA protein and nonionic surfactant do not show any interaction [193]. Figure 6.8(a) clearly supports to this point where the scattering from BSA with C12E10 micelles is sum of the scattering from BSA and C12E10 micelles. This is believed to be due to absence of electrostatic interaction between the components. The BSA protein interaction with nonionic-ionic mixed surfactants is found to be similar to nonionic surfactants [Figure 6.8(b)]. The protein and mixed micelles coexists individually in the system. The non-adsorption of mixed micelles to protein is driven by the dominance of ionic-nonionic mixed micellization over the binding of ionic surfactants with the protein.

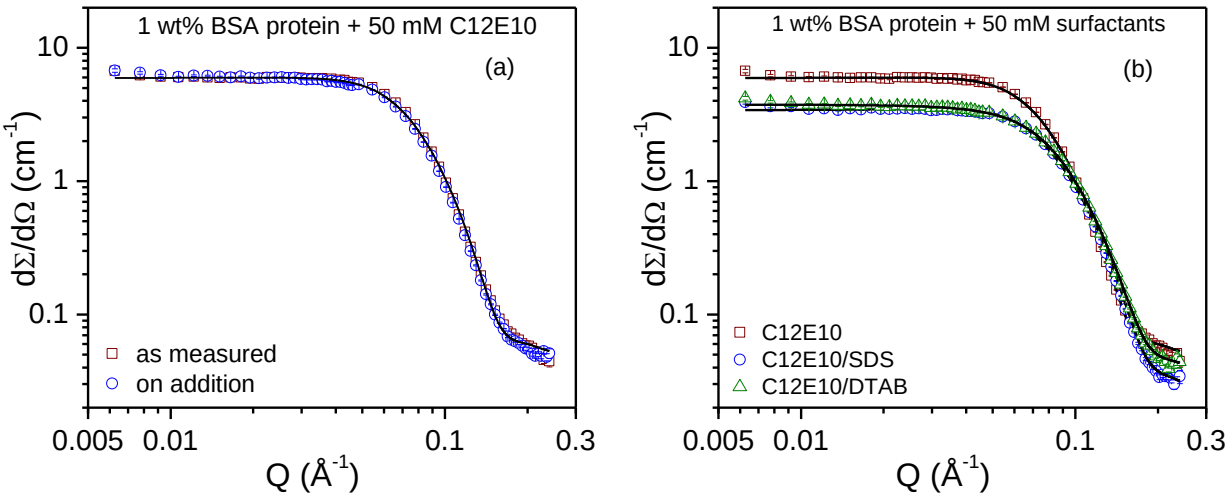

Figure 6.8. SANS data of 1 wt% BSA protein with (a) 50 mM C12E10 surfactant compared with sum of scattering of individual components and (b) C12E10/SDS, C12E10/DTAB mixed surfactants and nonionic C12E10 surfactants at pH=7 and 0.2 M NaCl in D_2O.

6.4.3. Characterization of three-component systems

The three-component, nanoparticle-protein-surfactant system with nonionic surfactant show nanoparticle aggregation, which could arise because of either nanoparticle-BSA and/or nanoparticle-surfactant [Figure 6.5(a)] interactions. The role of these two-component interactions in the three-component system is compared in Figure 6.9. It is clearly observed that the data of nanoparticle-protein are very different from that of nanoparticle-protein-surfactant system. However, the data of nanoparticle-surfactant match with that of the nanoparticle-protein-surfactant system. In the present nanoparticle-protein-surfactant system, both the protein and surfactant are non-adsorbing to the nanoparticles (Figure 6.5). Also the protein and surfactant do not form any complex and remain individually [Figure 6.8(a)]. Therefore, the aggregation of nanoparticles is expected to be induced by the combined depletion interaction of protein and surfactant. The fact that overall sizes of the protein and nonionic micelle are almost same, the nanoparticle aggregation is believed to be dominated by the nonionic micelles because of the absence of electrostatic repulsion between them [228].

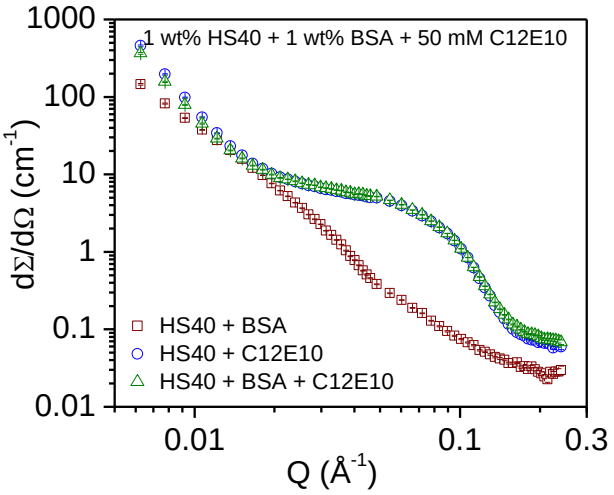

Figure 6.9. SANS data of 1 wt% HS40 nanoparticles with 1 wt% BSA protein and 50 mM of C12E10 surfactant compared with two-component 1 wt% HS40 nanoparticle with 1 wt% BSA protein and 1 wt% HS40 with 50 mM of C12E10 surfactant systems at pH=7 and 0.2 M NaCl in D_2O.

The three-component nanoparticle-protein-surfactant system with nonionic surfactant is further examined under the contrast conditions (a) micelles are contrast matched and (b) nanoparticle are contrast matched. Figure 6.10(a) shows that nanoparticle-protein-surfactant system exactly match to the nanoparticle-surfactant system when the micelles are contrast matched. In this contrast condition, the scattering from protein is also minimized. The results thus confirm that protein-surfactant effect is identical to the surfactant effect alone with nanoparticles. The data are fitted in linear low Q region with the surface fractal aggregates of the nanoparticles and for hump in the inter-mediate Q region with hard sphere interaction for the nanoparticles within the aggregate. The surface fractal dimension (D_s) is found to be 2.75. The volume fraction of nanoparticles within the aggregates is around 0.40, which is quite low as compared to that in crystalline systems. In the case when silica nanoparticles are contrast-matched [Figure 6.10(b)], the data of nanoparticle-protein-surfactant and nanoparticle-surfactant systems are again found similar. The scattering from BSA protein is not observed because of the low contrast of protein as compared to that for micelles (Figure 3.1).

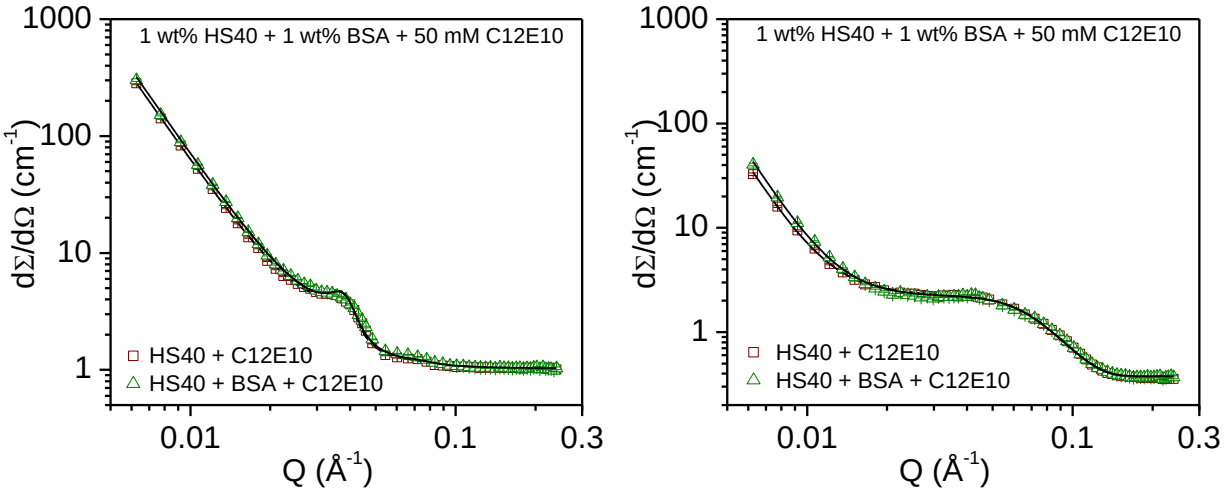

Figure 6.10. SANS data of 1 wt% HS40 nanoparticles with 1 wt% BSA protein and 50 mM C12E10 surfactant system compared with scattering from nanoparticle-surfactant system under different contrast conditions (a) Micelles contrast matched and (b) nanoparticles contrast matched at pH=7 and 0.2 M NaCl.

SANS data of three-component nanoparticle-protein-surfactant system with nonionic-ionic (C12E10/SDS) surfactants under the solution conditions (a) micelles contrast-matched and (b) nanoparticles contrast-matched are shown in Figure 6.11(a & b). It had been observed that the structures of nanoparticle-C12E10 surfactant and nanoparticle-C12E10/SDS surfactants are similar. Also the interactions of protein-C12E10 and protein-C12E10/SDS

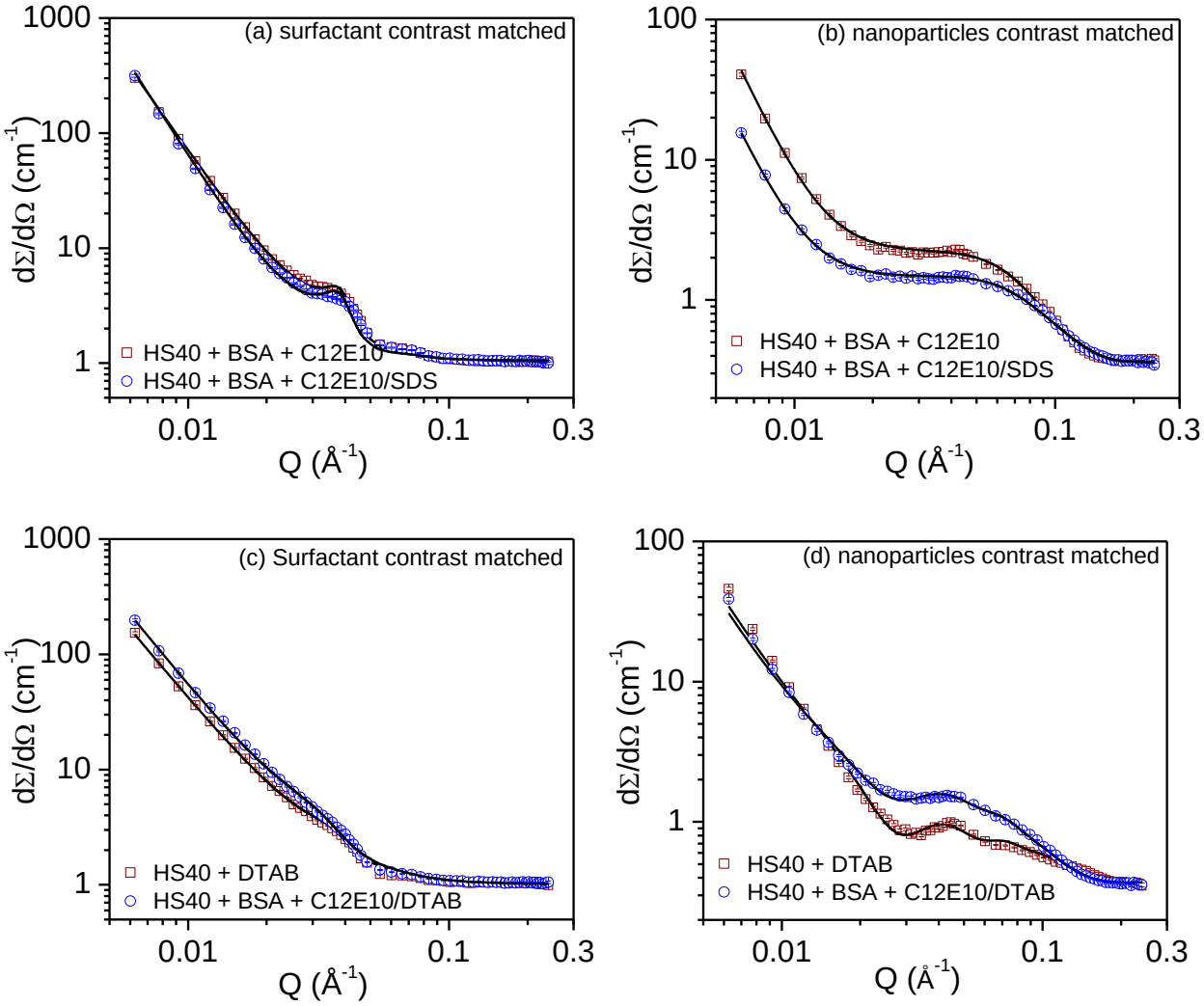

Figure 6.11. SANS data of 1 wt% HS40 nanoparticles with 1 wt% BSA protein and 50 mM of mixed C12E10/SDS surfactants compared with scattering from nanoparticle-protein-C12E10 surfactant system under different contrast conditions (a) surfactant contrast matched (b) nanoparticles contrast matched. SANS data of 1 wt% HS40 nanoparticles with 1 wt% BSA protein and 50 mM of mixed C12E10/DTAB surfactants compared with scattering from nanoparticle-C12E10 surfactant system under different contrast conditions (c) surfactant contrast matched (d) nanoparticles contrast matched at pH=7 and 0.2 M NaCl.

surfactants are similar. Therefore, the SANS data of nanoparticle-protein-surfactant having mixed C12E10/SDS surfactants are compared with the nanoparticle-protein-surfactant having C12E10 surfactant for their similarity. The measured data are found to quite similar. These systems consist of surface fractal aggregates of nanoparticles coexisting with individual protein and mixed micelles. In the case of nanoparticles are contrast-matched, the data show two populations of micelles as trapped in nanoparticle aggregates (buildup in low *Q* data) and free micelles in solution [228]. Unlike the case of C12E10/SDS, the two-component interaction of C12E10/DTAB with nanoparticles is decided by the nanoparticle-DTAB interaction [185,225]. However, the protein-mixed surfactant interaction for both C12E10/SDS and C12E10/DTAB is same (chapter 3). The micelle contrast-matched SANS data of nanoparticle-protein-surfactant having C12E10/DTAB mixed surfactants are found to be similar to that of nanoparticle-DTAB surfactant [Figure 6.11(c)]. The data are fitted with the mass fractal aggregates of nanoparticles and aggregation is believed to be mediated by the DTAB micelles. The protein-micelle complex mediated aggregation as observed for nanoparticle-protein-DTAB system (chapter 5) is not favored for nanoparticle-protein-C12E10/DTAB system since no protein interaction has been found with C12E10/DTAB. Figure 6.11(d) shows the comparison of nanoparticle-protein-C12E10/DTAB with nanoparticle-DTAB when nanoparticles are contrast-matched. The data of these two systems almost match in the low *Q* region, whereas significant difference in the higher *Q* region. The similarity in the low *Q* region confirms the similar mechanism of nanoparticle aggregation in these systems and differences in the high *Q* regions are due to different free micelles in the systems.

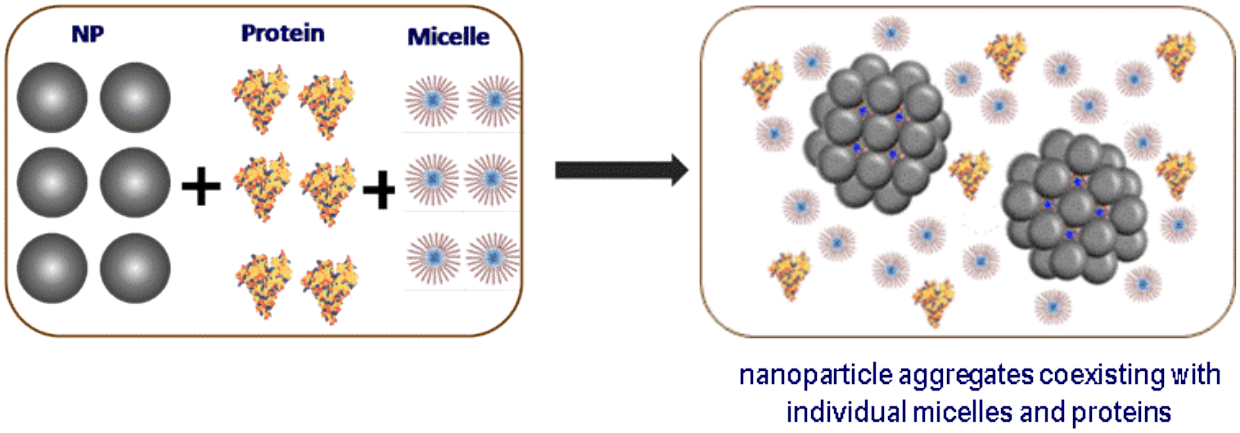

Figure 6.12. Schematic of structures formed in three-component system of anionic silica nanoparticles, anionic BSA protein and nonionic C12E10 surfactant.

Table 6.2. The fractal dimension of nanoparticle aggregates in presence of different components.

Sample	Morphology of aggregates	Fractal dimension
HS40 + C12E10	Surface fractal	D_s=2.75±0.20
HS40 + C12E10/SDS	Surface fractal	D_s=2.45±0.20
HS40 + C12E10/DTAB	Mass fractal	D_m=2.75±0.20
HS40 + C12E10 + BSA	Surface fractal	D_s=2.75±0.20
HS40 + C12E10/SDS + BSA	Surface fractal	D_s=2.55±0.20
HS40 + C12E10/DTAB + BSA	Mass fractal	D_m=2.75±0.20

The nonionic C12E10 micelles show depletion force induced fractal aggregation in nanoparticles (Figure 6.5). The use of C12E10/SDS and C12E10/DTAB mixed micelles will add additional charge to micelles, which will tune the depletion force experienced by nanoparticles as well as nanoparticle aggregation in solution. SANS scattering profile of 1 wt% HS40 silica nanoparticles with 50 mM of C12E10/SDS, C12E10/DTAB and C12E10 micelles are compared under micelle contrast matched condition to understand the correlation among nanoparticles is

shown in [Figure 6.7(a)]. The common feature among the three scattering curves is the linear scattering profile in low *Q* range [163,185,228]. The slope of linearity in the low *Q* range is highest for mixed surfactants C12E10/SDS followed by nonionic C12E10 and then mixed surfactants C12E10/DTAB with nanoparticles. The corresponding morphology of nanoparticle aggregates and fractal dimension is surface fractal for mixed surfactants C12E10/SDS (D_s=2.45) followed by nonionic C12E10 (D_s=2.75) and mass fractal for mixed surfactants C12E10/DTAB (D_m=2.75) with nanoparticles. The another common feature in C12E10/SDS and C12E10 system is the hump in intermediate *Q* range which disappears for the case of C12E10/DTAB mixed surfactant system. The hump in intermediate *Q* range is the correlation peak for the cluster formation in C12E10/SDS and C12E10 system [203,228]. The scattering profile of C12E10/DTAB mixed surfactant system is very similar to that of DTAB surfactant system with similar fractal dimension (D_m=2.75) [inset of figure 6.7(a)]. The results propose that the depletion force which is responsible for aggregating the nanoparticles is weaken for C12E10/DTAB and strengthen for C12E10/SDS as compared to C12E10 micelles based on packing of nanoparticles in aggregates. The possible reason for enhanced depletion force for C12E10/SDS with nanoparticles is the soft repulsion of depletant C12E10/SDS micelles with nanoparticles and corresponding reduced depletion force is because of adsorption of DTAB micelles on nanoparticles [25].

6.5. Conclusions

The structure and interaction in three-component nanoparticle-protein-surfactant systems with nonionic C12E10 surfactant and mixed nonionic-ionic (C12E10-SDS and C12E10-DTAB) surfactants have been investigated. The systems are analyzed in terms of two-component (nanoparticle-protein, nanoparticle-surfactant and protein-surfactant) interactions. The non-adsorption of both BSA protein and nonionic C12E10 surfactants show depletion force induced

aggregation in two-component nanoparticle-protein and nanoparticle-surfactant systems [26]. The morphology of nanoparticle aggregates is surface fractal with more close packing for nonionic C12E10 and mass fractal for anionic BSA protein mediated nanoparticle aggregates. BSA protein and nonionic C12E10 surfactants remains independently in solution. In the three-component nanoparticle-protein-surfactant system, the strong depletion force of nonionic C12E10 micelles dominates over that of BSA protein to aggregate nanoparticles with morphology similar to nanoparticle-surfactant system coexisting with free BSA protein and nonionic C12E10 surfactants in solution. In the case of C12E10-SDS mixed surfactants, the mixed micelles behave very similar to nonionic C12E10 surfactant to produce depletion force induced nanoparticle aggregates and for the case of C12E10-DTAB mixed surfactants behave similar to cationic DTAB surfactant to produce adsorption-mediated nanoparticle aggregates in solution. For the case of C12E10-DTAB mixed surfactants the aggregates are mediated by adsorption of cationic DTAB micelles instead of DTAB/C12E10 mixed micelles in solution. In all these systems, BSA protein remains unaffected and resultant structures are driven by the interaction of surfactant micelles with nanoparticles.

Chapter 7

Summary

Nanoparticles, proteins and surfactants are three major components in soft condensed matter [3,12,230]. Each one of these is extensively used for specific applications [106,119,127,171,231-233]. Further, many additional applications arise by adjoining these components together to obtain interesting functional objects [34,37,99,129,131,134,234-235]. The nanometer length scale in these systems is believed to be important to decide their macroscopic properties [118,185]. The present thesis provides an understanding of the complex structures in these multi-component systems. The charged silica nanoparticles, BSA protein and three different surfactants (SDS, DTAB and C12E10) have been used as model systems. The systems are characterized by scattering techniques SANS and DLS. In particular, SANS with easy possibility to vary the contrast is an ideal technique to study such multi-component systems.

The thesis consists of seven chapters including this chapter on summary of thesis. Chapter 1 gives a general introduction on structure and function of proteins, self-assembly of surfactants and characteristics of nanoparticles. The interest in nanoparticle-protein-surfactant complexes and layout of thesis are also discussed in chapter 1. The details of experimental techniques SANS and DLS as used are described in chapter 2. The results of thesis are given in chapters 3 to 6. The structure and interaction of protein-surfactant complexes under different solution conditions are presented in chapter 3. The nanoparticles effect on protein-surfactant complexes with different surfactants are discussed in chapters 4-6. The results of anionic nanoparticles on anionic protein-anionic surfactant complexes (all the components are similarly

charged) are discussed in chapter 4. The study on nanoparticle effect on protein-surfactant complexes using cationic surfactant and their comparison with anionic surfactant (chapter 4) are reported in chapter 5. The nanoparticle effect on protein-surfactant complexes using nonionic surfactant and tuning by nonionic-ionic mixed surfactants is studied in chapter 6.

A general introduction to proteins, surfactants, nanoparticles is given in chapter 1. Proteins are the polymers of amino acids with a specific three-dimensional shape and charge on them. The structures of proteins, interactions in protein solutions and types of proteins are discussed in details. In this thesis, globular protein BSA has been used as a model system, which has a molecular weight of 66.4 kDa and its isoelectric point is at pH=4.7 [50]. Surfactants are amphiphilic molecules and can self-assemble to different structures [13,67]. Their classification, micelle formation and different structures of micelles are discussed. The three different surfactants [anionic sodium dodecyl sulphate (SDS), cationic dodecyl trimethylammoniumbromide (DTAB) and nonionic polyoxyethylene 10 lauryl ether (C12E10)] have been used in this thesis. Nanoparticles are particles between 1 and 100 nm in size. The characteristics of nanoparticles, synthesis methods and some important applications requiring their conjugation with protein-surfactant are also discussed [105,115,118,201]. Charge-stabilized silica nanoparticles have been used in the present thesis because of their easy preparation, high stability, low toxicity and ability to be functionalized with a range of macromolecules [115-116]. A layout of thesis is discussed in the end of this chapter.

The experimental techniques SANS and DLS are described in chapter 2. These techniques can be used for characterization of length scale (1 to 100 nm) where most of the structures of protein, micelles and nanoparticle exist. SANS is a diffraction experiment measuring the scattered neutron intensity as a function of wave vector transfer Q ($=4\pi\sin\theta/\lambda$,

where λ is the incident neutron wavelength and 2θ is the scattering angle). The scattered intensity as given by $I(Q) \sim (\rho_p - \rho_s)^2 \times P(Q) \times S(Q)$, where $P(Q)$ is the intraparticle structure factor and $S(Q)$ is the interparticle structure factor [143]. $P(Q)$ is the square of particle form factor and decided by the shape and size of the particle. $S(Q)$ depends on the spatial arrangement of particles and is thereby sensitive to interparticle interactions. The magnitude of the scattered neutron intensity in the SANS experiments depends on contrast factor $[(\rho_p - \rho_s)^2]$, the square of the difference between the average scattering length densities of the particle and the medium. Due to the fact that the scattering lengths are very different for hydrogen and deuterium, SANS is ideally suited for studying the multi-components systems by selectively contrast matching the components with the partial deuteration of the components. In addition to SANS, DLS is used wherever possible to compliment the SANS results [144]. This technique is also described in chapter 2.

The main results of the thesis as given in Chapters 3 - 6 are:

The structure and interaction of anionic BSA protein with anionic SDS, cationic DTAB and nonionic C12E10 surfactants have been studied in chapter 3. It is found that ionic and nonionic surfactants show very different interactions with protein [193,217-218]. The ionic surfactants bind to the protein by the site-specific electrostatic interaction and forming micelle-like clusters along the unfolded protein chain. On the other hand, nonionic surfactants do not interact with protein and coexist independently with unperturbed folded protein. The interaction of protein and ionic surfactant can be enhanced by increasing ionic strength and/or surfactant concentration. The ionic surfactant binding to proteins follows three concentration regions (specific binding, cooperative binding, and saturation). Further, the use of nonionic-ionic mixed surfactants is shown to fold back unfolded protein as well as to prevent ionic surfactant induced

protein unfolding. This behavior is explained as a result of the dominance of hydrophobic interaction of mixed surfactants over the electrostatic binding of ionic surfactant with protein. The bead-necklace structure of protein-surfactant system is characterized by the mass fractal structure and results are interpreted in terms of change in the fractal dimension, overall size of the protein-surfactant complex and number of micelles attached to the protein.

The effect of anionic silica nanoparticles with anionic BSA protein and anionic SDS surfactant has been examined in chapter 4 [219-220,236]. Although all the components are similarly charged, strong structural evolutions amongst them have been observed. The properties of nanoparticle interaction with protein-surfactant system are determined by the different possible interactions of components with each other (e.g. nanoparticle-protein, nanoparticle-surfactant and protein-surfactant). Surfactants interact cooperatively with the protein to form bead-necklace structure comprising micelle-like clusters of the surfactant along the unfolded protein chain. In nanoparticle-protein system, the nanoparticle aggregates are formed through the depletion force of non-adsorbing protein to the nanoparticles. On the other hand, no physical interaction is observed between the components for nanoparticle-surfactant system. The resultant structural behavior of the three-component system is explained via synergetic effect of two-component nanoparticle-protein and protein-surfactant interactions. The non-adsorption of protein-surfactant complex on nanoparticles result in depletion induced nanoparticle aggregation (similar to nanoparticle-protein system) coexisting with the protein-surfactant complexes. Both the bead-necklace structure of protein-surfactant complexes and nanoparticle aggregates are characterized by the mass fractals. The protein unfolding as well as nanoparticle aggregation is found to be enhanced in the three-component system as compared to the corresponding two-component systems.

The modifications in the structure and interaction of cationic DTAB vs. anionic SDS surfactant for nanoparticle effect in protein-surfactant systems are reported in chapter 5. In both the cases (DTAB and SDS), the structure of nanoparticles in protein-surfactant systems is predominantly determined by the interactions of individual two components [225,237]. The nanoparticle-surfactant and protein-surfactant interactions for DTAB unlike nanoparticle-protein and protein-surfactant for SDS are found to be responsible for the resultant structure of nanoparticle-protein-surfactant complexes. Irrespective of the charge on the surfactant, both of them form the similar kind of bead-necklace structure with the protein. The adsorption of these protein-surfactant complexes for DTAB on oppositely charged nanoparticles gives rise to the protein-surfactant complex mediated aggregation of nanoparticles (similar to that as observed with DTAB surfactant). It is different from that of depletion induced aggregation of nanoparticles with non-adsorption of protein-surfactant complexes for SDS in similarly charged nanoparticle systems (similar to that of protein alone). The micelles are found to be rearranging on adsorption of protein-surfactant complex on the nanoparticles in leading to their (nanoparticle) aggregation. The role of DTAB than SDS is found to be interestingly different, where nanoparticle-protein (mediated through protein-surfactant complex) and protein-surfactant for SDS decide their resultant structure. It is thus shown that the structure and interaction of three-component nanoparticle-protein-surfactant systems can simply be modified by the change in the charge state of the surfactant.

Chapter 6 provides the effect of nanoparticles on protein-surfactant systems with nonionic C12E10 and mixed nonionic-ionic (C12E10-SDS and C12E10-DTAB) surfactants [238]. The interactions in three-component system with nonionic surfactant are interpreted in terms of competition of two-component nanoparticle-protein and nanoparticle-surfactant

interactions. The non-adsorption of both anionic BSA protein and nonionic C12E10 surfactants show depletion force induced aggregation in two-component nanoparticle-protein and nanoparticle-surfactant systems [228]. The morphology of nanoparticle aggregates is surface fractal with more close packing for nonionic C12E10 and mass fractal for anionic BSA protein mediated nanoparticle aggregates. BSA protein and nonionic C12E10 surfactants remains independently in solution. In the ternary nanoparticle-protein-surfactant system, the strong depletion force of nonionic C12E10 micelles dominates over that of anionic BSA protein to aggregate nanoparticles with morphology similar to nanoparticle-surfactant system coexisting with free BSA protein and nonionic C12E10 surfactants in solution. In the case of C12E10-SDS mixed surfactants, the mixed micelles behave very similar to nonionic C12E10 surfactant to produce depletion force induced nanoparticle aggregates and for the case of C12E10-DTAB mixed surfactants behave similar to cationic DTAB surfactant to produce adsorption-mediated nanoparticle aggregates in solution. For the case of C12E10-DTAB mixed surfactants the aggregates are mediated by adsorption of cationic DTAB micelles instead of DTAB/C12E10 mixed micelles in solution. In all these systems, BSA protein remains unaffected and resultant structures are driven by the interaction of surfactant micelles with nanoparticles.

To conclude, the structural evolution of nanoparticle effect in protein-surfactant systems have been investigated. The charged silica nanoparticles, BSA protein and three different surfactants (SDS, DTAB and C12E10) have been used as model systems. The structure and interaction of BSA protein with ionic (anionic SDS and cationic DTAB) and nonionic C12E10 surfactants are found to very different. The ionic surfactants strongly bind to the protein and form bead-necklace structure, whereas protein does not show any change with the nonionic surfactant. The silica nanoparticle effect in each of these protein-surfactant systems shows that

the surfactant-dependent different microstructures of nanoparticle aggregates (mass and surface fractals) are formed along with enhanced protein-surfactant interactions in the resultant nanoparticle-protein-surfactant systems. The interactions in these systems are governed by the competition of electrostatic (repulsive and/or attractive) and attractive depletion interaction. This thesis provides useful results which can be utilized in nanoparticle applications of drug delivery, phase separation processes and synthesis of functional materials. Future studies will involve examining the nanoparticle effect in protein-surfactant systems with magnetic nanoparticles and other model proteins such as lysozyme [125,209].

References

[1] P. Attard, Adv. Chem. Phys. **92**, 1 (2007).

[2] I. W. Hamley, Angew. Chem. Int. Ed. **42**, 1692 (2003).

[3] R. A. Jones, *Soft condensed matter* (Oxford University Press, New York, 2002).

[4] P. A. Hassan, G. Verma, and R. Ganguly, in *Functional Materials*, edited by S. Banerjee, and A. K. Tyagi (Elsevier, London, 2012).

[5] I. W. Hamley, *Introduction to Soft Matter: Synthetic and Biological Self-Assembling Materials, Revised Edition* (John Wiley & Sons, Ltd, West Sussex, England, 2007).

[6] R. Mezzenga, P. Schurtenberger, A. Burbidge, and M. Michel, Nature Mater. **4**, 729 (2005).

[7] J.-P. Hansen and I. R. McDonald, *Theory of Simple Liquids (Third Edition)* (Academic Press, Burlington, 2006).

[8] E. Dickinson, Trends Food Sci. Technol. **43**, 178 (2015).

[9] E. Dickinson, in *Food Structures, Digestion and Health*, edited by M. Golding, and H. Singh (Academic Press, San Diego, 2014), pp. 3.

[10] J. P. F. Lagerwall and G. Scalia, Curr. Appl. Phys. **12**, 1387 (2012).

[11] M. Kleman and O. D. Lavrentovich, *Soft Matter Physics: An Introduction* (Springer, New York, 2003).

[12] C. N. Likos, Phys. Rep. **348**, 267 (2001).

[13] J. N. Israelachvili, *Intermolecular and Surface Forces (Third Edition)* (Academic Press, San Diego, 2011).

[14] Y. Min, M. Akbulut, K. Kristiansen, Y. Golan, and J. Israelachvili, Nature Mater. **7**, 527 (2008).

[15] E. J. W. Verwey and J. T. G. Overbeek, *Theory of the stability of lyophobic colloids* (Elsevier, Netherlands, 1948).

[16] J.-P. Hansen and I. R. McDonald, *Theory of Simple Liquids (Third Edition)* (Academic Press, Burlington, 2006).

[17] J. Israelachvili, Acc. Chem. Res. **20**, 415 (1987).

[18] K. van Gruijthuijsen, M. Obiols-Rabasa, M. Heinen, G. Nägele, and A. Stradner, Langmuir **29**, 11199 (2013).

[19] C. Tanford, *The hydrophobic effect* (John Wiley & Sons, Inc., New York, 1980).

[20] E. Arunan and D. Mani, Faraday Discuss. **177**, 51 (2015).

[21] E. Arunan *et al.*, Pure and Applied Chemistry **83**, 1637 (2011).

[22] C. L. Perrin and J. B. Nielson, Annu. Rev. Phys. Chem. **48**, 511 (1997).

[23] D. H. Napper, J. Colloid Interface Sci. **58**, 390 (1977).

[24] S. Asakura and F. Oosawa, J. Chem. Phys. **22**, 1255 (1954).

[25] H. N. W. Lekkerkerker and R. Tuinier, *Colloids and the depletion interaction* (Springer, New York, 2011).

[26] D. Frenkel, Physica A **263**, 26 (1999).

[27] L. Feng, B. Laderman, S. Sacanna, and P. Chaikin, Nature Mater. **14**, 61 (2015).

[28] R. D. Kamien, Rev. Mod. Phys. **74**, 953 (2002).

[29] T. Vicsek, A. Czirók, E. Ben-Jacob, I. Cohen, and O. Shochet, Phys. Rev. Lett. **75**, 1226 (1995).

[30] J. Palacci, S. Sacanna, A. P. Steinberg, D. J. Pine, and P. M. Chaikin, Science **339**, 936 (2013).

[31] J. Schwarz-Linek, C. Valeriani, A. Cacciuto, M. E. Cates, D. Marenduzzo, A. N. Morozov, and W. C. K. Poon, Proc. Natl. Acad. Sci. U.S.A. **109**, 4052 (2012).

[32] S. Sacanna, W. T. M. Irvine, P. M. Chaikin, and D. J. Pine, Nature **464**, 575 (2010).

[33] G. M. Whitesides and M. Boncheva, Proc. Natl. Acad. Sci. U.S.A. **99**, 4769 (2002).

[34] A. E. Nel, L. Madler, D. Velegol, T. Xia, E. M. V. Hoek, P. Somasundaran, F. Klaessig, V. Castranova, and M. Thompson, Nature Mater. **8**, 543 (2009).

[35] I. Lynch and K. A. Dawson, Nano Today **3**, 40 (2008).

[36] D. Otzen, Biochim. Biophys. Acta **1814**, 562 (2011).

[37] M. Ospinal-Jiménez and D. C. Pozzo, Langmuir **30**, 1351 (2014).

[38] M. Mahmoudi, I. Lynch, M. R. Ejtehadi, M. P. Monopoli, F. B. Bombelli, and S. Laurent, Chem. Rev. **111**, 5610 (2011).

[39] C. C. Fleischer and C. K. Payne, Acc. Chem. Res. **47**, 2651 (2014).

[40] E. Yasun, C. Li, I. Barut, D. Janvier, L. Qiu, C. Cui, and W. Tan, Nanoscale **7**, 10240 (2015).

[41] S. Dominguez-Medina, J. Blankenburg, J. Olson, C. F. Landes, and S. Link, ACS Sustainable Chem. Eng. **1**, 833 (2013).

[42] S. J. Lee, N. Scotti, N. Ravasio, I. S. Chung, and H. Song, Cryst. Growth Des. **13**, 4131 (2013).

[43] D. Whitford, *Proteins: structure and function* (John Wiley & Sons, England, 2005).

[44] K. A. Dill, Biochemistry **29**, 7133 (1990).

[45] K. A. Dill and J. L. MacCallum, Science **338**, 1042 (2012).

[46] N. Rawat and P. Biswas, J. Phys. Chem. B **118**, 3018 (2014).

[47] A. S. Mahadevi and G. N. Sastry, Chem. Rev. **116**, 2775 (2016).

[48] S.-H. Chong and S. Ham, J. Phys. Chem. B **118**, 5017 (2014).

[49] A. V. Finkelstein and O. B. Ptitsyn, *Protein Physics* (Academic Press, London, 2002).

[50] T. Peters Jr, *All About Albumin: Biochemistry, Genetics, and Medical Applications* (Academic Press, San Diego, 1995).

[51] C. Tanford, J. Am. Chem. Soc. **86**, 2050 (1964).

[52] B. J. Bennion and V. Daggett, Proc. Natl. Acad. Sci. U.S.A. **100**, 5142 (2003).

[53] S. Deep and J. C. Ahluwalia, Phys. Chem. Chem. Phys. **3**, 4583 (2001).

[54] P. Bharmoria, K. S. Rao, T. J. Trivedi, and A. Kumar, J. Phys. Chem. B **118**, 115 (2014).

[55] G. Panick, R. Malessa, and R. Winter, Biochemistry **38**, 6512 (1999).

[56] D. Paschek and A. E. García, Phys. Rev. Lett. **93**, 238105 (2004).

[57] U. Anand and S. Mukherjee, Phys. Chem. Chem. Phys. **15**, 9375 (2013).

[58] T. Serno, R. Geidobler, and G. Winter, Adv. Drug Deliv. Rev. **63**, 1086 (2011).

[59] A. Rogozea, I. Matei, I. M. Turcu, G. Ionita, V. E. Sahini, and A. Salifoglou, J. Phys. Chem. B **116**, 14245 (2012).

[60] C. M. Dobson, Nature **426**, 884 (2003).

[61] S. W. Englander and L. Mayne, Proc. Natl. Acad. Sci. U.S.A. **111**, 15873 (2014).

[62] V. K. Aswal, S. Chodankar, J. Kohlbrecher, R. Vavrin, and A. G. Wagh, Phys. Rev. E **80**, 011924 (2009).

[63] A. J. R. Law and J. Leaver, J. Agric. Food Chem. **48**, 672 (2000).

[64] A. Wallqvist, D. G. Covell, and D. Thirumalai, J. Am. Chem. Soc. **120**, 427 (1998).

[65] K. K. Andersen and D. E. Otzen, J. Phys. Chem. B **113**, 13942 (2009).

[66] S. Chodankar, V. K. Aswal, P. A. Hassan, and A. G. Wagh, Physica B **398**, 112 (2007).

[67] D. F. Evans and H. Wennerström, *The Colloidal Domain: where Physics, Chemistry, Biology, and Technology Meet, 2nd Edition* (Wiley-VCH, New York, 1999).

[68] P. S. Goyal and V. K. Aswal, Curr. Sci. **80**, 972 (2001).

[69] Y. Chevalier and T. Zemb, Rep. Prog. Phys. **53**, 279 (1990).

[70] J. Haldar, V. K. Aswal, P. S. Goyal, and S. Bhattacharya, Angew. Chem. Int. Ed. **40**, 1228 (2001).

[71] V. K. Aswal and P. S. Goyal, Phys. Rev. E **67**, 051401 (2003).

[72] V. K. Aswal, P. S. Goyal, and P. Thiyagarajan, J. Phys. Chem. B **102**, 2469 (1998).

[73] V. K. Aswal and P. S. Goyal, Phys. Rev. E **61**, 2947 (2000).

[74] D. Varade, T. Joshi, V. K. Aswal, P. S. Goyal, P. A. Hassan, and P. Bahadur, Colloids and Surfaces A: Physicochemical and Engineering Aspects **259**, 95 (2005).

[75] A. J. Chinchalikar, V. K. Aswal, J. Kohlbrecher, and A. G. Wagh, Eur. Phys. J. E **35**, 1 (2012).

[76] L. Jiang, M. Deng, Y. Wang, D. Liang, Y. Yan, and J. Huang, J. Phys. Chem. B **113**, 7498 (2009).

[77] J. V. Joshi, V. K. Aswal, and P. S. Goyal, Pramana **71**, 1039 (2009).

[78] V. K. Aswal and P. S. Goyal, Physica B **245**, 73 (1998).

[79] T. Patel, G. Ghosh, V. K. Aswal, and P. Bahadur, Colloids and Surfaces A: Physicochemical and Engineering Aspects **333**, 145 (2009).

[80] N. J. Turro, X.-G. Lei, K. P. Ananthapadmanabhan, and M. Aronson, Langmuir **11**, 2525 (1995).

[81] D. Lugo, J. Oberdisse, M. Karg, R. Schweins, and G. H. Findenegg, Soft Matter **5**, 2928 (2009).

[82] R. Zhang and P. Somasundaran, Adv. Colloid Interface Sci. **123–126**, 213 (2006).

[83] H. J. Lee, A. McAuley, K. F. Schilke, and J. McGuire, Adv. Drug Deliv. Rev. **63**, 1160 (2011).

[84] R. Piazza, M. Pierno, E. Vignati, G. Venturoli, F. Francia, A. Mallardi, and G. Palazzo, Phys. Rev. Lett **90**, 208101 (2003).

[85] M. N. Jones, Biochem. J. **151**, 109 (1975).

[86] A. D. Nielsen, K. Borch, and P. Westh, Biochim. Biophys. Acta **1479**, 321 (2000).

[87] L. R. S. Barbosa, M. G. Ortore, F. Spinozzi, P. Mariani, S. Bernstorff, and R. Itri, Biophys. J. **98**, 147 (2010).

[88] C. Cao, J. Lei, T. Huang, and F.-P. Du, Soft Matter **10**, 8896 (2014).

[89] E. L. Gelamo, C. H. T. P. Silva, H. Imasato, and M. Tabak, Biochim. Biophys. Acta **1594**, 84 (2002).

[90] M. Vasilescu, D. Angelescu, M. Almgren, and A. Valstar, Langmuir **15**, 2635 (1999).

[91] S. F. Santos, D. Zanette, H. Fischer, and R. Itri, J. Colloid Interface Sci. **262**, 400 (2003).

[92] J. A. Reynolds and C. Tanford, Proc. Natl. Acad. Sci. U.S.A. **66**, 1002 (1970).

[93] M. N. Jones, Chem. Soc. Rev. **21**, 127 (1992).

[94] A. Lee, S. K. Y. Tang, C. R. Mace, and G. M. Whitesides, Langmuir **27**, 11560 (2011).

[95] X.-H. Guo and S.-H. Chen, Chem. Phys. **149**, 129 (1990).

[96] K. Shirahama, K. Tsujii, and T. Takagi, J. Biochem. **75**, 309 (1974).

[97] S.-H. Chen and J. Teixeira, Phys. Rev. Lett. **57**, 2583 (1986).

[98] S. Chodankar, V. K. Aswal, J. Kohlbrecher, R. Vavrin, and A. G. Wagh, J. Phys.: Condens. Matt. **19**, 326102 (2007).

[99] F. J. Lech, M. B. J. Meinders, P. A. Wierenga, and H. Gruppen, Colloids and Surfaces A: Physicochemical and Engineering Aspects **473**, 18 (2015).

[100] B. Nieto-Ortega, J. M. Hierrezuelo, C. C. Ruiz, J. T. L. Navarrete, J. Casado, and F. J. Ramírez, J. Phys. Chem. Lett. **5**, 8 (2014).

[101] X.-H. Guo and S.-H. Chen, Phys. Rev. Lett. **64**, 2579 (1990).

[102] A. Fiechter, Trends Biotechnol. **10**, 208 (1992).

[103] R. Petkova, S. Tcholakova, and N. D. Denkov, Langmuir **28**, 4996 (2012).

[104] M. A. Biasutti, E. B. Abuin, J. J. Silber, N. M. Correa, and E. A. Lissi, Adv. Colloid Interface Sci. **136**, 1 (2008).

[105] P. Khullar, V. Singh, A. Mahal, P. N. Dave, S. Thakur, G. Kaur, J. Singh, S. S. Kamboj, and M. S. Bakshi, J. Phys. Chem. C **116**, 8834 (2012).

[106] E. Roduner, Chem. Soc. Rev. **35**, 583 (2006).

[107] P. Moriarty, Rep. Prog. Phys. **64**, 297 (2001).

[108] G. Cao and Y. Wang, *Nanostructures and Nanomaterials: Synthesis, Properties, and Applications (2nd Edition)* (World Scientific, Singapore, 2011).

[109] M.-C. Daniel and D. Astruc, Chem. Rev. **104**, 293 (2004).

[110] R. A. Sperling, P. Rivera Gil, F. Zhang, M. Zanella, and W. J. Parak, Chem. Soc. Rev. **37**, 1896 (2008).

[111] S. Chakraverty, M. Bandyopadhyay, S. Chatterjee, S. Dattagupta, A. Frydman, S. Sengupta, and P. A. Sreeram, Phys. Rev. B **71**, 054401 (2005).

[112] T. Hanemann and D. V. Szabó, Materials **3** (2010).

[113] R. W. Kelsall, I. W. Hamley, and M. Geoghegan, *Nanoscale science and technology* (John Wiley & Sons, England, 2005).

[114] L. Wang, W. Zhao, and W. Tan, Nano Res. **1**, 99 (2008).

[115] N. J. Halas, ACS Nano **2**, 179 (2008).

[116] I. A. Rahman and V. Padavettan, J. Nanomater. **2012**, 15, 132424 (2012).

[117] A. P. Alivisatos, Science **271**, 933 (1996).

[118] V. H. Grassian, J. Phys. Chem. C **112**, 18303 (2008).

[119] Y. S. Lee, *Self-assembly and nanotechnology: a force balance approach* (John Wiley & Sons, New Jersey, 2008).

[120] A.-H. Lu, E. L. Salabas, and F. Schüth, Angew. Chem. Int. Ed. **46**, 1222 (2007).

[121] J. N. Coleman, U. Khan, W. J. Blau, and Y. K. Gun'ko, Carbon **44**, 1624 (2006).

[122] T. L. Hill, Nano Lett. **1**, 111 (2001).

[123] W. L. Barnes, A. Dereux, and T. W. Ebbesen, Nature **424**, 824 (2003).

[124] M. R. Connolly *et al.*, Nature Nanotechnol. **8**, 417 (2013).

[125] B. Bharti, A.-L. Fameau, M. Rubinstein, and O. D. Velev, Nature Mater. **14**, 1104 (2015).

[126] J. Tang, J. Liu, N. L. Torad, T. Kimura, and Y. Yamauchi, Nano Today **9**, 305 (2014).

[127] Y. Wang *et al.*, J. Am. Chem. Soc. **138**, 3278 (2016).

[128] H. Zhang, M. Jin, Y. Xiong, B. Lim, and Y. Xia, Acc. Chem. Res. **46**, 1783 (2013).

[129] A. P. Kumar, D. Depan, N. S. Tomer, and R. P. Singh, Prog. Polym. Sci. **34**, 479 (2009).

[130] I. Willner and B. Willner, Nano Lett. **10**, 3805 (2010).

[131] C.-C. You, O. R. Miranda, B. Gider, P. S. Ghosh, I.-B. Kim, B. Erdogan, S. A. Krovi, U. H. F. Bunz, and V. M. Rotello, Nature Nanotechnol. **2**, 318 (2007).

[132] B. P. Binks and J. A. Rodrigues, Langmuir **23**, 7436 (2007).

[133] S. Santra, R. Tapec, N. Theodoropoulou, J. Dobson, A. Hebard, and W. Tan, Langmuir **17**, 2900 (2001).

[134] B. P. Binks, J. A. Rodrigues, and W. J. Frith, Langmuir **23**, 3626 (2007).

[135] A. Tulpar, R. D. Tilton, and J. Y. Walz, Langmuir **23**, 4351 (2007).

[136] I. Grillo, in *Soft Matter Characterization*, edited by R. Borsali, and R. Pecora (Springer, Netherlands, 2008), pp. 723.

[137] W. S. Gosal and S. B. Ross-Murphy, Curr. Opin. Colloid Interface Sci. **5**, 188 (2000).

[138] C. Sun, J. Yang, X. Wu, X. Huang, F. Wang, and S. Liu, Biophys. J. **88**, 3518 (2005).

[139] X. Zhang, A. Poniewierski, S. Hou, K. Sozanski, A. Wisniewska, S. A. Wieczorek, T. Kalwarczyk, L. Sun, and R. Holyst, Soft Matter **11**, 2512 (2015).

[140] Y. Li, M. S. Budamagunta, J. Luo, W. Xiao, J. C. Voss, and K. S. Lam, ACS Nano **6**, 9485 (2012).

[141] H. Cui, T. K. Hodgdon, E. W. Kaler, L. Abezgauz, D. Danino, M. Lubovsky, Y. Talmon, and D. J. Pochan, Soft Matter **3**, 945 (2007).

[142] Z. Varga, A. Wacha, and A. Bota, J. Appl. Cryst. **47**, 35 (2014).

[143] D. I. Svergun and M. H. J. Koch, Rep. Prog. Phys. **66**, 1735 (2003).

[144] P. A. Hassan, S. Rana, and G. Verma, Langmuir **31**, 3 (2015).

[145] R. Pecora, *Dynamic light scattering: applications of photon correlation spectroscopy* (Plenum Press, New York, 1985).

[146] V. K. Aswal and P. Goyal, Curr. Sci. **79**, 947 (2000).

[147] S.-H. Chen and T.-L. Lin, in *Methods in Experimental Physics*, edited by D. L. Price, and K. Sköld (Academic Press, New York, 1987), pp. 489.

[148] A. Guinier and G. Fournet, *Small angle scattering of X-rays* (Wiley, New York, 1955).

[149] J. S. Higgins and H. C. Benoit, *Polymers and Neutron Scattering* (Clarendon Press, Oxford, 1994).

[150] O. Glatter, J. Appl. Cryst. **10**, 415 (1977).

[151] J. S. Pedersen, Adv. Colloid Interface Sci. **70**, 171 (1997).

[152] J. K. Percus and G. J. Yevick, Phys. Rev. **110**, 1 (1958).

[153] R. V. Sharma and K. C. Sharma, Physica A **89**, 213 (1977).

[154] L. Reatto and M. Tau, Chem. Phys. Lett. **108**, 292 (1984).

[155] P. A. Egelstaff, *An introduction to the liquid state* (Academic Press, London, 1967).

[156] J. B. Hayter and J. Penfold, Mol. Phys. **42**, 109 (1981).

[157] R. J. Hunter, *Foundations of colloid science* (Oxford University Press, Oxford, 2001).

[158] J.-P. Hansen and J. B. Hayter, Mol. Phys. **46**, 651 (1982).

[159] A. Perera, P. G. Kusalik, and G. N. Patey, J. Chem. Phys. **87**, 1295 (1987).

[160] N. W. Ashcroft and J. Lekner, Phys. Rev. **145**, 83 (1966).

[161] R. J. Baxter, J. Chem. Phys. **49**, 2770 (1968).

[162] P. Schmidt, J. Appl. Cryst. **24**, 414 (1991).

[163] J. Teixeira, J. Appl. Cryst. **21**, 781 (1988).

[164] T. Freltoft, J. K. Kjems, and S. K. Sinha, Phys. Rev. B **33**, 269 (1986).

[165] D. F. R. Mildner and P. L. Hall, J. Phys. D **19**, 1535 (1986).

[166] A. P. Radliński, E. Z. Radlińska, M. Agamalian, G. D. Wignall, P. Lindner, and O. G. Randl, Phys. Rev. Lett. **82**, 3078 (1999).

[167] J. Kohlbrecher and W. Wagner, J. Appl. Cryst. **33**, 804 (2000).

[168] P. Lindner and R. Schweins, Neutron News **21**, 15 (2010).

[169] B. J. Frisken, Appl. Opt. **40**, 4087 (2001).

[170] D. E. Koppel, J. Chem. Phys. **57**, 4814 (1972).

[171] E. D. Goddard and K. P. Ananthapadmanabhan, *Interactions of Surfactants with Polymers and Proteins.* (CRC Press, Boca Raton, 1993).

[172] S. Chodankar, V. K. Aswal, J. Kohlbrecher, R. Vavrin, and A. G. Wagh, Phys. Rev. E **77**, 031901 (2008).

[173] C. A. Nelson, J. Biol. Chem. **246**, 3895 (1971).

[174] A. Valstar, M. Almgren, W. Brown, and M. Vasilescu, Langmuir **16**, 922 (2000).

[175] N. Deo, S. Jockusch, N. J. Turro, and P. Somasundaran, Langmuir **19**, 5083 (2003).

[176] X. L. Zhang, J. Penfold, R. K. Thomas, I. M. Tucker, J. T. Petkov, J. Bent, A. Cox, and I. Grillo, Langmuir **27**, 10514 (2011).

[177] T. Chakraborty, I. Chakraborty, S. P. Moulik, and S. Ghosh, Langmuir **25**, 3062 (2009).

[178] D. Kelley and D. J. McClements, Food Hydrocolloids **17**, 73 (2003).

[179] E. L. Gelamo, R. Itri, A. Alonso, J. V. da Silva, and M. Tabak, J. Colloid Interface Sci. **277**, 471 (2004).

[180] M. A. Mir, N. Gull, J. M. Khan, R. H. Khan, A. A. Dar, and G. M. Rather, J. Phys. Chem. B **114**, 3197 (2010).

[181] U. Keiderling, Appl. Phys. A **74**, s1455 (2002).

[182] J. B. Hayter and J. Penfold, Colloid Polym. Sci. **261**, 1022 (1983).

[183] F. Zhang *et al.*, Phys. Chem. Chem. Phys. **14**, 2483 (2012).

[184] J. Pedersen, J. Appl. Cryst. **33**, 637 (2000).

[185] S. Kumar, V. K. Aswal, and J. Kohlbrecher, Langmuir **28**, 9288 (2012).

[186] W. Warisnoicharoen, A. B. Lansley, and M. J. Lawrence, AAPS PharmSci. **2**, E12 (2000).

[187] E. A. Mun, C. Hannell, S. E. Rogers, P. Hole, A. C. Williams, and V. V. Khutoryanskiy, Langmuir **30**, 308 (2014).

[188] M. Ospinal-Jiménez and D. C. Pozzo, Langmuir **27**, 928 (2011).

[189] J. M. Franklin, L. N. Surampudi, H. S. Ashbaugh, and D. C. Pozzo, Langmuir **28**, 12593 (2012).

[190] E. Dickinson, Food Hydrocolloids **52**, 497 (2016).

[191] S. Tcholakova, N. D. Denkov, and A. Lips, Phys. Chem. Chem. Phys. **10**, 1608 (2008).

[192] M. Tebbe, C. Kuttner, M. Männel, A. Fery, and M. Chanana, ACS Appl. Mater. Interfaces **7**, 5984 (2015).

[193] S. Mehan, V. K. Aswal, and J. Kohlbrecher, Phys. Rev. E **92**, 032713 (2015).

[194] K. Rezwan, L. P. Meier, and L. J. Gauckler, Biomaterials **26**, 4351 (2005).

[195] S. Kumar, V. K. Aswal, and J. Kohlbrecher, Langmuir **27**, 10167 (2011).

[196] B. Bharti, J. Meissner, and G. H. Findenegg, Langmuir **27**, 9823 (2011).

[197] F. Turci, E. Ghibaudi, M. Colonna, B. Boscolo, I. Fenoglio, and B. Fubini, Langmuir **26**, 8336 (2010).

[198] K. Rezwan, A. R. Studart, J. Vörös, and L. J. Gauckler, J. Phys. Chem. B **109**, 14469 (2005).

[199] S. Kumar and V. K. Aswal, J. Phys.: Condens. Matt. **23**, 035101 (2011).

[200] B. Bharti, J. Meissner, S. H. L. Klapp, and G. H. Findenegg, Soft Matter **10**, 718 (2014).

[201] G. Klein, S. Devineau, J. C. Aude, Y. Boulard, H. Pasquier, J. Labarre, S. Pin, and J. P. Renault, Langmuir **32**, 195 (2016).

[202] M. Lundqvist, I. Sethson, and B.-H. Jonsson, Langmuir **20**, 10639 (2004).

[203] S. Kumar, M. J. Lee, V. K. Aswal, and S. M. Choi, Phys. Rev. E **87**, 042315 (2013).

[204] W. Norde and J. P. Favier, Colloids Surf. **64**, 87 (1992).

[205] G. Orts-Gil, K. Natte, D. Drescher, H. Bresch, A. Mantion, J. Kneipp, and W. Österle, J. Nanopart. Res. **13**, 1593 (2010).

[206] A. Kondo, S. Oku, and K. Higashitani, J. Colloid Interface Sci. **143**, 214 (1991).

[207] C. T. McKee and J. Y. Walz, J. Colloid Interface Sci. **365**, 72 (2012).

[208] X. Ye, T. Narayanan, P. Tong, and J. S. Huang, Phys. Rev. Lett. **76**, 4640 (1996).

[209] S. Kumar, V. K. Aswal, and P. Callow, Langmuir **30**, 1588 (2014).

[210] T. A. Witten and L. M. Sander, Phys. Rev. B **27**, 5686 (1983).

[211] R. Tuinier, J. Rieger, and C. G. de Kruif, Adv. Colloid Interface Sci. **103**, 1 (2003).

[212] M. Bergstrom and J. Skov Pedersen, Phys. Chem. Chem. Phys. **1**, 4437 (1999).

[213] L. Shang, Y. Wang, J. Jiang, and S. Dong, Langmuir **23**, 2714 (2007).

[214] P. Roach, D. Farrar, and C. C. Perry, J. Am. Chem. Soc. **128**, 3939 (2006).

[215] K. Das, S. Kundu, S. Mehan, and V. K. Aswal, Chem. Phys. Lett. **610–611**, 405 (2014).

[216] I. Yadav, S. Kumar, V. K. Aswal, and J. Kohlbrecher, Phys. Rev. E **89**, 032304 (2014).

[217] S. Mehan, V. K. Aswal, and J. Kohlbrecher, AIP Conf. Proc. **1665**, 040009 (2015).

[218] S. Mehan, S. Kumar, and V. K. Aswal, AIP Conf. Proc. **1512**, 160 (2013).

[219] S. Mehan, A. J. Chinchalikar, S. Kumar, V. K. Aswal, and R. Schweins, Langmuir **29**, 11290 (2013).

[220] S. Mehan, S. Kumar, and V. K. Aswal, AIP Conf. Proc. **1591**, 167 (2014).

[221] S. Kumar and V. K. Aswal, J. Phys.: Condensed Matt. **23**, 035101 (2011).

[222] J. S. Pedersen, D. Posselt, and K. Mortensen, J. Appl. Cryst. **23**, 321 (1990).

[223] P. Meakin, Phys. Rev. A **27**, 1495 (1983).

[224] P. G. Cummins, E. Staples, and J. Penfold, J. Phys. Chem. **94**, 3740 (1990).

[225] S. Mehan, V. K. Aswal, and J. Kohlbrecher, Langmuir **30**, 9941 (2014).

[226] G. Despert and J. Oberdisse, Langmuir **19**, 7604 (2003).

[227] D. Ray and V. K. Aswal, J. Phys.: Condens. Matt. **26**, 035102 (2014).

[228] D. Ray, V. K. Aswal, and J. Kohlbrecher, J. App. Phys. **117**, 164310 (2015).

[229] F. A. Heberle, D. A. A. Myles, and J. Katsaras, Chem. Phys. Lipids **192**, 41 (2015).

[230] S. Nayak and L. A. Lyon, Angew. Chem. Int. Ed. **44**, 7686 (2005).

[231] G. Konstantatos and E. H. Sargent, Nature Nanotechnol. **5**, 391 (2010).

[232] K. Marshall, Altern. Med. Rev. **9**, 136 (2004).

[233] E. Dickinson, Curr. Opin. Colloid Interface Sci. **15**, 40 (2010).

[234] X. Ding, J. Cai, and X. Guo, Process Biochemistry **50**, 272 (2015).

[235] D. Maiolo, P. Bergese, E. Mahon, K. A. Dawson, and M. P. Monopoli, Anal. Chem. **86**, 12055 (2014).

[236] K. Das, S. Kundu, S. Mehan, and V. K. Aswal, Chem. Phys. Lett. **645**, 127 (2016).

[237] S. Mehan, V. K. Aswal, and J. Kohlbrecher, AIP Conf. Proc. **1665**, 050026 (2015).

[238] S. Mehan, V. K. Aswal, and J. Kohlbrecher, Structure and Interaction of Silica Nanoparticle, BSA Protein and Mixed Nonionic-Ionic Surfactant Complexes (Submitted).